



Josef König, BSc

# **Experimental Study of Separation of Fines from Fiber Suspensions with Hydrodynamic Filtration**

## **MASTER'S THESIS**

To achieve the university degree of

Diplom-Ingenieur

Master's degree program: Chemical and Process Engineering

submitted to

**Graz University of Technology**

Supervisor

Ass.Prof. Dipl.-Ing. Dr.techn. Stefan Radl

Institute of Process and Particle Engineering

Graz, May 2016

## **EIDESSTATTLICHE ERKLÄRUNG**

Ich erkläre an Eides statt, dass ich die vorliegende Arbeit selbstständig verfasst, andere als die angegebenen Quellen/Hilfsmittel nicht benutzt, und die den benutzten Quellen wörtlich und inhaltlich entnommenen Stellen als solche kenntlich gemacht habe. Das in TUGRAZonline hochgeladene Textdokument ist mit der vorliegenden Masterarbeit identisch.

## **AFFIDAVIT**

I declare that I have authored this thesis independently, that I have not used other than the declared sources/resources, and that I have explicitly indicated all material which has been quoted either literally or by content from the sources used. The text document uploaded to TUGRAZonline is identical to the present master's thesis.

---

Date

---

Signature

Copyright © 2016 by Josef König, Graz University of Technology, Institute of Process and Particle Engineering.

OpenFOAM® is the name given to software produced by OpenCFD Ltd. and released free and open source to the general public. See <http://www.openfoam.com/legal/trademark-policy.php>.

All rights reserved. No part of the material protected by this copyright notice may be reproduced or utilized in any form or by any means, electronically or mechanically, including photocopying, recording or by any information storage and retrieval system without written permission from the author.

## **Abstract**

The pulp and paper industry in Austria has recently made a push towards alternative utilization of side products in the paper making process, in order to maintain its competitiveness on the global market. Therefore, the separation of fines, which are small particles and shives within the pulp, became a subject of interest. Established technologies to separate fines from pulp require either large investments, or large operating costs due to high energy consumption.

For this reason, the performance of hydrodynamic filtration (HDF) of fiber suspensions was experimentally assessed. This technology uses no external forces on the suspended particles or fibers, and also no additional chemicals are needed for operation. To allow the manufacturing of complex-shaped side channel geometries, 3D-printing was utilized for the fabrication of decisive parts. The key parameters affecting the separation process were investigated, which are the Reynolds number and the relative flow fraction. Separation efficiencies were determined for different process parameters in order to evaluate the impact of each. By means of high speed imaging, an insight into the flow situation was obtained.

In addition, the flow field of the fluid was predicted by means of Computational Fluid Dynamics simulations, with the goal to guide future improvements of the channel geometry. The pressure drop was measured and compared with the results of the simulations, showing that the energy consumption of the device is small compared to existing technologies. Finally, a pressure drop model was established, which allows the prediction of the required pressure drop, and hence energy demand, for the operation of a larger HDF device.

## **Kurzfassung**

Die Zellstoff- und Papierindustrie in Österreich hat vor kurzem einen Vorstoß in Richtung alternativer Nutzung von Nebenprodukten im Papierherstellungsprozess gemacht, um den wachsenden Herausforderungen auf dem globalen Markt gerecht zu werden. Aus diesem Grund wurde die Abtrennung von Feinstoffen, d.h., kleiner Partikel und Faserbruchstücke in der Zellstoffsuspension, zunehmend interessant. Es gibt zwar etablierte Technologien zur Abtrennung von Feinstoff aus Fasersuspensionen, diese erfordern in der Regel aber entweder hohe Investitionen, oder hohe Betriebskosten aufgrund des hohen Energieverbrauches.

Das Potential der Anwendung von hydrodynamischer Filtration, auch hydrodynamische Fraktionierung genannt, bei der Abtrennung von Feinstoffen wurde experimentell ermittelt. Bei dieser Technik wirken keine externen Kräfte auf die Fasern. Auch werden keine zusätzlichen Chemikalien benötigt, wie beispielsweise bei der Flotation.

Die für das Trennverfahren charakteristischen Parameter wurden isoliert, wobei sich herausstellte, dass die Reynolds Zahl, sowie die relative Abzugsrate entscheidend für eine zufriedenstellende Separierung sind. Der Trenngrad wurde für verschiedene Parametereinstellungen ermittelt, um den Einfluss jedes Parameters zu testen. Zudem wurden mit Hilfe einer Hochgeschwindigkeitskamera Aufnahmen von relevanten Bereichen gemacht, um einen Einblick in die Strömungsvorgänge zu bekommen. Komplizierte Formen wurden mit 3D-Druck gefertigt, um hinsichtlich des Designs der Kanäle nicht limitiert zu sein.

Weiters wurde das Strömungsfeld des Fluids mit Einphasensimulationen berechnet um eine zukünftige Optimierung der Kanalgeometrie vorzubereiten. Der Druckverlust wurde gemessen und mit den Ergebnissen der Simulation verglichen, was den niedrigen Energieverbrauch der Technologie im Vergleich zu etablierten Technologien unterstreicht. Weiters wurde ein Modell für den Zusammenhang zwischen Druckverlust und Durchfluss aufgestellt, um Vorhersagen über den notwendigen Druckverlust, und damit den Energiebedarf, treffen zu können.

## **Acknowledgement**

First of all, I want to thank my advisor Ass.Prof. Dipl.-Ing. Dr.techn. Stefan Radl for the continuous support of my master thesis, for his patience and his engagement. His enthusiasm for science and his determination to get the most out of every student made it a pleasure to work with him.

I gratefully acknowledge the financial support given by the *FLIPPR* consortium.

I also want to thank Dipl.-Ing. Jakob Redlinger-Pohn for his well appreciated comments and remarks, and for his help throughout this thesis.

Further, I want to thank my colleagues Lisa König and Thomas Puffitsch for making my time at the institute even more pleasant.

And I have to say thank you to my family, who supported me in so many ways during my education, and especially to my girlfriend Michaela for making me smile, even after days that didn't go according to plan.

## Table of Content

<b>1</b>	<b>Introduction .....</b>	<b>1</b>
1.1	FLIPPR Project .....	1
1.2	Fines in paper industry .....	1
1.3	Hydrodynamic filtration .....	2
1.4	Goals .....	4
<b>2</b>	<b>State of the art .....</b>	<b>5</b>
2.1	Separation of fines in the pulp and paper industry .....	5
2.2	Single phase simulations .....	6
2.3	Additive manufacturing .....	6
<b>3</b>	<b>Experiments .....</b>	<b>8</b>
3.1	Hydrodynamic filtration device (HDF) .....	8
3.2	Process parameters .....	10
3.2.1	Geometrical parameters .....	11
3.2.2	Pulp properties .....	11
3.2.3	Operating parameters .....	12
3.3	Results of preliminary experiments .....	12
3.3.1	Operating mode .....	14
3.3.2	Consistency .....	14
3.3.3	Pulp .....	14
3.3.4	Side channel plugging .....	15
3.3.5	Varying side channel flow rates .....	15
3.3.6	Summary of preliminary experiments .....	16
3.4	Experimental plan .....	16
3.5	Experimental Results .....	18
3.5.1	Definition of the separation efficiency .....	18

---

3.5.2	Effect of Reynolds number .....	19
3.5.3	Effect of consistency .....	22
3.5.4	Effect of side channel geometry .....	23
3.5.5	Effect of the side channel flow rate .....	26
3.5.6	Effect of channel height .....	27
3.5.7	Effect of channel width .....	29
3.6	Model function for the separation efficiency .....	32
3.7	Velocity Profiles recorded via Particle Image Velocimetry .....	35
<b>4</b>	<b>Single phase simulations .....</b>	<b>37</b>
4.1	Simulation strategy .....	37
4.2	Simulation results .....	39
4.2.1	Velocity field .....	39
4.2.2	Pressure field .....	41
<b>5</b>	<b>Modeling of the pressure drop .....</b>	<b>43</b>
5.1	Relationship between flow fraction and pressure drop .....	43
5.2	Results for pressure drop coefficients .....	44
<b>6</b>	<b>Conclusions .....</b>	<b>47</b>
6.1	Separation Efficiency .....	47
6.2	Pressure drop .....	48
6.3	Projections for operating costs .....	48
6.4	Outlook .....	51
<b>7</b>	<b>Experimental .....</b>	<b>53</b>
7.1	Pre-treatment of the pulp .....	53
7.2	Determination of the mass flow rates .....	53
7.3	Sampling .....	53
7.4	Measuring the consistency .....	54

---

7.5	Measuring the fiber distribution .....	54
7.6	Pressure measurement.....	55
<b>8</b>	<b>References .....</b>	<b>57</b>
<b>Appendix A</b>	<b>Preliminary Experiments .....</b>	<b>60</b>
A.1	Experiments with three open side channels .....	60
<b>Appendix B</b>	<b>P&amp;ID's for the Hydrodynamic Filtration Device .....</b>	<b>64</b>
B.1	Equipment list for P&ID's .....	64
B.2	P&ID for preliminary experiments .....	65
B.3	P&ID for HFD .....	66
<b>Appendix C</b>	<b>Experimental data .....</b>	<b>67</b>
<b>Appendix D</b>	<b>CFD Simulations .....</b>	<b>68</b>
D.1	Geometries .....	68
D.2	Meshing .....	69
D.3	Numerical schemes .....	71
D.4	Boundary conditions and initial values.....	71
<b>Appendix E</b>	<b>Calculations.....</b>	<b>74</b>
E.1	Correlation between total flow rates and relative flow fraction .....	74
E.2	Separation efficiency with confidence intervals .....	76
E.3	Dimensionless Navier-Stokes Equation.....	78
E.4	Pressure drop model.....	79
E.5	Pressure drop in the experiments .....	83
E.6	Projection of the operating costs.....	87
E.6.1	Power draw of the main channel pump .....	87
E.6.2	Power draw for the side channel pump .....	88
E.6.3	Power draw of the purge pump .....	88
<b>Appendix F</b>	<b>MATLAB Code .....</b>	<b>89</b>

## List of Figures

- Fig. 1-1: The principle of hydrodynamic filtration. (a) alignment of particles near the channel wall, meaning that only fluid is removed (b) the separation of small particles at a slightly higher flow rate in the side channel (c) removal of all particles at high flow rates in the side channel (d) the overall separation process as a combination of (a) (b) and (c) [9]..... 2
- Fig. 2-1: Pressure screen “RotoWash” and washer “SpeedWasher” from ANDRITZ AG [21][22]..... 5
- Fig. 3-1: Hydrodynamic Filtration Device with its surroundings. The fiber suspension flows from the stirred storage tank (1) through the HDF (2), where at the side channels liquid is removed through a peristaltic pump (6). The remainder of the suspension flows through the hose exit (3) in the bucket (4), from where it is pumped into the storage tank again with the pump (5). The pressure gauge (7) and the camera support (8) are also part of the device. .... 8
- Fig. 3-2: Top view of the HDF, with the main channel inlet (1), supply for additional water (2) (not used), 2 tightened side channels (3), side channel pump (4), pressure measurement nozzle for measuring the side channel pressure (5), the used side channel (6) and the main channel exit (7)..... 9
- Fig. 3-3: Cross-sectional view of the HDF with the water distribution channel (blue), the main channel (green) and the collector-channel (red). The side channel is integrated in the 3D-printed part (3), the top-wall (4) and bottom-wall (2) of the main channel are made of acrylic glass to allow imaging. The channel height  $L$  can be adjusted by moving the position of the back wall (1) as marked with black arrows..... 10
- Fig. 3-4: Setup of the HDF for preliminary experiments. The suspension is pumped from the storage tank (1) via the pump (2) through the HDF (3), the suspension from all side channels is collected at the side channel exit (4). .... 13
- Fig. 3-5: Top View of the HDF. In the preliminary experiments, all three side channels (2) were used for separation. The water supply (3) was only tested. The main channel inlet (1) and outlet (4) have not changed in the final design..... 13
- Fig. 3-6: Pressure drop in the HDF with three operational side channels. The flow rates at the three side channels  $\dot{V}_{outJ,1}$ ,  $\dot{V}_{outJ,2}$  and  $\dot{V}_{outJ,3}$  depend on the respective pressure differences  $\Delta p_1$ ,  $\Delta p_2$  and  $\Delta p_3$ . The slope of the pressure profile along the main channel is decreasing due to the lower flow rates after every side channel. .... 15

- Fig. 3-7: Variation star with base case in the center and all 6 varied process parameters with their range arranged all around..... 17
- Fig. 3-8: Exemplary separation efficiency curve for a single side channel (red) and 15 side channels (blue), compared to an ideal separation with cut size  $l_{cut} = 0.2$  mm (dashed)..... 19
- Fig. 3-9: Separation efficiency for two different Reynolds numbers at two different flow fractions, at channel dimensions of 3 x 15 mm. As expected, more longer fibers are separated at the higher flow fraction of  $\Phi^+ \approx 0.05$ , compared to the standard flow fraction of 0.015. The big impact of the Reynolds number is given at both flow fractions, suggesting that the regime of flow in the main channel plays a major role. .... 20
- Fig. 3-10: Distribution of the fibers, based on the results of the *L&W fiber tester*, at the inlet *inC* and side channel *outJ*. The class widths are not equal, since fiber lengths below 1 mm are of major interest. At low Reynolds number and flow fraction, side channel fraction consists of over 85% of fines, which shows the potential of the separation technique. .... 21
- Fig. 3-11: Image of the main channel at the side channel entry at two different Reynolds numbers at a consistency of 0.1%. At  $Re = 4,000$ , the fibers are distributed over the channel, while at  $Re = 1,300$  the fibers are moving bound in a network through the channel. Thus, fibers reside mostly in the region from the channel center to the red-dashed lines. .... 21
- Fig. 3-12: Separation efficiency for inlet consistencies of  $C_{inC} \approx 0.5\%$  (white markers) and  $C_{inC} \approx 0.1\%$  (filled markers). At low flow fractions, no significant difference could be observed. However, at a flow fraction of  $\Phi^+ > 0.33$ , the amount of fibers removed is roughly increased by a factor 2 at higher consistency..... 23
- Fig. 3-13: Drawings of the used geometries (top) and images of the printed parts. Clearly, the side channel width in the  $20^\circ$  standard-geometry (left) is roughly the same as at the  $90^\circ$  geometry (right), but should only be 0.75 mm, while the side channel width of the  $90^\circ$  geometry was designed with 1 mm..... 24
- Fig. 3-14: Separation efficiency curves for two different geometries, showing only a small impact of the geometry on the separation characteristics of the device. At higher Reynolds number, the  $90^\circ$  geometry performs slightly better, because the fraction of fines separated is nearly equal to the  $20^\circ$  geometry, while only half of the fibers longer than 2 mm are separated..... 25
- Fig. 3-15: Situation at the side channel entry at  $Re = 4,000$ , and 3 x 15 mm channel dimensions. Despite the low flow fraction  $\Phi^+$  of 0.016, the side channel is nearly fully blocked after 1.6 seconds. To free the side channel again, the side channel was purged with

water, which forces the deposited fibers back into the main channel. This is shown in the right image, at time $t = 2$ s. ....	25
Fig. 3-16: Effect of the flow fraction $\Phi^+$ on the separation, showing that an increase of the side channel flow rate results into lower separation efficiencies for the 3 x 15 mm standard geometry.....	27
Fig. 3-17: Separation efficiency for the standard channel height of 15 and 9 mm, and the standard channel width of 3 mm. For smaller channel heights the effect of the Reynolds number is not visible anymore, and the separation performance is between the ones with 15 mm channel height for a low and high Reynolds number.....	28
Fig. 3-18: Situation in the main channel at 3 different channel heights at $Re = 1,300$ . The fiber network is located in the channel-center, but its size perpendicular to the channel axis seems to be roughly constant. For this reason, the nearly fiber-free area close to the wall gets smaller with decreasing channel height, lowering the impact of the Reynolds number on the separation. ....	29
Fig. 3-19: Separation efficiency for different channel widths at Reynolds numbers of 1,300 and 4,000, as well as low flow fractions. Only for the lower Reynolds number, a difference in the separation efficiency was observed, where more fibers are separated in the wider channel. This was also due to the higher flow fraction, caused by limitations associated with the operation of the side channel pump.....	30
Fig. 3-20: Separation efficiency for different channel widths at Reynolds numbers of 1,300 and 4,000, and at high fractions. ....	31
Fig. 3-21: Possible orientations of fibers within the channel. Fibers longer than the channel width are hindered to orient vertically. ....	31
Fig. 3-22: Fiber flow at 9 mm channel width at two different Reynolds numbers and a consistency of 0.12%, at a flow fraction of 0.017 (left) and 0.022 (right). Note, not all fibers are in focus in these images.....	32
Fig. 3-23: Separation efficiency for different Reynolds numbers and flow fractions (symbols) approximated by the model function (lines), showing good agreement between model function and experimental results. The model function, equation (3-8), was fitted using MATLAB. ....	33
Fig. 3-24: Image of the channel flow (left panel) and the resulting velocity field determined with PIV (right panel), at $Re = 1,300$ and $\Phi^+ = 0.045$ in the 3 x 15 mm channel.....	35

Fig. 3-25: Flow field with averaged values over 1,000 images at $Re = 1,300$ and $\Phi^+ = 0.045$ in the 3 x 15 mm channel. The velocity is decreasing at $y$ values lower than 2 mm. ....	36
Fig. 4-1: HDF with the simulation domain (red) for the $90^\circ$ geometry, with the inlet face $in_C$ and the two outlet faces $out_C$ and $out_J$ . ....	38
Fig. 4-2: Simulation results for the velocity field at $Re = 500$ , for the $90^\circ$ side channel geometry (left panel) and the $20^\circ$ geometry (right panel). The pressure at the side channel increases from top to bottom. ....	39
Fig. 4-3: Streamlines for the $20^\circ$ junction, illustrating the complex flow situation at the entry into the collector channel (left panel). Velocity field with vectors colored by the magnitude of the velocity at the center plane of the side channel (right panel). ....	40
Fig. 4-4: Simulation results for the pressure field at $Re = 500$ , for the $90^\circ$ side channel geometry (left side) and the $20^\circ$ geometry (right side). The pressure at the side channel increases from top to bottom. ....	41
Fig. 5-1. Illustration of the $20^\circ$ side channel geometry, including all variables used in the model for the pressure drop. ....	43
Fig. 5-2: Results of the simulations (markers) and the model function for the determined frictional factors. ....	45
Fig. 5-3: Results for the flow fractions as a function of the pressure difference for both geometries at two different Reynolds numbers. ....	46
Fig. 6-1: Separation efficiency at $Re = 4,000$ and $\Phi^+ = 0.015$ after 1, 10, 50 and 100 side channels. ....	51
Fig. 7-1: Suction filter with vacuum pump (left panel) and sheet dryer (right panel) as used for the determination of the consistencies. ....	54
Fig. 7-2: <i>L&amp;W FIBER TESTER PLUS</i> with the PC for the data analysis at the IPZ. ....	55
Fig. 7-3: T-junction for pressure measurement. In case the initial pressure in the measuring line is too low, the interfacial area is shifted upwards as shown by the dashed line, and further the measured pressure is lowered by $\rho_{water} g \Delta h_m$ . Here, the pressure of the hydrostatic height of air is neglected, since the density of air is much lower than the density of water. ....	55
Fig. A-1: First set of experiments, with two different operation modes. The flow rate in the main channel at the first 4 experiments was controlled via a peristaltic pump. The channel dimensions were 3 x 15 mm at the $90^\circ$ side channel geometry. ....	60
Fig. A-2: Results for the preliminary experiments using mechanical pulp from <i>Norske Skog Bruck</i> , at channel dimensions of 3 x 15 mm at the $90^\circ$ geometry. ....	61

Fig. A-3: Separation efficiencies for channel dimensions of 3 x 15 mm at the 20° geometry.	62
Fig. A-4: Solenoid valve <i>Bürkert 134071</i> , as used for controlling the purge flow rate. ....	63
Fig. A-5: Flow rates through the solenoid valve as a function of the pause time and impulse time, which are adjusted with the time relays <i>ABB CT-TGS</i> . ....	63
Fig. B-1: P&ID of the HDF, at preliminary experiments. The main channel flow rate is controlled via a peristaltic pump. ....	65
Fig. B-2: P&ID of the HDF. The main channel flow rate is controlled via the height of the liquid in stirred storage tank <i>B1</i> and the height of the liquid in the bucket <i>B3</i> . ....	66
Fig. D-1: Geometry of the flow situation at a single side channel. Fluid passes the three black colored faces inC, outC and outJ. ....	68
Fig. D-2: Mesh of the 90° standard geometry, built with blockMesh and extrudeMesh. The cells in the side channel region are smaller with increasing x-position, because higher gradients are expected at this side. The total number of cells is approx. 650 000. ....	70
Fig. D-3: Mesh for the 20° geometry, built with blockMesh and extrudeMesh. The mesh is finer at the left wall of the side channel, because the fluid is expected to be located there due to inertia. The total number of cells for this mesh is approx. 650,000. ....	70
Fig. D-4: Velocity profile imposed at the inlet patch inC, created with setInletVelocity with the solution of Tamayol and Bahrami [38]. ....	73
Fig. E-1: Flow rates at the main channel with multiple side channels. ....	74
Fig. E-2: Total fraction of the inlet flow $\Psi_+$ depending on the relative flow fraction $\Phi^+$ for different numbers of side channels. ....	76
Fig. E-3: Exemplary results of the separation efficiency, with error bars based on the standard deviation and confidence intervals. ....	77
Fig. E-4: Geometrical situation of the 90° geometry. All dimensions are normalized with the channel height $L^+$ . The pressure at the plane $A_{SC}$ is determined by averaging the pressure at 9 measurement points in the simulation. ....	80
Fig. E-5: Geometrical situation of the 20° geometry. All dimensions are normalized with the channel height $L^+$ . The pressure at the plane $A_{SC}$ is determined by averaging the pressure at 9 measurement points in the simulation. ....	80
Fig. E-6: Pressure drop in the HDF. The red colored area shows the part for which single-phase simulations are done. ....	84
Fig. E-7: Factor $\varphi_{AR}$ as a function of the aspect ratio $AR$ , as given in [35] ....	85
Fig. E-8: Loss coefficient $\zeta_{wide}$ as a function of the widening angle $\beta$ , as given in VDI [35].	86

---

## List of Tables

Table 3-1: Parameters for the model function describing the separation efficiency.....	34
Table 6-1: Process parameters for the estimate of the power draw of a HDF with a throughput of 100,000 kg/h suspension.....	50
Table 6-2: Results for the power draw of a HDF with a throughput of 100,000 kg/h suspension, with 10 and 100 side channels per main channel. ....	50
Table B-1: List of the equipment as detailed in the P&ID's.....	64
Table C-1: Operating parameters and results of the experiments. ....	67
Table C-2: Description of the geometry ID's used in Table C-1.....	67
Table D-1: Settings for the numerical schemes used in openFOAM.....	71
Table D-2: Initial values and boundary conditions used for the simulations in openFOAM. .	72

---

## Abbreviations

CAD	Computer Aided Design
CFD	Computational Fluid Dynamics
DNS	Direct Numerical Simulation
FDM	Fused Deposition Modeling
FLIPPR	Future Lignin and Pulp Processing Research
HDF	Hydrodynamic Filtration Device
IPPT	Institute of Process and Particle Engineering at TU Graz
LIGGGHTS®	LAMMPS Improved for General Granular and Granular Heat Transfer Simulations
LES	Large Eddy Simulation
OpenFOAM®	Open Source Field Operation and Manipulation
PIV	Particle Image Velocimetry
PTV	Particle Tracking Velocimetry
RANS	Reynolds-Averaged Navier-Stokes equations
SLS	Selective Laser Sintering
STL	Stereo Lithography

## Nomenclature

### Latin Symbols

$A$	cross sectional area	$\text{m}^{-2}$
$C$	consistency	%
$D$	characteristic length for Stokes number	m
$d$	diameter	m
$k$	regime coefficient	-
$K$	costs	€
$L$	channel height / length	m
$L^+$	dimensionless length, norm. by channel height	-
$m$	regime coefficient	-
$\dot{m}$	mass flow rate	$\text{kg s}^{-1}$
$n$	number of side channels / number of samples / regime coefficient	- / - / -
$P$	power	$\text{kg m}^2 \text{s}^{-3}$
$p$	pressure	$\text{kg m}^{-1} \text{s}^{-2}$
$\bar{p}$	spatially averaged pressure	$\text{kg m}^{-1} \text{s}^{-2}$
$\langle \bar{p} \rangle$	time- and spatially averaged pressure	$\text{kg m}^{-1} \text{s}^{-2}$
$r$	regime coefficient	-
$R^2$	coefficient of determination	-
$Re$	Reynolds number	-
$s^2$	sample variance	-
$SCW$	side channel width	m
$SCW^+$	dimensionless side channel width	-
$Stk$	Stokes number	-
$t$	time	s

$T$	separation efficiency	-
$U$	characteristic velocity / cross s. circumference	$\text{m s}^{-1} / \text{m}$
$u$	velocity	$\text{m s}^{-1}$
$\bar{u}$	spatially averaged velocity	$\text{m s}^{-1}$
$\langle \bar{u} \rangle$	time- and spatially averaged velocity	$\text{m s}^{-1}$
$\dot{V}$	volumetric flow rate	$\text{m}^3 \text{s}^{-1}$
$W$	channel width	m
$W^+$	dimensionless width, norm. by channel height	-
$x$	particle size (general)	m

### Greek Symbols

$\alpha$	side channel angle	deg
$\varepsilon$	pump efficiency	-
$\Phi^+$	volumetric flow fraction	-
$\Delta h_{exp}$	height difference in the experiment	m
$\Psi^+$	total volumetric flow fraction	-
$\lambda$	pipe friction factor	-
$\mu$	dynamic viscosity	$\text{kg m}^{-1} \text{s}^{-1}$
$\Delta p^+$	dimensionless pressure difference	-
$\Delta Q$	fraction in a class	-
$\rho$	density	$\text{kg m}^{-3}$
$\nu$	kinematic viscosity	$\text{m}^2 \text{s}^{-1}$
$\zeta$	pressure loss coefficient	-

### Indices

$C$	channel	-
$cont$	contraction	-
$cut$	cut size	-

---

<i>exp</i>	experimental	-
<i>fines</i>	fines fraction	-
<i>fiber</i>	fiber	-
<i>fluid</i>	fluid	-
<i>h</i>	hydraulic	-
<i>i</i>	component <i>i</i>	-
<i>inC</i>	main channel inlet	-
<i>inlet</i>	total at inlet	-
<i>J</i>	junction	-
<i>min</i>	minimum	-
<i>max</i>	maximum	-
<i>oa</i>	overall	-
<i>outC</i>	main channel outlet	-
<i>outJ</i>	side channel outlet (J = junction)	-
<i>outJ,tot</i>	total side channel outlet	-
<i>p</i>	particle	-
<i>Purge</i>	purge channel	-
<i>ref</i>	reference	-
<i>SC</i>	side channel	-
<i>single</i>	with respect to a single side channel	-
<i>wid</i>	widening at inlet and outlet to main channel	-
<i>w</i>	side channel widening	-

# 1 Introduction

## 1.1 *FLIPPR Project*

This work is part of the FLIPPR (Future Lignin and Pulp Processing Research) project. The aim of this project is to find new applications for by-products in the pulp and paper production [1][2].

The FLIPPR consortium consists of the leading Austrian companies in the field of pulp and paper technology, the BOKU Vienna, the University of Graz, and the Graz University of Technology (TU Graz). The project is divided into the main areas (i) lignin research and (ii) pulp and paper research. Within the FLIPPR project, the Institute of Process and Particle Engineering at TU Graz is dealing with the separation of fines from pulp suspensions.

## 1.2 *Fines in paper industry*

Products of the pulp and paper industry are recovered primarily from wood, for which two different process types for the extraction of fibers from the wood matrix are commonly used: (i) chemical pulping, and (ii) mechanical pulping. Both methods can be used to produce pulp, i.e., a mixture of water, fibers and fines. In this work, fines are defined as fibers described by a length below 200 microns. However, fines are often referred to as the fraction which passes a screen of a certain size, i.e., usually a mesh-200 screen with a mesh size of 76 microns [3].

Depending on the position in the process, this fines fraction also contains pigments and fillers, as they also are below this size. In addition, a distinction between primary fines, originally present in the wood, and secondary fines, generated during refining, can be made. Fines produced in later stages of the process are usually termed tertiary fines [3]. In literature, also the term micro fibrillated cellulose is often used instead of fines, since an exact definition of the two terms is not given and varies with the application [4].

The relative amount, as well as the morphology of the fines has a large influence on the properties of the final product, which is paper in most cases. Due to its larger specific surface area, fines behave differently in all surface-controlled processes [5]. For example,

the necessary amount of bleaching chemicals to reach a certain degree of whiteness decreases with lower fines content.

A lower fines content also causes a lower water retention in most cases, which positively affects the energy consumption in the drying section of a paper machine [6], since the amount of water to be removed decreases. Contrary, an increasing fines content has a positive effect in terms of strength characteristics of the paper, because fines act as a natural filler and lead to higher binding forces within the fiber network in the paper [7].

Currently, fines are not deliberately separated in the paper making process, caused by the difficulty to achieve a sharp and economically feasible separation from fiber suspensions. The separation of fines would possibly allow new or optimized products, e.g., paper with high porosity, associated with high absorbency [8].

### 1.3 Hydrodynamic filtration

Hydrodynamic Filtration is a separation technique that uses hydrodynamic forces acting on particles. Since no external forces are applied, it can be grouped into so-called passive separation techniques. It is quite similar to cross flow filtration, however, the key difference is that the side channels can be wider than the particle diameter, meaning that particles are not hindered to enter the side channel only by their size.

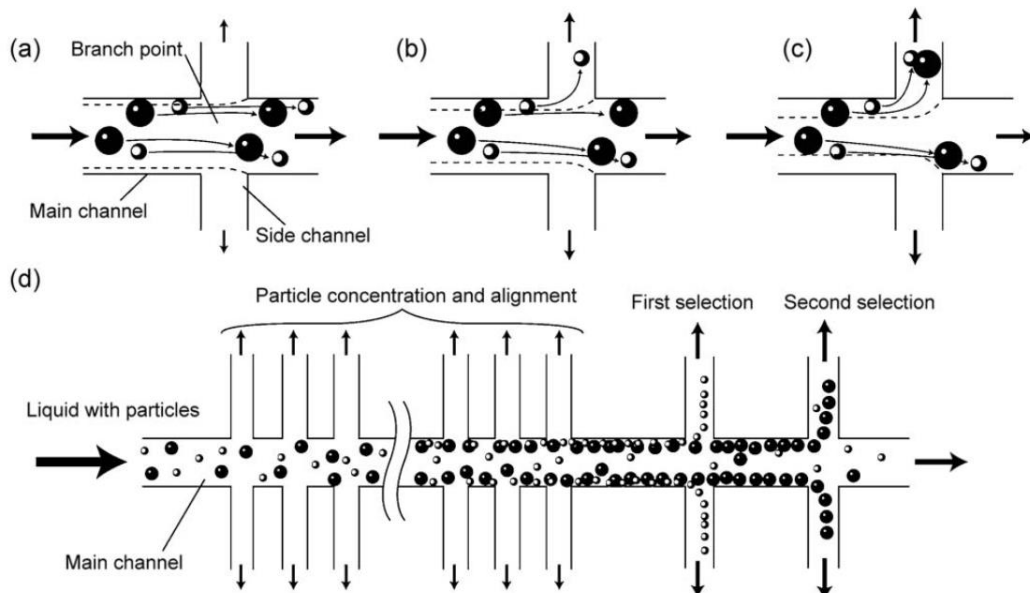


**Fig. 1-1: The principle of hydrodynamic filtration. (a) alignment of particles near the channel wall, meaning that only fluid is removed (b) the separation of small particles at a slightly higher flow rate in the side channel (c) removal of all particles at high flow rates in the side channel (d) the overall separation process as a combination of (a) (b) and (c) [9].**

Due to the precise control of the flow rate in the side channels, small particles can be separated. In case the hydrodynamic center of a particle is outside the region marked by the dashed line in Fig. 1-1 (a) to (c), the particle stays in the main channel. The higher the flow rate in the side channels, the larger gets this region, and thus the larger are the particles to be separated. For instance, the separation of white blood cells from red blood cells, where a gentle treatment of the cells is of utmost importance, has been performed with this method [10].

A small particle is only separated in case it is located inside the small liquid layer that is removed, thus its alignment in the main channel is critical. A so-called wall effect lift forces particles to move away from the channel's wall, and decreases with wall distance. Contrary, a shear gradient lift, directed down the shear gradient and thus from the channel-center to the wall, is acting on the particle as well. In combination, these forces lead to an equilibrium position of a small particle in channel flow [11][12].

Since hydrodynamic filtration can also be applied to non-spherical and rod-like particles [13][14], it is also suitable for separating fibers according to their length. The major difference between the motion of fibers and spherical particles in a channel flow is that the acting hydrodynamic forces depend not only on the particles' position but also on its orientation. Furthermore, the rotation of fibers due to wall contact plays an important role for the fibers' alignment. After a contact with the wall, the fiber rotates and moves inwards, until the distance from the wall reaches half of the fiber's length. This leads to a lower concentration of long fibers in regions close to the wall [15][16]. The separation process at the junction can only take place in a satisfactory manner if the rotation of the fiber has already taken place, so that the center of the fiber is outside of the separation layer. Thus, the distance between side channels has to exceed the length in flow direction a fiber needs to rotate.

The behavior of fibers passing a small slot has been investigated at high Reynolds numbers to mimic the conditions in an industrial pressure screen, both experimentally and by means of simulations [17][18][19][20]. The simplified setup to mimic an industrial pressure screen is quite similar to the setup for hydrodynamic filtration. However, the difference in the main channel Reynolds number, together with the different relative flow rates at the side channel indicates the need to investigate the separation behavior of fibers in hydrodynamic filtration devices at low Reynolds numbers. Furthermore, in most types of

pressure screens the main goal is to achieve a high fiber passage ratio, which means that all fibers should pass the aperture, and larger particles should be retained. In contrast, the goal of hydrodynamic filtration is to let only fines pass the side channel, while fibres should be retained.

## **1.4 Goals**

The separation of fines from fiber suspensions with hydrodynamic filtration will be investigated with experiments performed on a novel lab-scale device, further called Hydrodynamic Filtration (HDF) Device. The experiments will be done at the Institute of Process and Particle Engineering, analytical tasks, e.g. measurement of the fiber length distribution, are performed partly at the Institute for Paper-, Pulp- and Fiber Technology. For simulations, the dcluster at TU Graz can be accessed, which hosts more than 2,400 computing cores.

The main goals of this thesis are to:

- quantify the separation behavior based on experiments (i.e., identify key parameters that affect separation),
- calculate the pressure drop for relevant flow situations with single-phase-simulations to establish mechanistic understanding of fluid flow in the device,
- investigate the applicability of the technique for the separation at high consistencies, e.g., via a comparison of high-speed imaging videos and existing simulations, and to
- give an outlook on the suitability for industrial scale separation of fines (i.e., roughly estimate investment and energy input needed).

## 2 State of the art

### 2.1 Separation of fines in the pulp and paper industry

Since fines can be used as a side product, it is of interest to separate them from fiber suspensions. In that case, primary and secondary fines play a bigger role than tertiary fines, since the inorganic particles in the latter are not wanted for most applications of fines. We can differentiate technologies for the separation of organic fines and inorganic fines, and technologies that focus on the separation of fines from fiber suspensions in general, where hydrodynamic filtration is part of the latter.

Pressure screens are widely used in the paper making process, in most cases to remove undesired material from a fiber suspension. In such applications, fibers pass a screening basket, while impurities stay in the so-called reject stream. Pressure screening can also be used for fractionation of fibers by its length, but typically a huge amount of energy up to 300 kW is needed for a typical aggregate. This energy input is dissipated by the rotor in the center of the device which is pushing the liquid and small fibers through very narrow gaps in the range of 100 to 300  $\mu\text{m}$ .

Another approach is to mimic the processes at the headbox of a paper machine, where the sheet formation takes place. The apparatus is operated as a small closed-circuit device and is used to separate mostly tertiary (i.e., organic and inorganic) fines from pulp. These devices are commonly termed as washers. For both, the pressure screen and washer, examples are shown in Fig. 2-1.

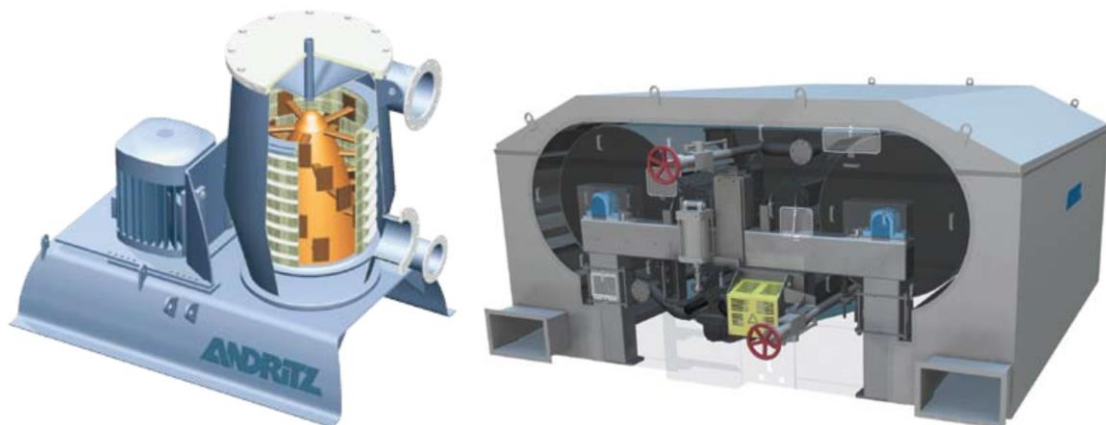


Fig. 2-1: Pressure screen “RotoWash” and washer “SpeedWasher” from ANDRITZ AG [21][22].

Like pressure screens, also small units of hydro cyclones (often termed “cleaners”) are used to recover usable fibers. However, the density of primary and secondary fines is quite similar to the density of longer fibers, which makes separation of organic fines from fibers difficult. Because of its small size and moderate flow rates, cleaners are usually installed in parallel units and stages to allow the required flow rates and separation efficiency [23].

## **2.2 Single phase simulations**

The description fluid dynamics by means of computational methods, also known as computational fluid dynamics (CFD), is found in a variety of fields, like engineering science, medical science as well as meteorology. The term fluid includes both liquid and gaseous media.

Commercial software (e.g. Ansys Fluent, COMSOL) is available on the market, which helps the user at decisions regarding the correct set-up, as well as open-source software such as the software package OpenFOAM®, which is used in this work. As a user of CFD software, the main focus is on the proper selection of discretization schemes and a correct virtualization of the geometric situation, in general called meshing. The discretization scheme describes the method for time and space discretization.

In order to simulate large systems, the calculations are nowadays often performed on computer clusters. These clusters allow large simulation using rigorous models, which in extreme cases can utilize up to several thousand computing cores at a time. With the everlasting progress of computing power, it is now also possible to directly predict small-scale transient phenomena, e.g., turbulence. This type of simulation is called Direct Numerical Simulation (DNS), and is used to describe the flow in the apparatus also in this work.

## **2.3 Additive manufacturing**

With additive manufacturing, manufacturing processes are generally understood in which products are produced by a layer-wise plotting of material. The major advantage of additive manufacturing is the almost limitless freedom in the design-process of a component, since conventional manufacturing steps bring certain limitations with them, such as hollow spaces inside of parts.

It is possible to produce end products with 3D printing, but it can also be combined with conventional manufacturing processes to reduce the manufacturing costs and expand the design capabilities.

Referring to Femmer et al. [24], 3D printing techniques can be categorized with respect to their working principle:

- Liquid-based techniques
- Wire-based techniques
- Powder-based techniques
- Foil-based techniques

Typically, various polymeric materials are used for 3D printing. However, in recent years there has also been a significant progress in printing metallic materials, especially in the field of powder-based techniques, such as selective laser sintering (SLS).

Highest accuracies can be achieved with liquid-based techniques, such as the Polyjet printing process, developed by the American manufacturer Stratasys. The method can be compared with conventional inkjet printing, which is used for printing ink on paper. However, instead of ink, a UV-curable polymer which is cured immediately after it has left the nozzle. The achievable minimum layer thickness is in the size range of 16 microns (in the z direction) at a resolution of 600 dpi in the *x*- and *y*-axis [22]. If necessary, a support structure is printed with water-soluble material and removed after completion of the product with water.

In the lower price range mainly so-called Fused Deposition Modeling (FDM) printers are available, which use fine plastic filaments to build up the print layer by layer. The prices for printer and the print material relying on FDM are rather low compared to other printing processes. Unfortunately, the achievable accuracy and surface quality is typically well below that of other methods.

In the course of this work, the Polyjet print technology was predominantly used, while some individual parts were produced by means of FDM printing.

## 3 Experiments

### 3.1 Hydrodynamic filtration device (HDF)

Prior to this work, a novel lab-scale device was designed and assembled, as shown in the work of König [8]. However, for the experiments in this thesis, modifications had to be done, which are detailed in the sections below and in the appendix.

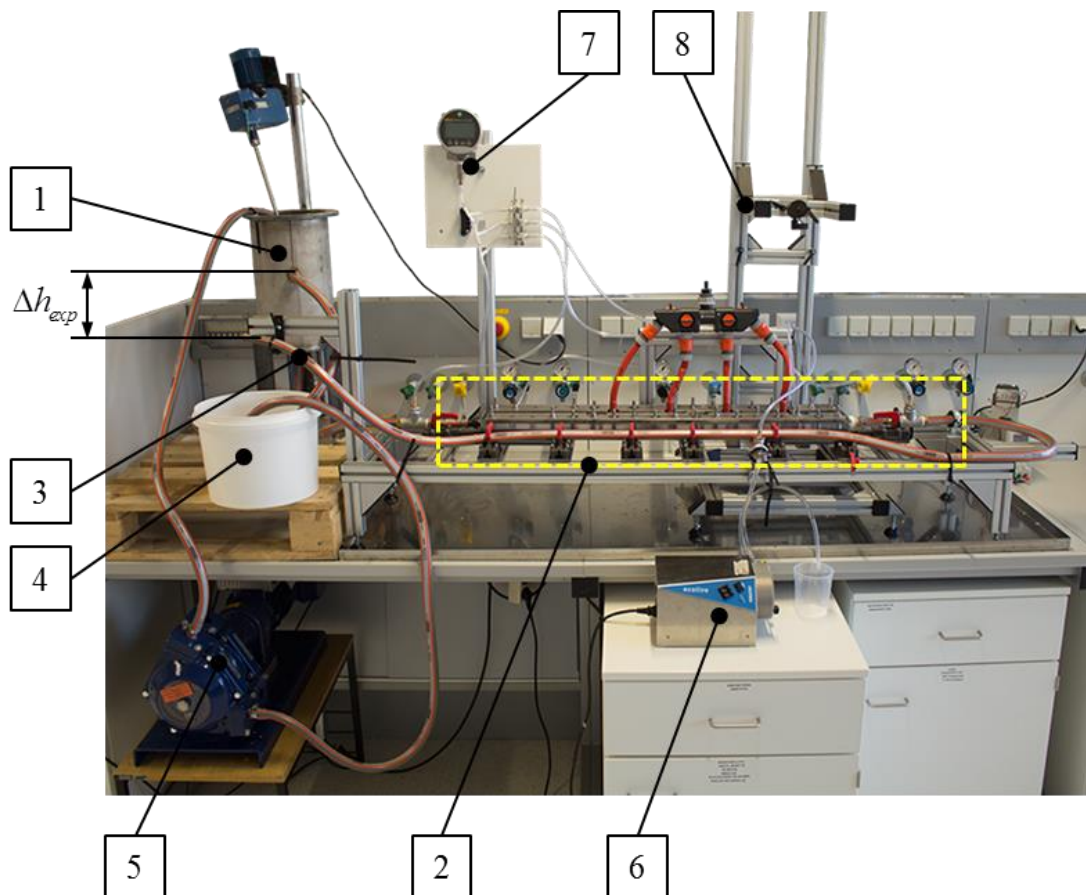


**Fig. 3-1: Hydrodynamic Filtration Device with its surroundings. The fiber suspension flows from the stirred storage tank (1) through the HDF (2), where at the side channels liquid is removed through a peristaltic pump (6). The remainder of the suspension flows through the hose exit (3) in the bucket (4), from where it is pumped into the storage tank again with the pump (5). The pressure gauge (7) and the camera support (8) are also part of the device.**

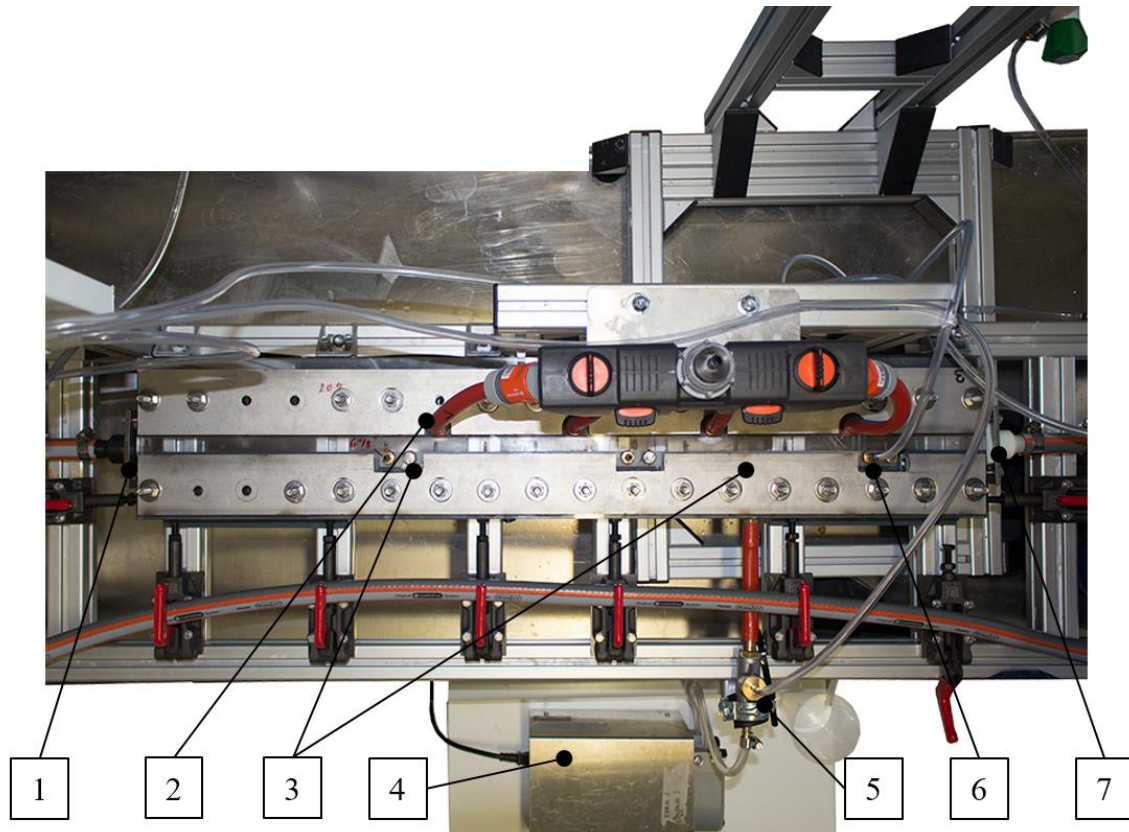


**Fig. 3-2:** Top view of the HDF, with the main channel inlet (1), supply for additional water (2) (not used), 2 tightened side channels (3), side channel pump (4), pressure measurement nozzle for measuring the side channel pressure (5), the used side channel (6) and the main channel exit (7).

The fiber suspension is stirred in the storage tank before flowing into the main channel. At the inlet of the separation unit, the cross-sectional area changes from the circular shape of the connected hose to the rectangular-shaped cross section of the main channel. This transition was realized using a 3D-printed adapter. A small fraction of the incoming suspension is removed via the side channel, where the volume flow rate is controlled via a peristaltic pump. The fiber suspension exits the main channel at the outlet adapter towards a bucket, from which it is again pumped into the storage tank. The level in the storage tank is controlled by a nozzle, from which fiber suspension flows back into the bucket after the desired fill level is reached. The flow rate through the HDF is a function of the total pressure drop over the device, thus the height level of the hose right before the bucket drives the flow rate. This is also visualized in Fig. 3-1 by  $\Delta h_{exp}$ , which is the height difference between the liquid level in the storage tank and the hose exit.

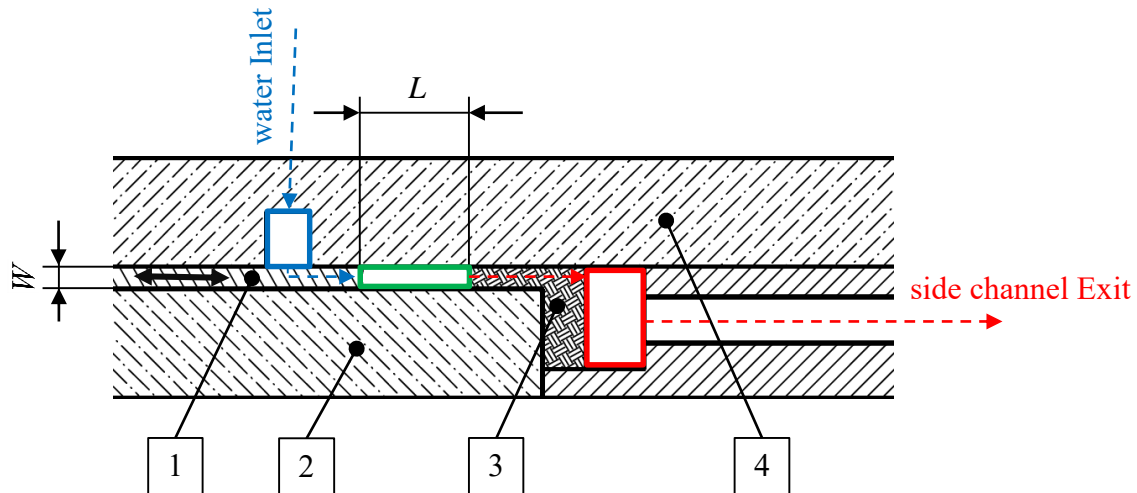


**Fig. 3-3:** Cross-sectional view of the HDF with the water distribution channel (blue), the main channel (green) and the collector-channel (red). The side channel is integrated in the 3D-printed part (3), the top-wall (4) and bottom-wall (2) of the main channel are made of acrylic glass to allow imaging. The channel height  $L$  can be adjusted by moving the position of the back wall (1) as marked with black arrows.

The dimensions of the rectangular main channel can have the values 3, 9 and 15 mm in height and 3 and 9 mm in width, so they are of the same order of magnitude as the length of typical pulp fibers. The side channel geometry is integrated in a 3D-printed part. This fabrication technique has the major advantage that also complicated geometrical shapes can be realized, compared to slot geometries at research on pressure screening [19][25]. The side channel branch is leading to a collector-channel parallel to the main channel, with dimensions in the same order as at the main channel, depending on the main channel width to reduce the pressure drop from the side channel to the peristaltic pump to a minimum.

The water distribution channel (blue colored in Fig. 3-3) allows the addition of water at a number of smaller water-channels along the main channel. This feature has been added for future purposes and was not used for the experiments in this thesis.

### 3.2 Process parameters

A fundamental need in order to obtain satisfactory results is to know all influence variables of the system, and to further isolate the key parameters. In the studied fiber suspension system, the influence variables can be divided into:

1. Geometric parameters (e.g., the channel dimensions, side channel geometry)
2. Pulp properties (e.g., the fiber-length distribution)
3. Operating parameters (e.g., Reynolds number, side channel flow rate, consistency)

### 3.2.1 Geometrical parameters

- Width  $W$  and Height  $L$

In the main channel of the HDF, different channel dimensions can be realized. Since the cross-sectional area is of rectangular shape, both the channel height and width can be varied. The difference between changing the channel height and changing the channel width is that the latter also changes the dimensions of the side channel (see Fig. 3-3).

- Side channel geometry

The side channel geometry, including the width of the side channel and its angle related to the main channel, is essential for the separation behavior. The flow field around the entry of the side channel determines whether a fiber gets separated or not. When choosing the dimensions too small, the pressure drop is expected to increase for the same flow rates, in the opposite case the flow field might cause problems regarding separation behavior.

### 3.2.2 Pulp properties

Due to the variety of application areas an enormous variety of fibrous materials is available on the market. The aim is to cover the properties of a lot of different pulps, which makes choosing a representative pulp a tough decision. However, we used pulp from *SAPPI Gratkorn* and *Norske Skog Bruck*, representing softwood chemical and mechanical pulp, respectively.

- Fiber-length distribution

The HDF is designed to separate fibers by length, meaning that in an ideal system with infinite dilution, the fiber length distribution should not have an impact on the separation. However, fiber-fiber interactions are expected to have an impact on the separation behavior. These interactions can be observed above consistencies of around 0.05%, which means that in technical relevant applications we always have to deal with these phenomena. Due to its contribution to the presence of fiber-fiber interactions, the fiber-length distribution is important for the flow of the suspension in the main channel.

- Consistency

Together with the fiber-length distribution, the consistency determines whether fibers are mobile in the suspension or not. The latter is defined as the mass fraction of fibers, and can be determined by thermogravimetric analysis.

### 3.2.3 Operating parameters

- Flow rate

The flow rate determines the flow regime in the HDF, and it is proportional to the Reynolds number, a dimensionless number to characterize the ratio of inertial forces to viscous forces in a fluid flow. The flow rate through the apparatus depends on the hydrostatic pressures at the inlet and outlet, with the pressure at the inlet given through the liquid height in the storage tank and the pressure at the outlet driven by the height of the hose exit. The height of the storage tank cannot be adjusted, so the flow rate is only controlled by the pressure at the outlet of the HDF. The maximum flow rate through the apparatus is in the range of 2,200 ml/min at channel dimensions of 3 x 15 mm for width and height, respectively.

- Side channel flow rate

The more liquid is removed at the side channel, the bigger gets the liquid layer in the main channel that is entering the side channel. The side channel flow rate is controlled via a peristaltic pump, which has a minimum flow rate of 10.4 ml/min.

Since the ratio between the two flow rates can be used as a description, the flow fraction  $\Phi^+$  is defined as

$$\Phi^+ = \frac{\dot{V}_{outJ}}{\dot{V}_{outC}} \quad (3-1)$$

where  $\dot{V}_{outC}$  is the flow rate at the main channel outlet and  $\dot{V}_{outJ}$  at the side channel.

### 3.3 Results of preliminary experiments

Since the HDF is a novel laboratory device, preliminary experiments were necessary to determine its capabilities. In the experiments, the side channel width was set to 1 mm at an angle 90° relative to the main channel. All 3 side channels were used for separation. A detailed description of these experiments is given in Appendix A, while only its general findings are discussed in this section.

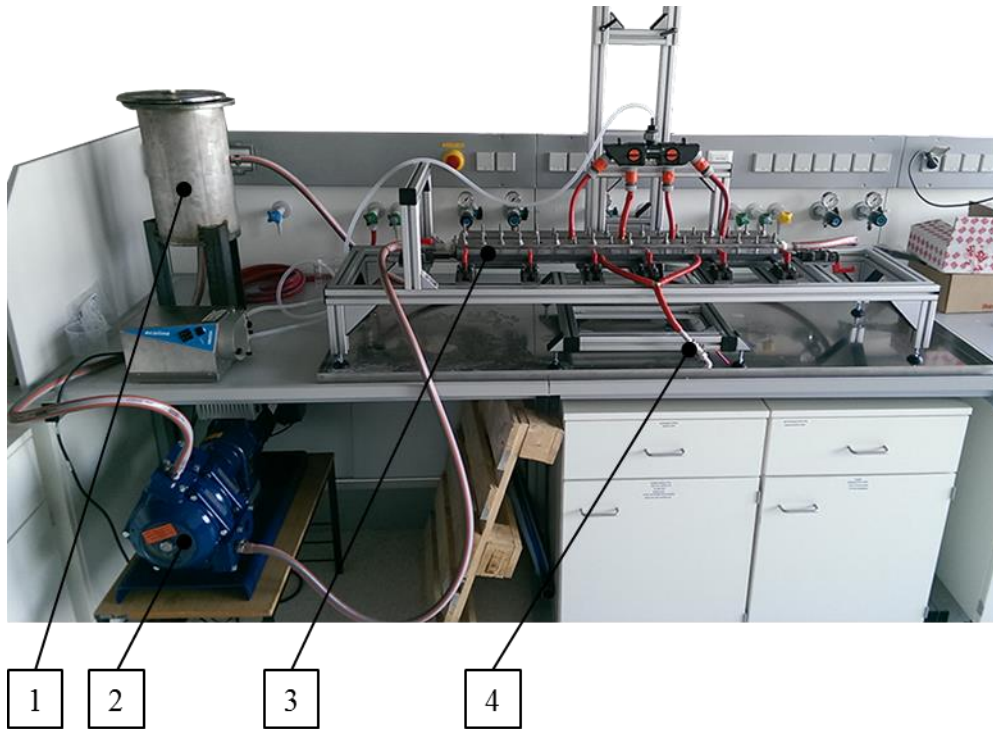


**Fig. 3-4: Setup of the HDF for preliminary experiments. The suspension is pumped from the storage tank (1) via the pump (2) through the HDF (3), the suspension from all side channels is collected at the side channel exit (4).**

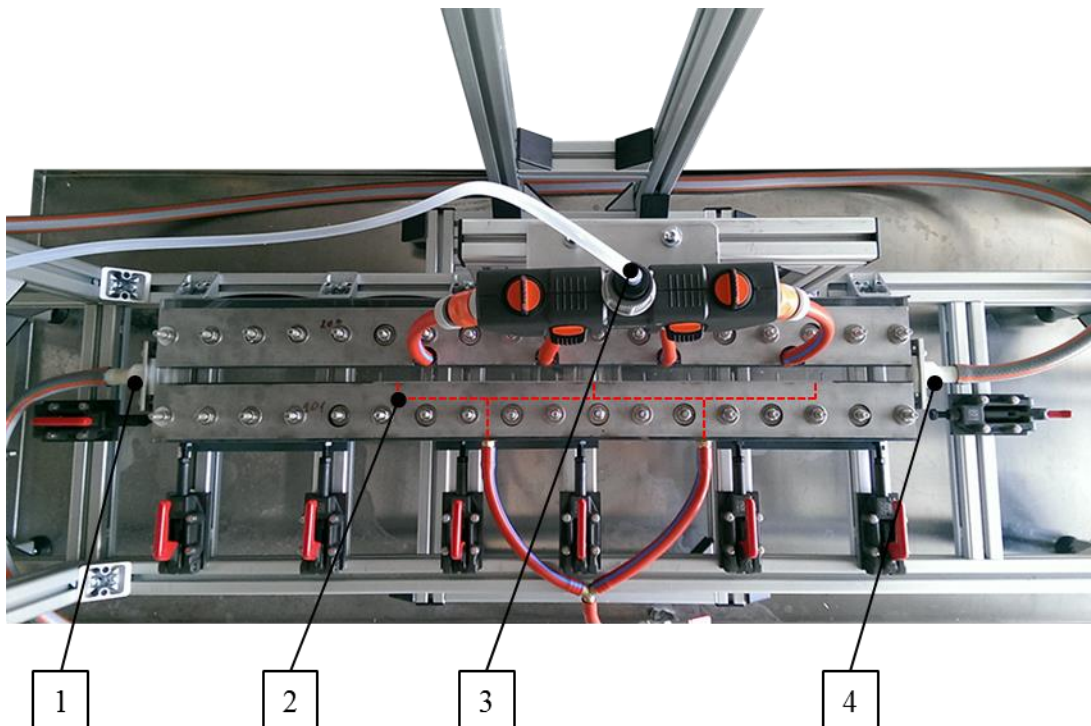


**Fig. 3-5: Top View of the HDF. In the preliminary experiments, all three side channels (2) were used for separation. The water supply (3) was only tested. The main channel inlet (1) and outlet (4) have not changed in the final design.**

### 3.3.1 Operating mode

Initially, the volume flow through the main channel was controlled by a peristaltic pump, just as the side channel flow rate. However, experiments showed strong pulsations in the main channel flow, especially at lower flow rates. These pulsations cause a variation not only in the main channel flow rate, but also in the relative flow fraction that is removed through the side channels. Thus, the separation is not constant over time and varies with the frequency of the pulsations of the peristaltic pump. This disadvantage in terms of separation overcomes the advantage of an easier control of the main channel flow rate compared to the operation with hydrostatic pressure, which always undergoes slight variations.

### 3.3.2 Consistency

In industrial processes, fiber suspensions can be pumped until consistencies of approximately 15%, if additional turbulence is applied at pumping. However, when pumping fiber suspensions through channels or piping with small dimensions in the same order of magnitude as the length of the fibers, plugging becomes an issue and is limiting the pumpable consistency. Starting from a single fiber flock in the suspension attaching to a channel edge, plugging was observed at the main channel inlet at consistencies above 0.5% at channel dimensions of 3 x 15 mm and at high flow rates. When reducing the flow rate, the induced shear forces are lowered, which prevent the formation of fiber flocks. For this very reason, the highest possible consistency gets lower at low flow rates.

### 3.3.3 Pulp

In the preliminary experiments two types of pulp, softwood chemical pulp from *SAPPI Gratkorn* and mechanical pulp from *Norske Skog Bruck*, were used.

Since we expect fibers to align in a distance of half the fiber length away from the channel walls due to wall contact and rotation due to shear forces (see chapter 1.3), the shorter fibers of mechanical pulp can move closer to the channel wall. So the fraction of fibers that is going to be separated is higher for a fiber-length distribution with shorter fibers. The results of the comparison between the two types of pulp supported these considerations. Additionally, the tendency of side channel plugging seemed to be higher when operating the device with mechanical pulp.

### 3.3.4 Side channel plugging

Beside problems with pulsations at the main channel flow when operating with the peristaltic pump, plugging of the side channel was the main problem in terms of operational ease. The higher the flow fraction, the faster the side channels becomes plugged with fibers. Plugging was checked visually, and when needed, the side channel hose was lightly squeezed to free the side channel of fibers. To avoid this inaccuracy in operation, a purging mechanism was installed and used in the later used geometry.

### 3.3.5 Varying side channel flow rates

Another operational problem became visible when the side channel flow rates were decreased to a minimum. Due to the pressure drop in the main channel, the pressure differences between the main channel and the collector-channel are decreasing along the channel direction.

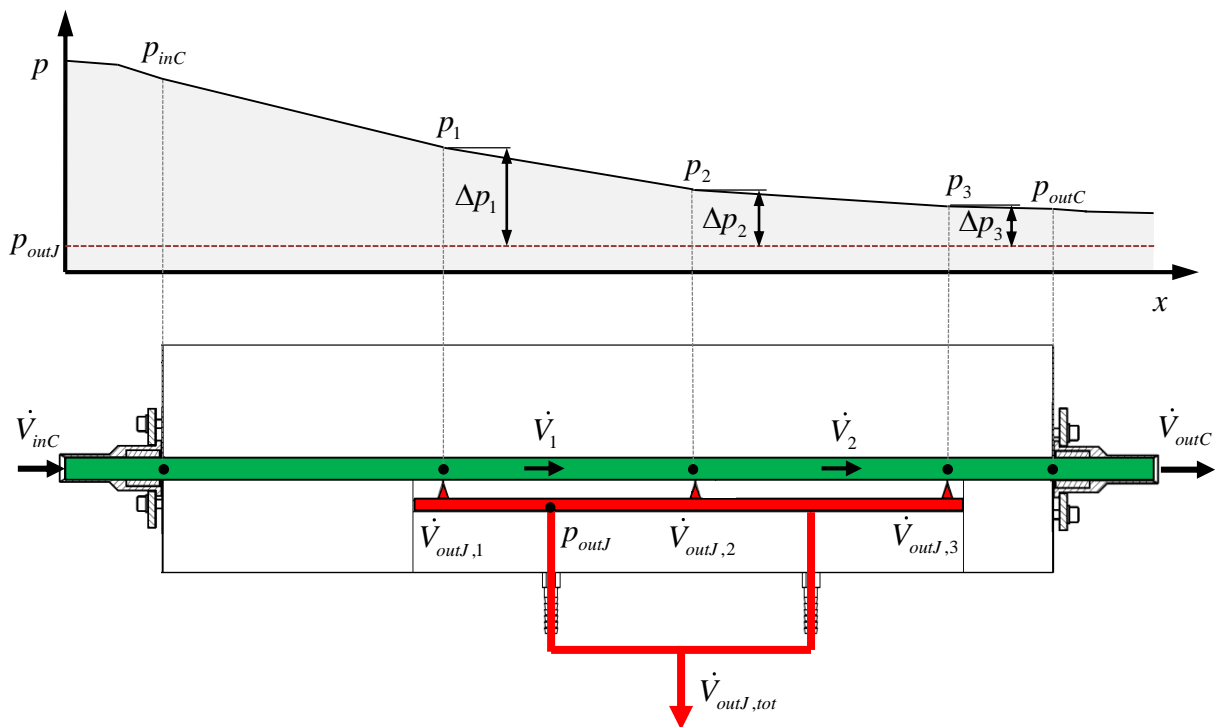


**Fig. 3-6: Pressure drop in the HDF with three operational side channels. The flow rates at the three side channels  $\dot{V}_{outJ,1}$ ,  $\dot{V}_{outJ,2}$  and  $\dot{V}_{outJ,3}$  depend on the respective pressure differences  $\Delta p_1$ ,  $\Delta p_2$  and  $\Delta p_3$ . The slope of the pressure profile along the main channel is decreasing due to the lower flow rates after every side channel.**

Here, we assume constant pressure at the collector channel (red, parallel to the main channel) with pressure  $p_{outJ}$ . To reduce the flow rates through the side channels, this pressure has to be increased. Looking at Fig. 3-6, this would move the red-dotted line with

pressure  $p_{outJ}$  upwards. If this pressure is further increased until  $p_{outJ} > p_3$  is given, fluid flows back from the last side channel into the main channel.

### 3.3.6 Summary of preliminary experiments

The general findings of the preliminary test can be summarized as follows:

- In order to have a continuous, pulsation free main channel flow, the device has to be operated with hydrostatic pressure, since no radial pumps are available at the market for fiber suspensions at the desired flow rates.
- The maximum consistency at the highest possible flow rate is 0.5%, where no plugging of the main channel takes place.
- The separation works better with a wider fiber length distribution. For this reason, long fiber chemical pulp was used for further experiments.
- To overcome plugging of the side channels, a purge mechanism was installed to allow controlled flushing of the side channels with little additional water.
- The side channel flow rates are not equal, and in case of very low flow rates, even backflow takes place. A solution would be to design every side channel with a different side channel width, with smaller dimensions at the upstream side channel and wider dimensions at the downstream side channel. Unfortunately, this would only guarantee equal flow rates at one operating point, so the first two side channels were tightened with silicone to have only one operational side channel. This allows a precise control of the side channel flow rate.

## 3.4 Experimental plan

In order to identify the parameters with the biggest impact on the separation, an experimental plan was established. The idea is to set up a base case and to vary only one parameter to determine its effect on the behavior of the system. This method is commonly termed as “one factor at a time” [26]. An alternative approach, which is not used here, would be to define the matrix of experiments by means of a Design of Experiment (DOE) method. In chapter 3.2, 7 process parameters were identified to determine the system. Since the pulp was set to be softwood chemical pulp after preliminary experiments, 6 process parameters still remain to be investigated.

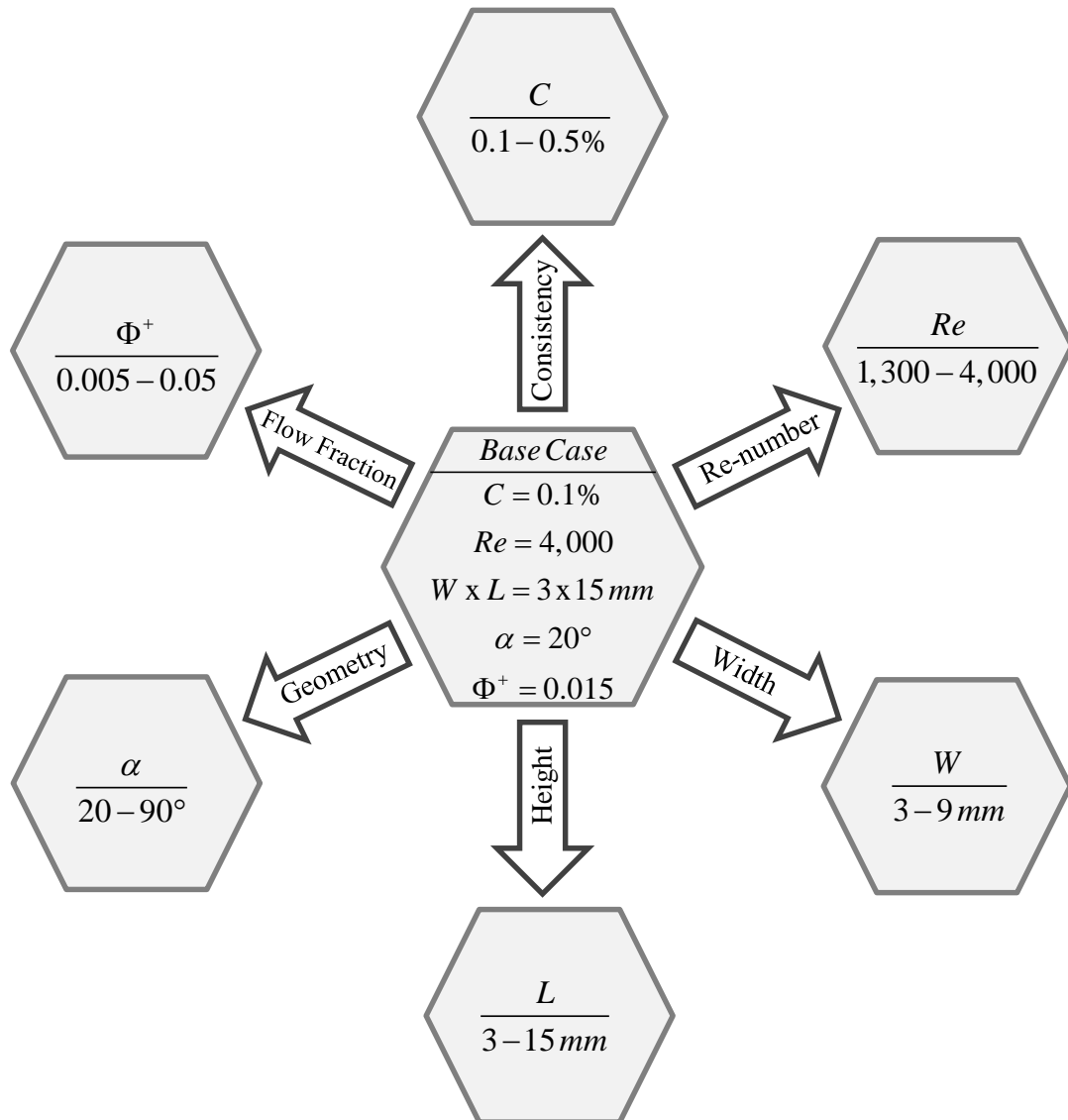


**Fig. 3-7: Variation star with base case in the center and all 6 varied process parameters with their range arranged all around.**

The base case was chosen to have a consistency of 0.1% to prevent plugging of the main channel at lower Reynolds numbers. The Reynolds number of 4,000 was selected due to the maximum flow rate achievable with the given hydrostatic height difference of the setup. The channel dimensions were set to 3 x 15 mm for width and height, the side channel geometry was designed with an angle of 20°, since this resulted in an easier operation due to a lower tendency for plugging. Preliminary experiments suggested setting the flow fraction to a value below 0.03, since the separation performance of long fibers is low below values of 0.03 for  $\Phi^+$ . Thus, the flow fraction at the base case was chosen with 0.015.

### 3.5 Experimental Results

#### 3.5.1 Definition of the separation efficiency

In the following, the results of the experiments are shown, with the aim to show the impact of every process parameter on the separation. As commonly used in process engineering, the separation behavior of an apparatus can be described by the separation efficiency  $T$ , which is in general defined as

$$T(x) = 1 - \frac{\dot{m}_{fines}(x)}{\dot{m}_{inlet}(x)} = 1 - \frac{\dot{m}_{fines} \Delta Q_{fines}(x)}{\dot{m}_{inlet} \Delta Q_{inlet}(x)} \quad (3-2)$$

with the mass flow of the fines fraction  $\dot{m}_{fines}$  and inlet fraction  $\dot{m}_{inlet}$ , and their respective cumulative distribution  $\Delta Q_{fines}$  and  $\Delta Q_{inlet}$ , which are functions of the particle size  $x$  [27]. Another valid definition of the separation efficiency is based on the coarse fraction, but since the fines fraction is of more interest, the above form is used.

The particle size  $x$  has to be replaced by the fiber length  $l_{fiber}$  to account for the present system, and the fines and inlet fraction are denoted with indices  $outJ$  and  $inC$ . We can now write

$$T(l_{fiber}) = 1 - \frac{\dot{m}_{outJ} \Delta Q_{outJ}}{\dot{m}_{inC} \Delta Q_{inC}} \quad (3-3)$$

with

$$\dot{m}_{inC} = \dot{V}_{inC} \rho_{inC} C_{inC} \quad (3-4)$$

$$\dot{m}_{outJ} = \dot{V}_{outJ} \rho_{outJ} C_{outJ} \quad (3-5)$$

Thus, the separation efficiency for the HDF can be determined with the following equation:

$$T(l_{fiber}) = 1 - \frac{\dot{V}_{outJ} \rho_{outJ} C_{outJ} \Delta Q_{outJ}}{\dot{V}_{inC} \rho_{inC} C_{inC} \Delta Q_{inC}} \quad (3-6)$$

An ideal separation of fines would be represented by a step function, with the step at the cut size of fines, by definition 200  $\mu\text{m}$  (see chapter 1.2). The separation efficiency would there change from 0 to 1, meaning that no fibers longer than the cut size are present at the side channel outlet. This ideal separation efficiency cannot be realized, since only a small fraction of fines can be separated, as they are distributed homogeneously over the channel cross-section. However, if the number of longer fibers is kept very low, applying the

separation multiple times leads to an overall separation performance that is not too far off the ideal separation. This overall separation efficiency  $T_{oa}$  can be computed as

$$T_{oa}(l_{fiber}) = T(l_{fiber})^n \quad (3-7)$$

with the number of side channels  $n$ .

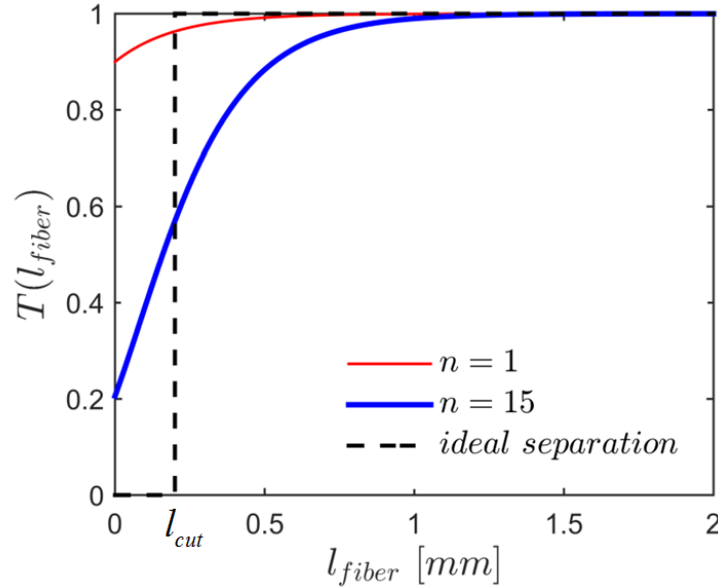


**Fig. 3-8:** Exemplary separation efficiency curve for a single side channel (red) and 15 side channels (blue), compared to an ideal separation with cut size  $l_{cut} = 0.2$  mm (dashed).

In what follows, the error bars have the width of  $\pm 1$  standard deviation. An alternative approach would be to calculate the confidence intervals, as described in Appendix E.2.

### 3.5.2 Effect of Reynolds number

The Reynolds number is directly proportional to the inlet flow rate, thus the relationship with the inlet flow rate is of a linear nature. In pipe flow the transition from the laminar to the turbulent regime takes place at a Reynolds number of 2,300. However, this number also depends on the shape of the inlet, and it has been found that for smooth inlet conditions this number can be much higher [28]. Furthermore, the laminar-turbulent transition of fiber suspension flows is shifted towards higher Reynolds numbers, since fibers stabilize the flow at a certain range of consistency [29]. Thus, the flow in the HDF is assumed to be laminar not only at  $Re = 1,300$ , but also at  $Re = 4,000$ .

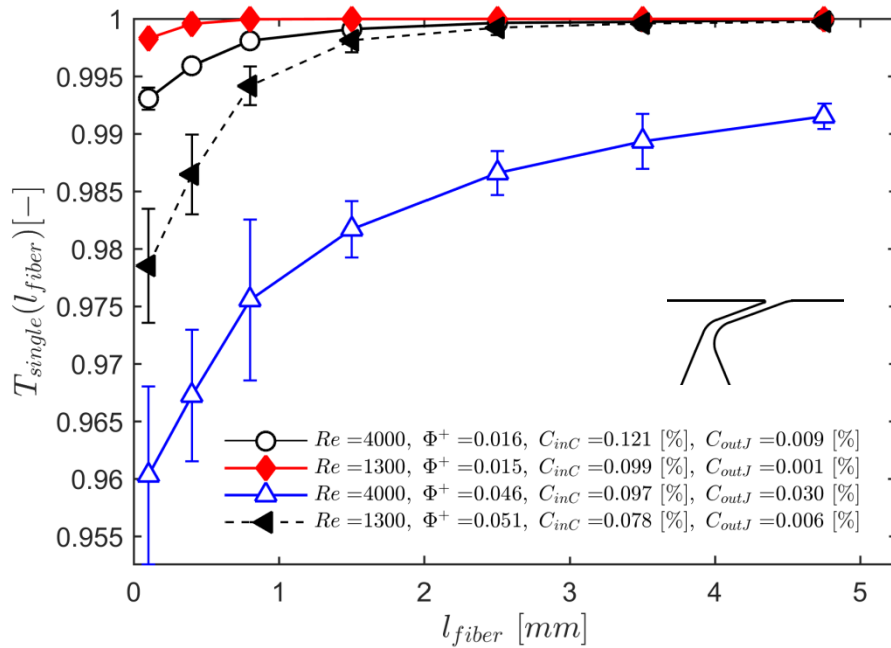


**Fig. 3-9: Separation efficiency for two different Reynolds numbers at two different flow fractions, at channel dimensions of 3 x 15 mm. As expected, more longer fibers are separated at the higher flow fraction of  $\Phi^+ \approx 0.05$ , compared to the standard flow fraction of 0.015. The big impact of the Reynolds number is given at both flow fractions, suggesting that the regime of flow in the main channel plays a major role.**

The results in Fig. 3-9 suggest that the Reynolds number has a big influence on the separation. Experiments were made at two different flow fractions, where the results of both clearly show the impact of the Reynolds number. Comparing experiments with the same flow fraction, less fibers are separated at the side channel for  $Re = 1,300$ . This becomes even clearer when looking at the fiber distributions as shown in Fig. 3-10, the increase at fractions with short fibers is largest at low Reynolds numbers.

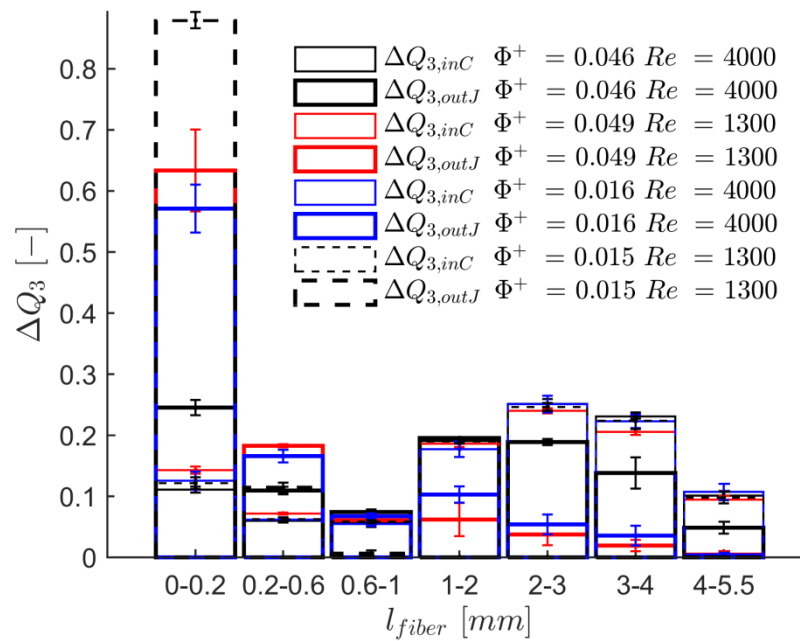


**Fig. 3-10: Distribution of the fibers, based on the results of the *L&W fiber tester*, at the inlet *inC* and side channel *outJ*. The class widths are not equal, since fiber lengths below 1 mm are of major interest. At low Reynolds number and flow fraction, side channel fraction consists of over 85% of fines, which shows the potential of the separation technique.**

The results of both the separation efficiency and the fiber distributions indicate that the distribution of the fibers in the main channel is not equal at different Reynolds numbers. The situation of the channel flow around the side channel entry was therefore investigated by means of high-speed imaging. Fig. 3-11 shows images that were taken with a high-speed camera at a frequency of 3,000 images per second.

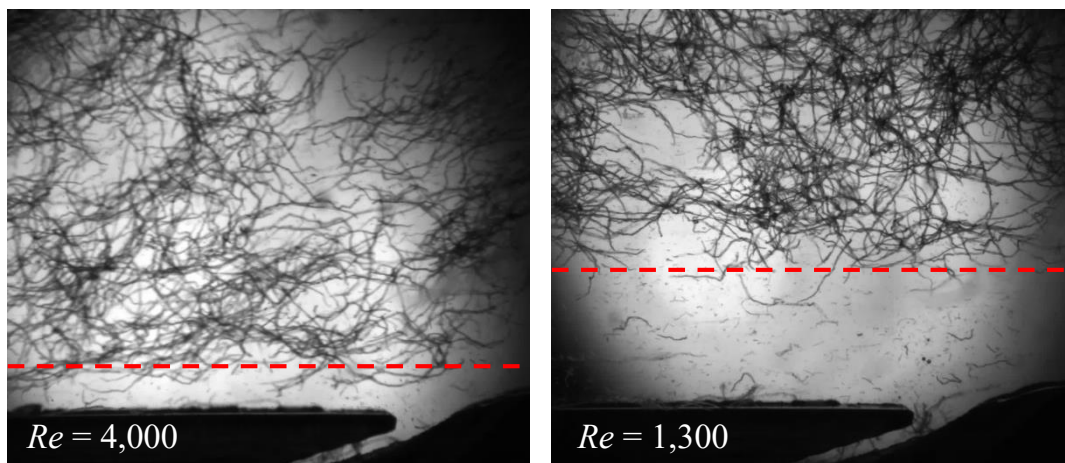


**Fig. 3-11: Image of the main channel at the side channel entry at two different Reynolds numbers at a consistency of 0.1%. At  $Re = 4,000$ , the fibers are distributed over the channel, while at  $Re = 1,300$  the fibers are moving bound in a network through the channel. Thus, fibers reside mostly in the region from the channel center to the red-dashed lines.**

Clearly, the fibers are more distributed over the channel at  $Re = 4,000$ , while at  $Re = 1,300$  the fibers flow through the channel in a network that is aligned at the channel center,

leaving a zone with a very low fiber concentration near the walls. Although these images show the situation only for one time instance, this phenomenon was observed at almost all of the 1,000 images taken during the experiment. Since the number of fibers near the side channel is lower at  $Re = 1,300$ , less fibrous material is entering the side channel, explaining the differences for the results for the separation efficiency.

A possible explanation for that is, that the shear stress experienced by the fibre network in the main channel is higher at  $Re = 4,000$  because of the higher mean velocity. The resulting shear forces act against the forces between fibers and prevent the formation of fiber networks. For this reason, fibers are able to move relative to each other, even only for small distances. Thus, the distribution over the main channel is more homogeneous compared to the situation at  $Re = 1,300$ , where the formation of a fiber network takes place, which is moving towards the channel center driven by the forces acting on it.

While this explains the difference in the separation characteristics of long fibers, the question why also fines are removed to a lower extent remains unanswered here. Ajersch [30] compared the fines fraction in fiber networks, i.e. fiber flocks, and in the region between these networks. He concluded that the fines are excluded from the flocks to a small extent. This would mean that the fines fraction in the wall near region could be slightly higher than in the center of the channel, which enhances the separation efficiency. Unfortunately, this speculation could not be supported with data in the present work.

### 3.5.3 Effect of consistency

The maximum consistency in the experiments in the HDF was determined to be 0.5%, above which plugging of the main channel became a problem. In Fig. 3-12, the results for experiments with two different consistencies of 0.5 and 0.1% and two flow fractions are shown. Experiments were only made at a Reynolds number of 4,000, because operation at lower Reynolds numbers was not possible at this consistency.

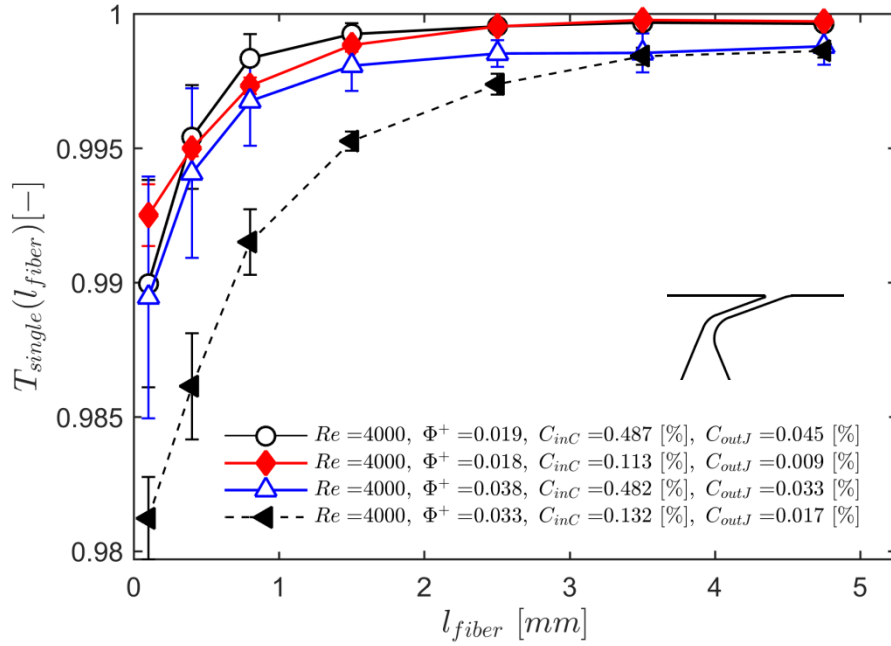


**Fig. 3-12: Separation efficiency for inlet consistencies of  $C_{inC} \approx 0.5\%$  (white markers) and  $C_{inC} \approx 0.1\%$  (filled markers). At low flow fractions, no significant difference could be observed. However, at a flow fraction of  $\Phi^+ > 0.33$ , the amount of fibers removed is roughly increased by a factor 2 at higher consistency.**

Interestingly, separation efficiency curves at lower flow fractions do not show significant differences, while at higher flow fractions more fibers were separated at lower consistency. This is somehow surprising, since one would expect that more fibers are separated if the consistency was higher, where more fibers are in the channel.

Furthermore, the concentration profiles of fibers in channels at low consistencies were studied by various authors [15][31], showing a linear increase of the fiber concentration with the wall distance until a nearly constant bulk concentration of fibers is reached at a distance of  $0.31 \cdot l_{fiber}$ . At higher consistencies, this distance is reduced by two thirds, which means that longer fibers are closer to the wall when increasing the consistency.

A reason for this discrepancy might be that at  $C = 0.5\%$  especially long fibers have many contact points with other fibers due to the higher concentration. Thus, even in case hydrodynamic forces “pulling” the fiber towards the side channel exit are present, the fiber is still fixed to the fiber network.

### 3.5.4 Effect of side channel geometry

The geometry of the side channel entry is crucial for the flow field near the entry of the side channel. Since the hydrodynamic forces acting on fibers are of key importance for

separation, it is essential to have a look at this very detail. Additionally, the geometry also determines the pressure drop across the side channel, which contributes to the overall energy consumption of the device.

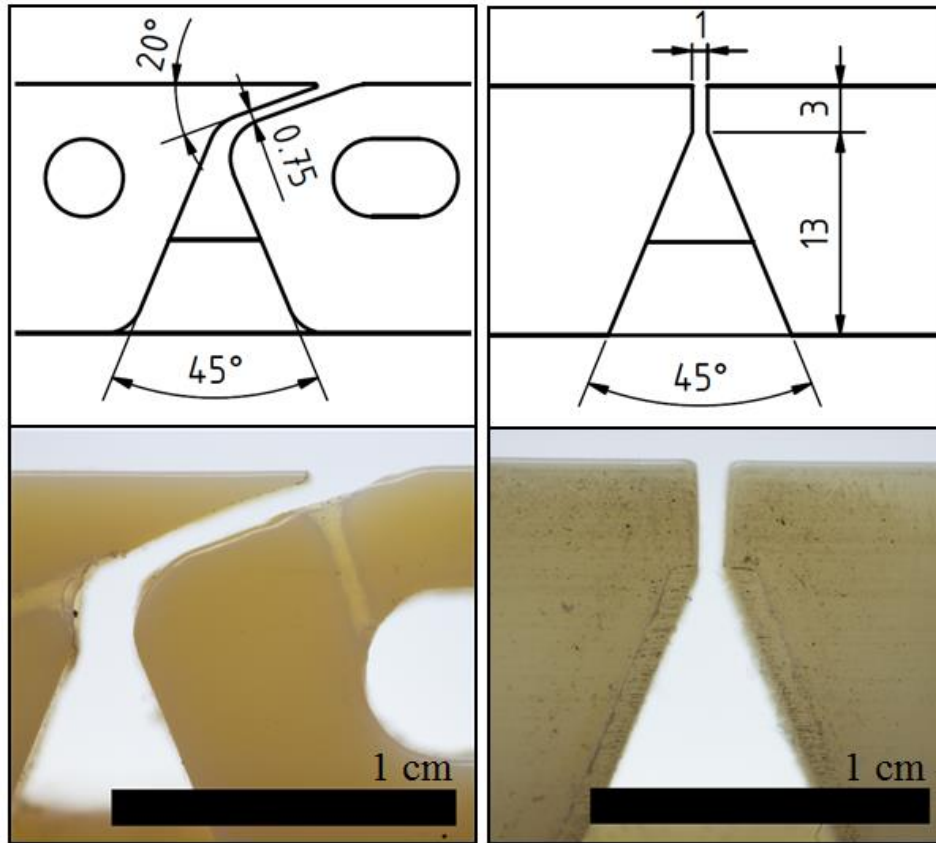


**Fig. 3-13: Drawings of the used geometries (top) and images of the printed parts. Clearly, the side channel width in the 20° standard-geometry (left) is roughly the same as at the 90° geometry (right), but should only be 0.75 mm, while the side channel width of the 90° geometry was designed with 1 mm.**

The 90° geometry depicted in the right panel of Fig. 3-13 represents a simple side channel geometry, since it is just a T-channel. This geometry was used as a first basic design because of its simplicity. The side channel height is 1 mm, and the length of the side channel is 3 mm. The separation process takes only place at the side channel entry, so the length of the side channel is designed short to reduce the pressure drop.

Subsequent to the preliminary experiments, the 20° geometry was designed. Its acute entrance angle hinders longer fibers to follow the flow field, and even if a single fiber temporarily deposits at the side channel entry, there is no sharp edge where it could get stuck. Two options for purging were designed, one at the side channel perpendicular to the side channel, and one in side channel direction. Both channels are visible in Fig. 3-13, since the low wall thickness at the purge channels result in a certain transparency of the 3D-printed parts. Tests suggested the use of the second option, since it guarantees purging

of the side channel even if a fiber became stuck in the middle of it, while this was not the case for the first option. The side channel width was designed with 0.75 mm.

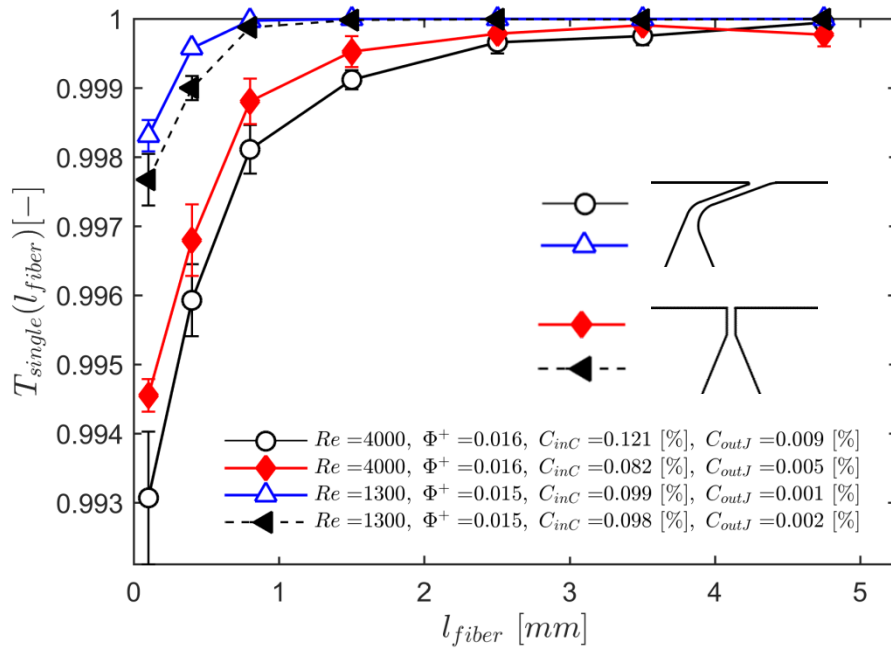


**Fig. 3-14: Separation efficiency curves for two different geometries, showing only a small impact of the geometry on the separation characteristics of the device. At higher Reynolds number, the 90° geometry performs slightly better, because the fraction of fines separated is nearly equal to the 20° geometry, while only half of the fibers longer than 2 mm are separated.**

The difference in the separation efficiency curves of both geometries is low, indicating the low influence of the geometry on separation. However, the difference in operation is big, since for the 90° geometry purging was necessary every 2.5 seconds at  $Re = 4,000$ , and every 20 seconds at  $Re = 1,300$ . The tendency for plugging of the side channel at the 20° geometry is much lower. A continuous operation was possible at a purge frequency of 1 per minute, at low flow fractions this period can be even extended.

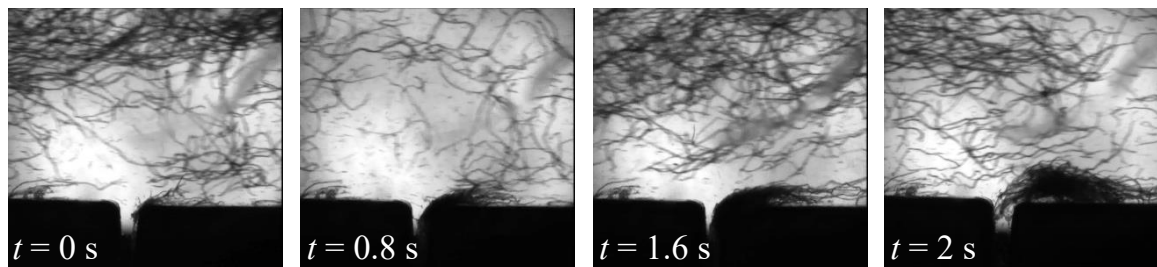


**Fig. 3-15: Situation at the side channel entry at  $Re = 4,000$ , and 3 x 15 mm channel dimensions. Despite the low flow fraction  $\Phi^+$  of 0.016, the side channel is nearly fully blocked after 1.6 seconds. To free the side channel again, the side channel was purged with water, which forces the deposited fibers back into the main channel. This is shown in the right image, at time  $t = 2$  s.**

Interestingly, a research group in Japan studied the influence of the side channel shape on the separation of spherical and non-spherical particles [9][13][14]. One of their results was

that for rod-like particles, i.e., fibers, a side channel geometry with a sharp angle hinders those particles to enter the side channel.

In our case of the  $20^\circ$  geometry, the fibers collide with the wall at the side channel entry and get back into the main channel again, which prevents the side channel from plugging. Keeping the side channel angle this low seems to be very important for hydrodynamic filtration of fiber suspensions, as it is crucial for operational ease.

One problem at the experimental determination of the separation efficiency was the swelling behavior of the 3D-printed material. When in contact with water for a long time, the printing material which includes the side channel, fabricated with the Polyjet technology (see Chapter 2.3), changed its geometry. Because of this issue, the side channel width was not constant, i.e., 0.75 mm as designed.

### **3.5.5 Effect of the side channel flow rate**

The absolute value of the side channel flow rate is not of interest, so the flow fraction  $\Phi^+$  was defined previously, relating the side channel flow rate to the main channel flow rate. Since the distribution of fibers and fines over the main channel is not equal, as shown in the results before, the height of the liquid layer that is removed, which is in fact a suspension layer here, plays an important role at hydrodynamic filtration. The experiments with different flow fractions were done at a Reynolds number of 4,000, at the  $20^\circ$  geometry.

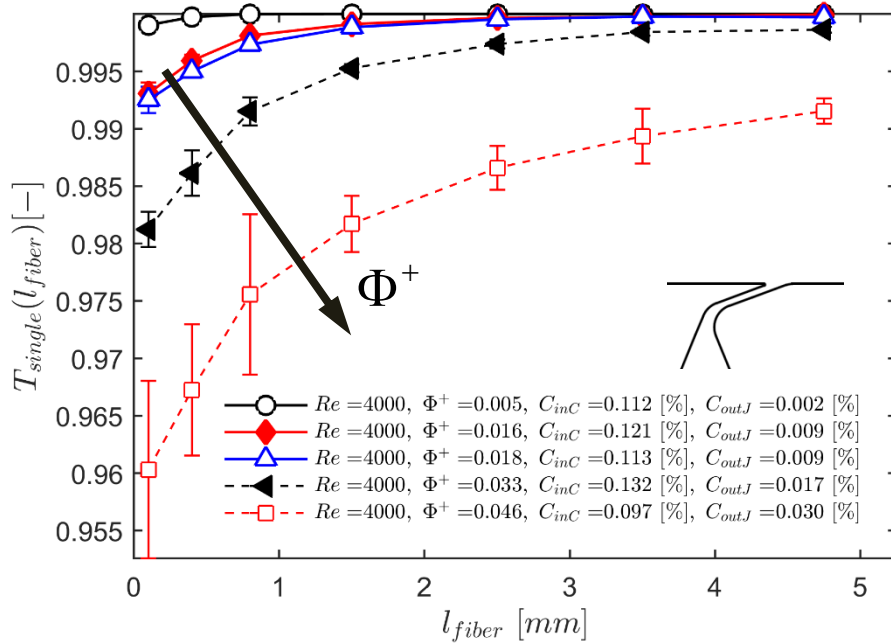


**Fig. 3-16: Effect of the flow fraction  $\Phi^+$  on the separation, showing that an increase of the side channel flow rate results into lower separation efficiencies for the 3 x 15 mm standard geometry.**

As expected, higher flow fractions lead to more separated fibers. Interestingly, the fraction of longer fibers that are separated dramatically increased between the two highest flow fractions of  $\Phi^+ = 0.033$  and  $0.046$ . This suggests that the amount of long fibers in the removed liquid layer is increasing above  $\Phi^+ = 0.033$ . Consequently, this means that the height of the liquid layer is bigger than the distance between the wall and the region of low concentration of long fibers. For the given pulp and a Reynolds number of 4,000, this value marks a critical flow fraction, above which the separation behavior is not satisfying, since too many long fibers are separated.

At different Reynolds numbers the height region with low concentration of longer fibers increases, as discussed in Chapter 3.5.2. For this reason, no longer fibers are separated even at higher flow fractions, which can be seen in Fig. 3-9. At flow fractions of 0.05, no significant increase in the separation of longer fibers can be seen at  $Re = 1,300$ . A higher flow fraction can thus be chosen at lower Reynolds numbers.

### 3.5.6 Effect of channel height

The general design of the HDF with a rectangular main channel, where suspension is removed at only one edge, allows the investigation of both the channel height and width, because the impact of each is not equal. While at different channel heights, the cross-sectional area of the side channel stays the same, different channel widths also change the

size of the side channel. For this reason, both parameters are investigated separately. The separation efficiency was carried out for channel heights of 15 and 9 mm at two different Reynolds numbers, the channel width was 3 mm in all cases. Experiments at 3 mm channel height failed because of plugging of the main channel.

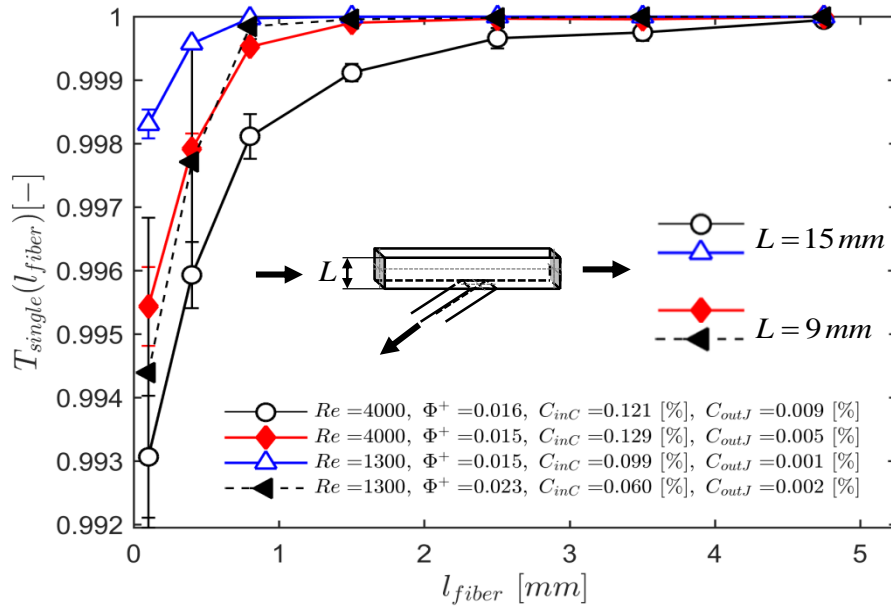


**Fig. 3-17: Separation efficiency for the standard channel height of 15 and 9 mm, and the standard channel width of 3 mm. For smaller channel heights the effect of the Reynolds number is not visible anymore, and the separation performance is between the ones with 15 mm channel height for a low and high Reynolds number.**

The results in Fig. 3-17 are interesting, since the separation efficiency is more or less identical at both Reynolds numbers and for a channel height of 9 mm. This would mean that the effect of fibers positioned more likely in the middle of the channel at low Reynolds numbers would not be as strong as at a channel height of 15 mm. However, due to limitations of the adjustment of the side channel flow rate, the lowest possible flow fraction at the lower Reynolds number was set to 0.023 at the 9 mm channel. Thus, the separation efficiency curve at this case is expected to be slightly above the curve of the experiment with the higher Reynolds number. Furthermore, the error bars are indicative that the results should be treated with care. This is caused by deviations in the consistency, which is fluctuating at lower flow rates, in contrast to higher flow rates for which consistency can be easily kept constant. Since the exact reason for this fluctuation of the consistency, we avoid any speculation on its origin.

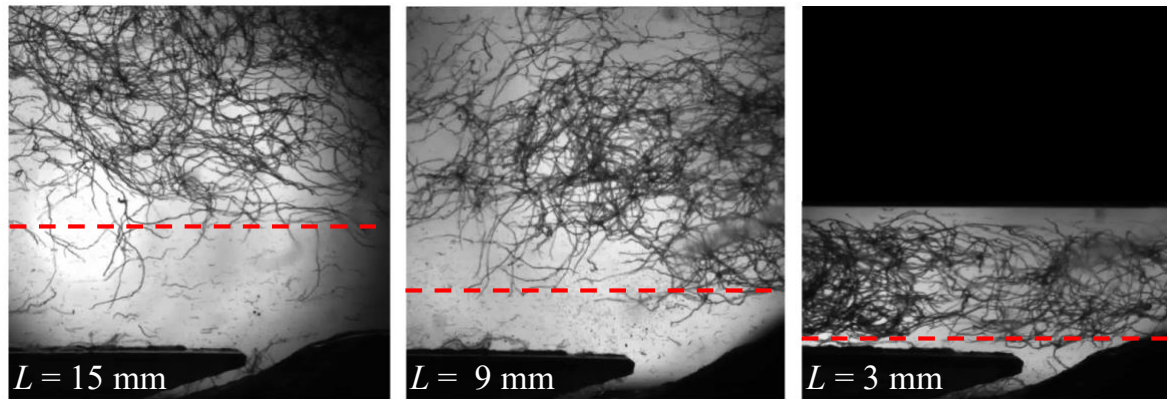


**Fig. 3-18:** Situation in the main channel at 3 different channel heights at  $Re = 1,300$ . The fiber network is located in the channel-center, but its size perpendicular to the channel axis seems to be roughly constant. For this reason, the nearly fiber-free area close to the wall gets smaller with decreasing channel height, lowering the impact of the Reynolds number on the separation.

A closer look at the flow situation in the main channel gives a possible answer for the observed behavior. The size of the fiber network in the channel center seems to have a similar size. Thus, the region with lower concentration of long fibers becomes smaller at lower channel-heights. This becomes even more visible at the very small channel height of 3 mm, where the main channel gets plugged very easily. For this reason it was not possible to determine the separation efficiency at that channel height. All images are shot at  $Re = 1,300$ ; at  $Re = 4,000$  the fibers were again distributed more evenly across the channel, which is not shown here.

Overall, the difference in the flow regimes seems to become smaller at decreasing channel height. It is speculated that this is due to the size of the fiber network, which is almost independent of the channel height, leading to a narrower zone with low fiber concentration near the wall.

### 3.5.7 Effect of channel width

Changing the main channel width also changes the cross-sectional area of the side channel, thus it simply results in a geometric stretching of the system in one direction. From an economic point of view, an increase in the channel width is associated with lower energy costs, since the pressure drop decreases with wider dimensions. This pressure drop, as shown later, is crucial for the overall energy consumption of the HDF.

The previous experiments were all performed at a channel width of 3 mm, while for the analysis of the impact of the channel width also experiments with a channel width of 9 mm were made.

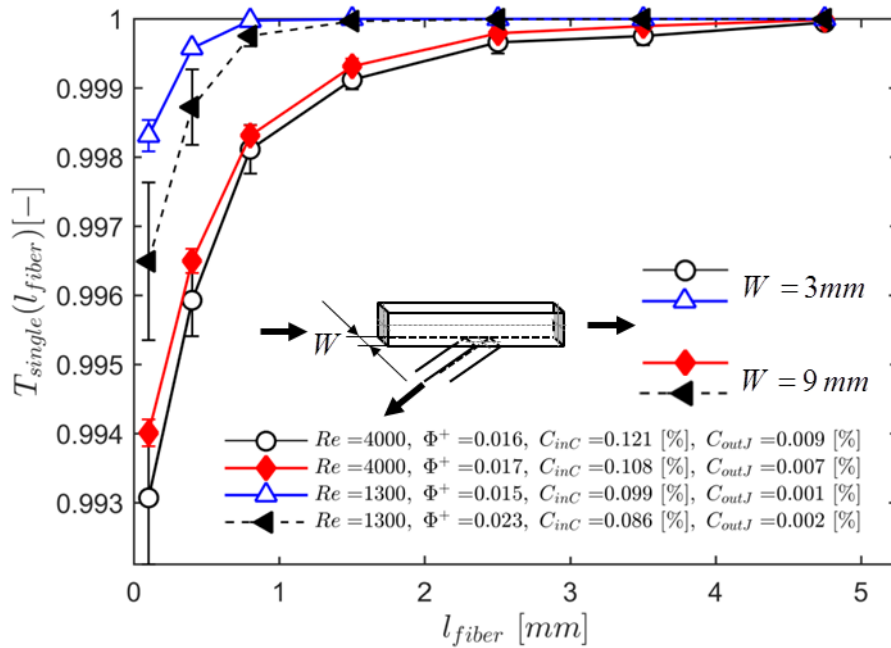


**Fig. 3-19: Separation efficiency for different channel widths at Reynolds numbers of 1,300 and 4,000, as well as low flow fractions. Only for the lower Reynolds number, a difference in the separation efficiency was observed, where more fibers are separated in the wider channel. This was also due to the higher flow fraction, caused by limitations associated with the operation of the side channel pump.**

At low flow fractions, the difference between the channel widths is quite low, especially at the higher Reynolds number of 4,000. At  $Re = 1,300$ , more fibers are separated at a channel width of 9 mm. However, since the flow fraction at  $Re = 1,300$  is 0.023, due to the lack of a possible variation of the side channel flow rate, the separation efficiency curve is expected to be similar to the curve for the channel width of 3 mm.

Another set of experiments were performed with higher flow fractions of 0.05, as shown in Fig. 3-20. The separation efficiency is similar in both cases, with slightly more separated fibers at a channel width of 3 mm.

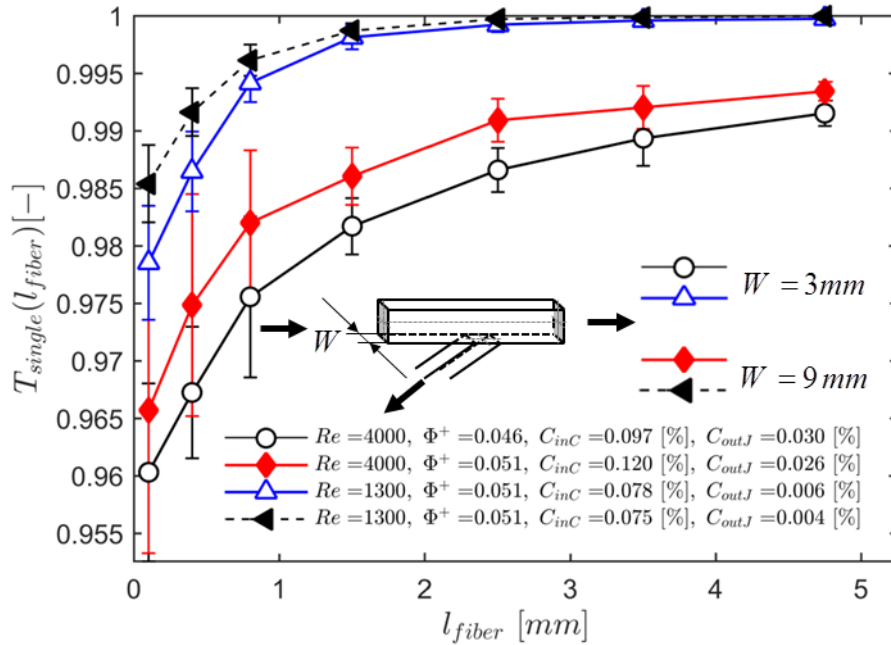


**Fig. 3-20: Separation efficiency for different channel widths at Reynolds numbers of 1,300 and 4,000, and at high fractions.**

At a channel with of 3 mm, fibers cannot orientate randomly in any position, since the range of fiber lengths is up to 6 mm long fibers. In case the channel width and height exceeds the length of the longest fibers, which is the case at a channel dimension of 9 x 15 mm, this is possible as illustrated in Fig. 3-22.

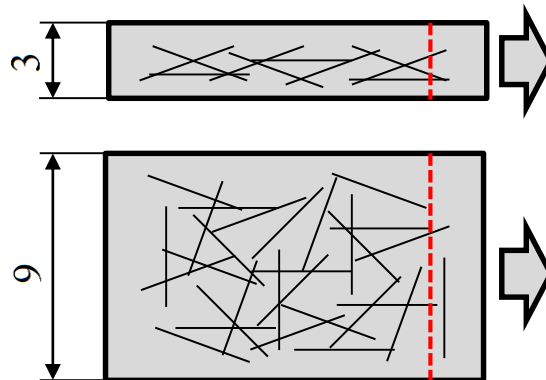


**Fig. 3-21: Possible orientations of fibers within the channel. Fibers longer than the channel width are hindered to orient vertically.**

Following this theory, one would expect more long fibers to be separated at wider channels, because of the additional possibilities of fiber orientations in the separation zone. However, this is not the case as shown in the results for the separation efficiencies. Fibers tend to be oriented in stream wise direction, because the angular velocity of the fibers is smaller at these positions in channel direction. Thus, fibers are unlikely to be oriented vertically in the channel.

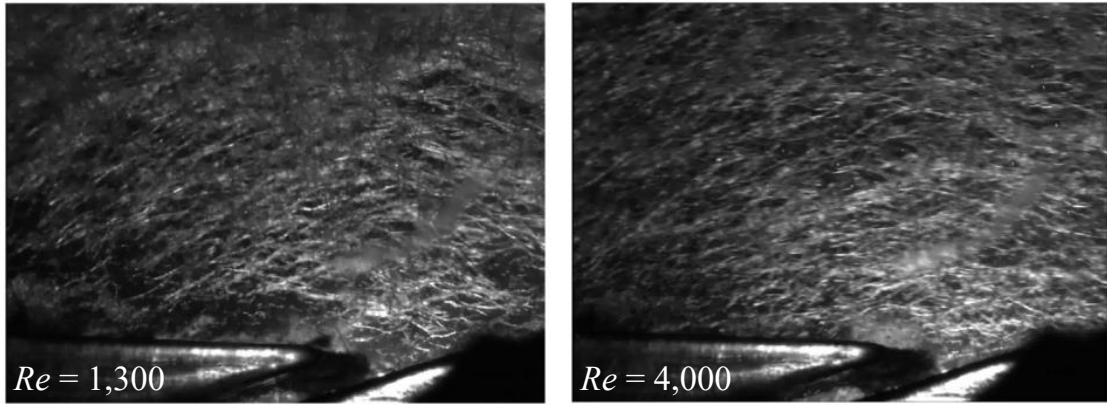


**Fig. 3-22: Fiber flow at 9 mm channel width at two different Reynolds numbers and a consistency of 0.12%, at a flow fraction of 0.017 (left) and 0.022 (right). Note, not all fibers are in focus in these images.**

Both findings on the influence of the Reynolds number and the flow fraction can be found also in the results for the analysis of the channel width, since the results do not vary significantly. At  $Re = 1,300$ , the number of longer fibers is clearly smaller near the wall, compared to  $Re = 4,000$ , which can be seen in Fig. 3-22. The impact of the width on the separation is small, so it can be chosen higher to reduce the pressure drop in the main channel. Also, the number of main channels can be kept lower if the dimensions are large, in order to have the same throughput in a future multi-channel HDF device.

### **3.6 Model function for the separation efficiency**

In the previous sections, results for the experiments at different starting parameters were shown. The logical next step is to find a way to interpret these results also with a mathematical relationship. Developing a model function to predict the separation efficiency curve as a function of input parameters would be a goal for future work, and hence is out of the scope of this thesis. Instead, a mathematical function has been postulated describing the separation efficiency with three parameters.

$$T(l_{fiber}) = T_{max} - e^{-\frac{l_{fiber}}{l_{cut}}} (T_{max} - T_{min}) \quad (3-8)$$

The parameters  $T_{min}$  and  $T_{max}$  represent the separation efficiency for fibers with a length of  $l_{fiber} = 0$  and  $l_{fiber} \rightarrow \infty$ , respectively. The cut size  $l_{cut}$  defines the shape of the curve, and provides information about the typical fibre length at which the separation takes place. Ideally,  $l_{cut}$  should take low values when aiming at the separation of short fibers. In case no long fibers are separated, the parameter  $T_{max}$  should equal unity. A low value of  $T_{min}$  is

desired, since the fraction of fines remaining in the main channel should be as small as possible.

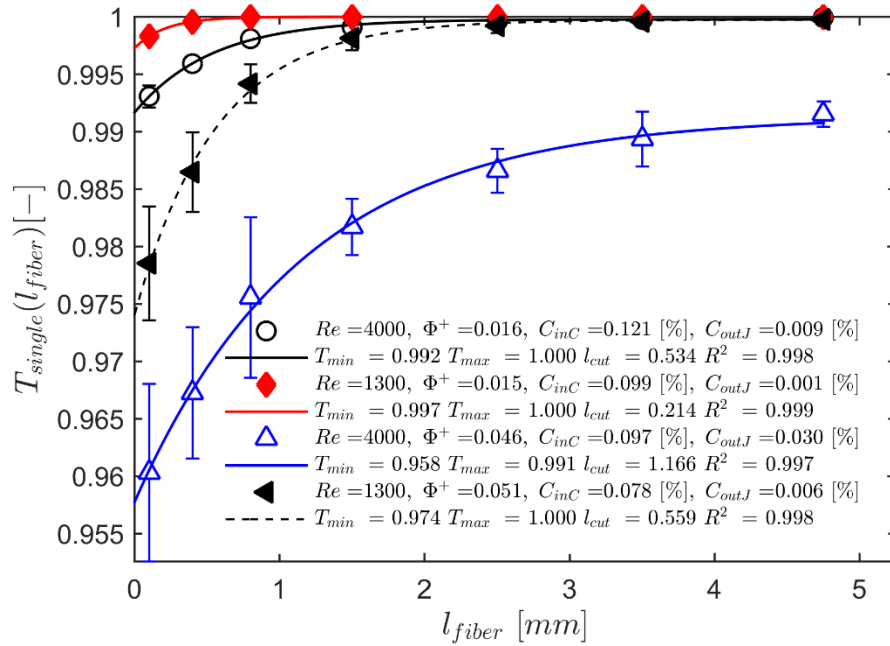


**Fig. 3-23: Separation efficiency for different Reynolds numbers and flow fractions (symbols) approximated by the model function (lines), showing good agreement between model function and experimental results. The model function, equation (3-8), was fitted using MATLAB.**

When fitting experimental data with equation (3-8), excellent agreement between the model function and the experimental data can be achieved. In this example, the maximum separation efficiency  $T_{max}$  at higher Reynolds number and flow fraction is 0.991, suggesting that long fibers are present in the side channel. The results for the experiments are given in Table 3-1 for different process parameters. Note, that the coefficient of determination  $R^2$  is close to 1 in all cases.

**Table 3-1: Parameters for the model function describing the separation efficiency.**

<i>Re</i>	<i>Width</i>	<i>Height</i>	<i>Geometry</i>	$\Phi^+$	$C_{inc}$	$T_{min}$	$T_{max}$	$l_{cut}$	$R^2$
[-]	[mm]	[mm]	[deg]	[-]	[%]	[-]	[-]	[mm]	[-]
4,000	3	15	20	0.019	0.487	0.987	1	0.354	0.999
4,000	3	15	20	0.038	0.482	0.987	0.999	0.436	0.999
1,300	3	15	90	0.015	0.098	0.997	1	0.322	0.994
4,000	3	15	90	0.016	0.082	0.993	1	0.479	0.996
1,300	3	15	20	0.015	0.099	0.993	1	0.214	0.999
1,300	3	15	20	0.051	0.078	0.974	1	0.559	0.998
4,000	3	15	20	0.005	0.112	0.998	1	0.226	0.999
4,000	3	15	20	0.016	0.121	0.992	1	0.534	0.998
4,000	3	15	20	0.018	0.113	0.991	1	0.667	0.999
4,000	3	15	20	0.033	0.100	0.979	0.999	0.828	0.999
4,000	3	15	20	0.046	0.097	0.958	0.991	1.166	0.997
1,300	3	9	20	0.023	0.060	0.992	1	0.302	0.993
4,000	3	9	20	0.015	0.129	0.994	1	0.353	0.998
1,300	9	15	20	0.023	0.086	0.995	1	0.289	0.999
1,300	9	15	20	0.051	0.075	0.982	1	0.530	1.000
4,000	9	15	20	0.017	0.108	0.993	1	0.552	0.999
4,000	9	15	20	0.051	0.120	0.963	0.993	0.853	0.992

### 3.7 Velocity Profiles recorded via Particle Image Velocimetry

Particle Image Velocimetry (PIV) is widely used in particle technology for the determination of velocity fields. It is based on the principle of pattern recognition, where the movement of these patterns within two images is determined. In so-called interrogation windows, the light intensity distribution is measured. By the use of a cross correlation algorithm, the movement of objects in each interrogation window can be calculated. In combination with the time between two images, the velocity can be calculated.

To get the flow field within a fluid, particles are suspended over the region of interest, whereby the density and the size of the particles should be small in order to ensure that the particles are following the fluid flow field as good as possible. Therefore, the Stokes number as given in Eqn. (3-9) should be below 0.1.

$$Stk = \frac{\rho_p}{\rho_{fluid}} \frac{d_p^2 u_{ref}}{18\nu D} \quad (3-9)$$

In this work, the MatPIV [32] package for MATLAB was used to implement a PIV analysis, together with existing subroutines for the processing of multiple sets of images [33]. When applying PIV for the determination of the flow field of a fibrous suspension, one faces multiple problems. First, fibers are not distributed over the whole cross section, which means that in some areas PIV will not work, since no patterns are detected. This is illustrated in the exemplary results shown in Fig. 3-24.

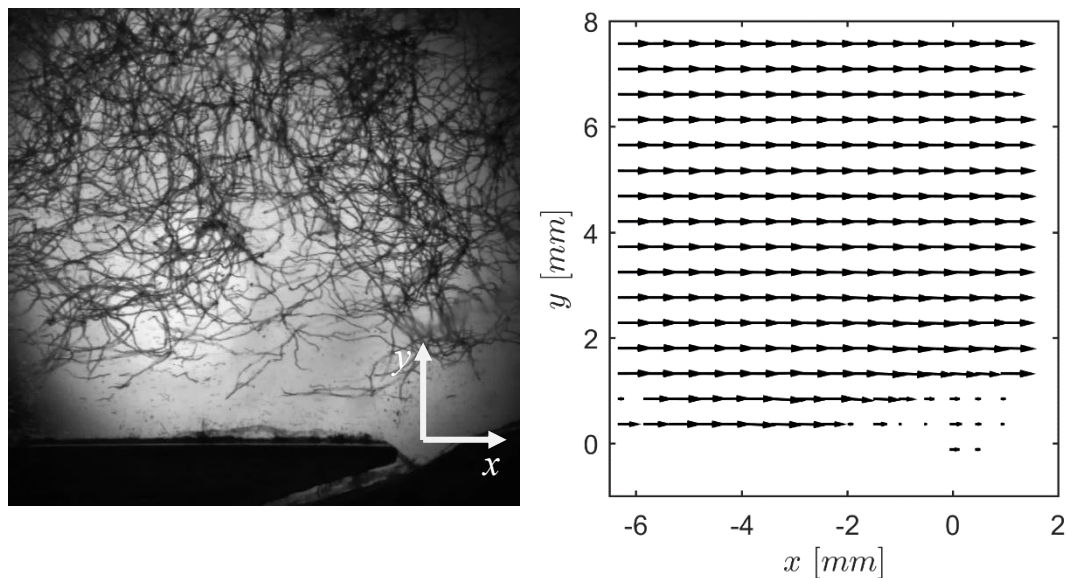


**Fig. 3-24: Image of the channel flow (left panel) and the resulting velocity field determined with PIV (right panel), at  $Re = 1,300$  and  $\Phi^+ = 0.045$  in the  $3 \times 15$  mm channel.**

Another problem becomes visible when looking at the results for flow field around the fiber network near the channel center: here it looks like that over a wide region plug flow is present, since the velocity vectors are all of the same length. This is due to the fact that fibers are not really mobile in that network, thus in fact the fiber velocity is measured, meaning that no accurate reproduction of the fluid flow field can be done.

However, at least in the wall near region, where the fiber concentration is low, the flow field can be approximated by simply averaging the results over a large number of images.

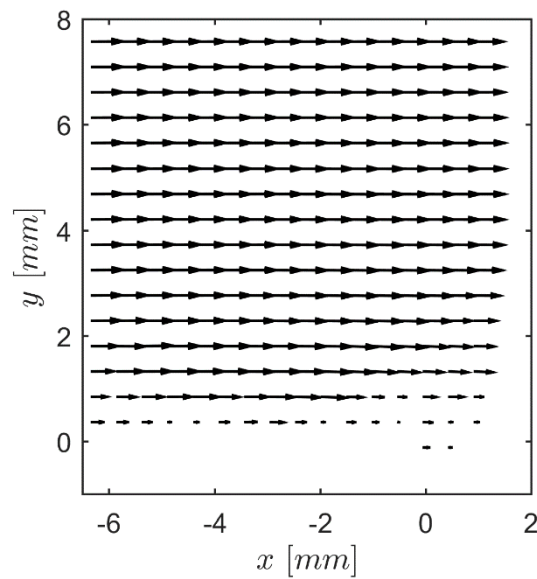


**Fig. 3-25: Flow field with averaged values over 1,000 images at  $Re = 1,300$  and  $\Phi^+ = 0.045$  in the 3 x 15 mm channel. The velocity is decreasing at  $y$  values lower than 2 mm.**

In order to track the rotation of a fiber in the flow, other measurement techniques like Particle Tracking Velocimetry (PTV) have to be applied. Since the concentration has to be very low to be able to identify single fibers on images, PTV was not considered here.

## 4 Single phase simulations

Single phase simulations are performed to evaluate the pressure drop not only experimentally, but also by means of simulation and to have an insight on the flow field in the HDF. At the IPPT, the open-source software package OpenFOAM® is used for single phase simulations, as well as for multiphase flow simulation in combination with LIGGGHTS®. However, simulations of fiber suspensions are still in an early stage and much more complex. Thus, we focus on the fluid phase only in what follows.

### 4.1 Simulation strategy

In conventional CFD-tools, the general sequence is:

1. Determination of the geometrical situation of the problem
2. Generation of the mesh, i.e. decomposition of the domain
3. Selection of an appropriate model, e.g. RANS, LES, DNS
4. Selection of numerical schemes
5. Definition of boundary conditions and initial values
6. Running the simulation
7. Post-Processing of the data, e.g. to get pressure-time curves

In our simulations DNS is used, which is the current state of the art choice for detailed simulations of smaller simulation domains. When using DNS, turbulence phenomena are simulated directly, thus no turbulence model is used. This requires a small size of individual cells in the regions of interest, which in our case is the region near the side channel entry.

A detailed description of the simulation parameters as well as the discretization schemes is given in Appendix D, while the geometrical situation is shown in Fig. 4-1. Simulating the whole flow field would require huge computational effort, and is not necessary since we assume a laminar flow regime over the total length of the main channel. König [34] showed that for a similar geometrical situation an inlet and outlet length of approximately 5 times the characteristic length of the channel cross section gives meaningful results. The idea behind the simulations is to get values for the flow fraction  $\Phi^+$  at different pressure

differences  $\Delta p^+$ . Since the reference velocity in the simulations is the inlet velocity  $\bar{u}_{inC}$  and is set to 1, the pressure is normalized with:

$$p_i^+ = \frac{P_i}{\rho \bar{u}_{inC}^2} = \frac{P_i}{\rho} \quad (4-1)$$

The pressure at the face  $out_C$  was set to 0 in all simulations, while the pressure at the side channel outlet  $out_J$  was varied. Note, that  $\Delta p^+$  can also take positive values, since the pressure at the side channel entry is different from the pressure at the main channel outlet due to the pressure drop along the main channel. The flow profile at the inlet face  $in_C$  was imposed to be that of a laminar flow in a rectangular channel.

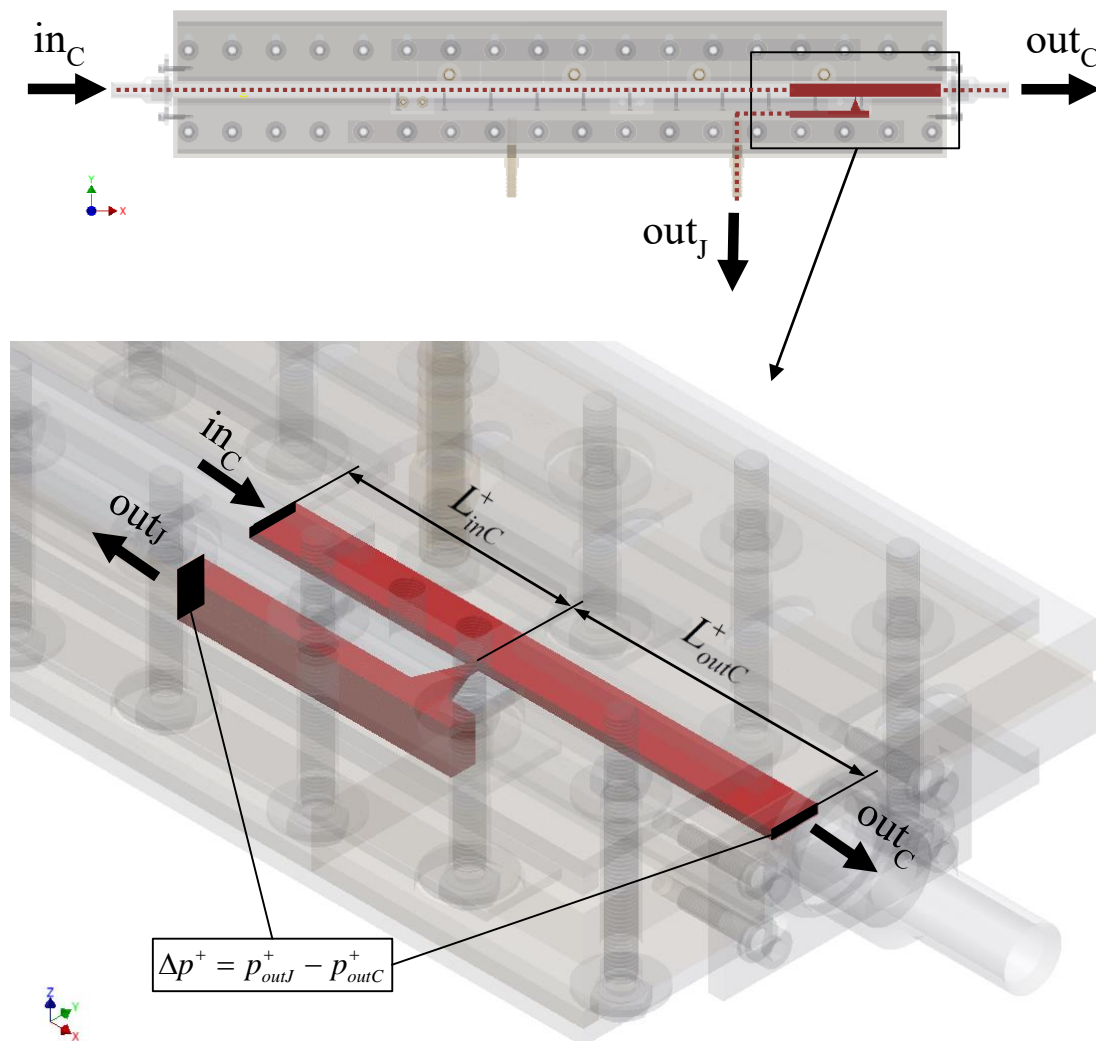


**Fig. 4-1: HDF with the simulation domain (red) for the 90° geometry, with the inlet face  $in_C$  and the two outlet faces  $out_C$  and  $out_J$ .**

Simulations were performed for channel geometries of 3 x 15 mm considering both geometries. Unfortunately, the Reynolds number had to be set to 500 in order to guarantee a reasonable grid resolution for DNS at a total number of cells in the range of 750k.

## 4.2 Simulation results

### 4.2.1 Velocity field

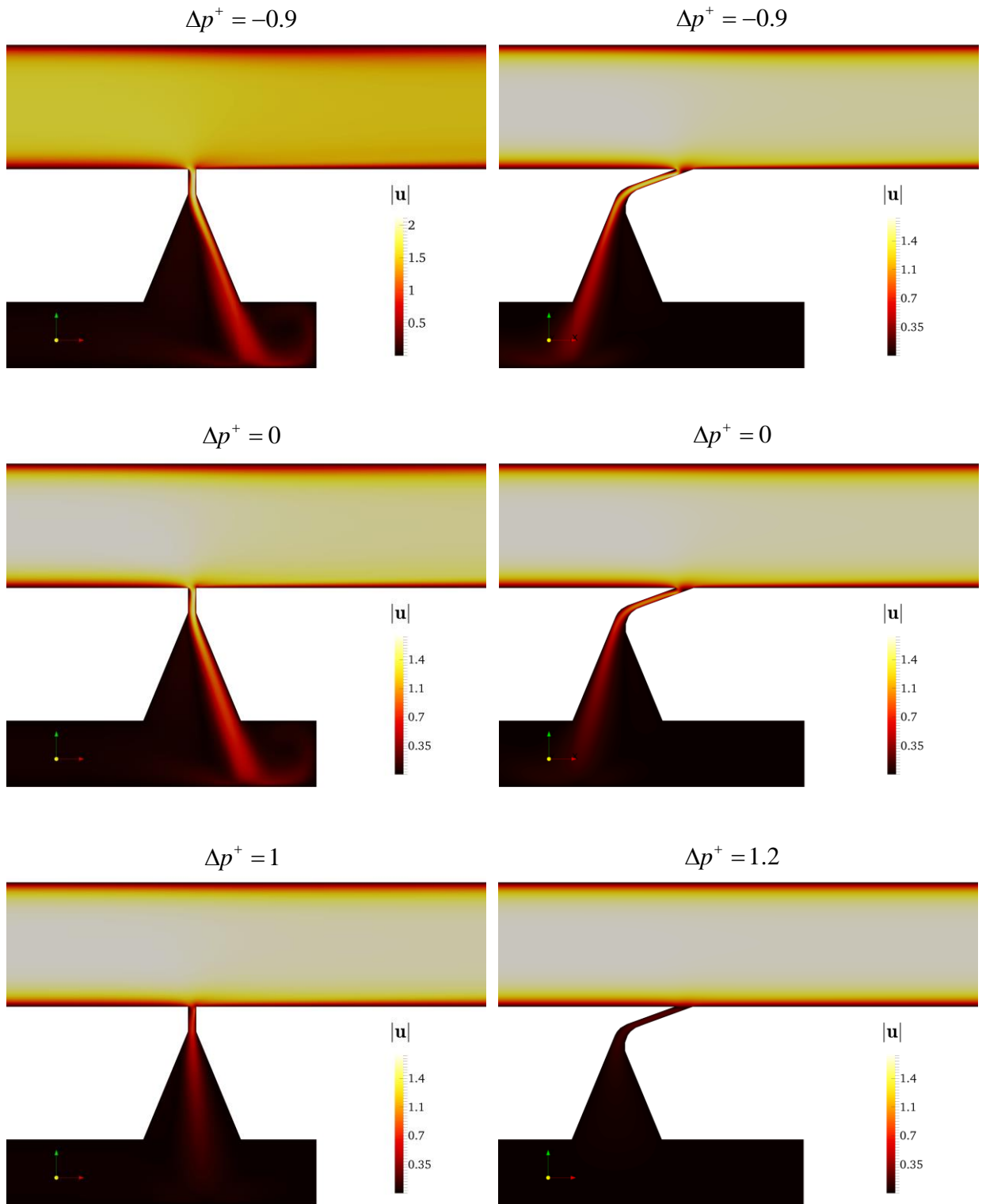


Fig. 4-2: Simulation results for the velocity field at  $Re = 500$ , for the  $90^\circ$  side channel geometry (left panel) and the  $20^\circ$  geometry (right panel). The pressure at the side channel increases from top to bottom.

The results for the velocity field are shown in Fig. 4-2 for pressure differences  $\Delta p^+$  ranging from -0.9 to 1 for the 90° geometry, and from -0.9 to 1.2 for the 20° geometry. For the 90° geometry, the liquid tends to flow along the right side of the widening until it enters the collector channel. In contrast, for the 20° geometry the liquid is faster near the left side of the widening. For the 20° geometry, this behavior is somehow obvious since the liquid is accelerated in the side channel direction and is thus pushed to the left side of the widening downstream.

The situation for the 90° geometry is different, because the fluid flow should only be directed perpendicular to the main channel. Thus, the alignment of the fluid near the right side of the widening might have its origin in the small vortex that is located at the upstream side at the side channel entry. This leads to a slightly compressed flow near the left side along the side channel.

The two images at the bottom of Fig. 4-2 represent very low flow fractions, since the pressure at the side channel is nearly equal to the pressure at the side channel entry. Hence, the velocities are very low compared to the other cases, leading to a centered flow along the widening at the 90° geometry.

Due to the alignment of the fluid along the widening, a big vortex can be observed in that area, as shown in Fig. 4-3. However, the velocity of the fluid flowing back into the widening is very low, so the energy loss is small. The angle of the widening is too aggressive. Thus, this angle should be reduced in future designs if it should act as a diffusor to recover energy when the velocity of the side channel fluid is slowed down.

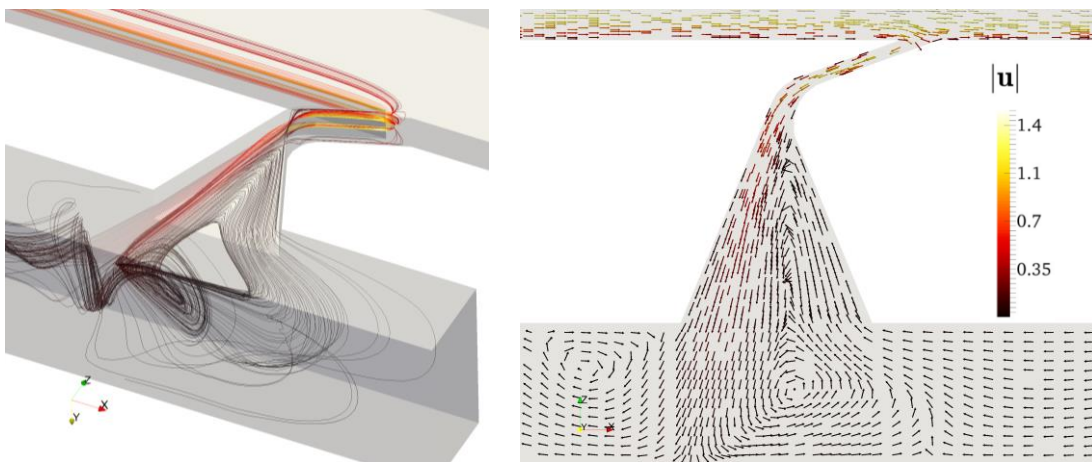


**Fig. 4-3: Streamlines for the 20° junction, illustrating the complex flow situation at the entry into the collector channel (left panel). Velocity field with vectors colored by the magnitude of the velocity at the center plane of the side channel (right panel).**

### 4.2.2 Pressure field

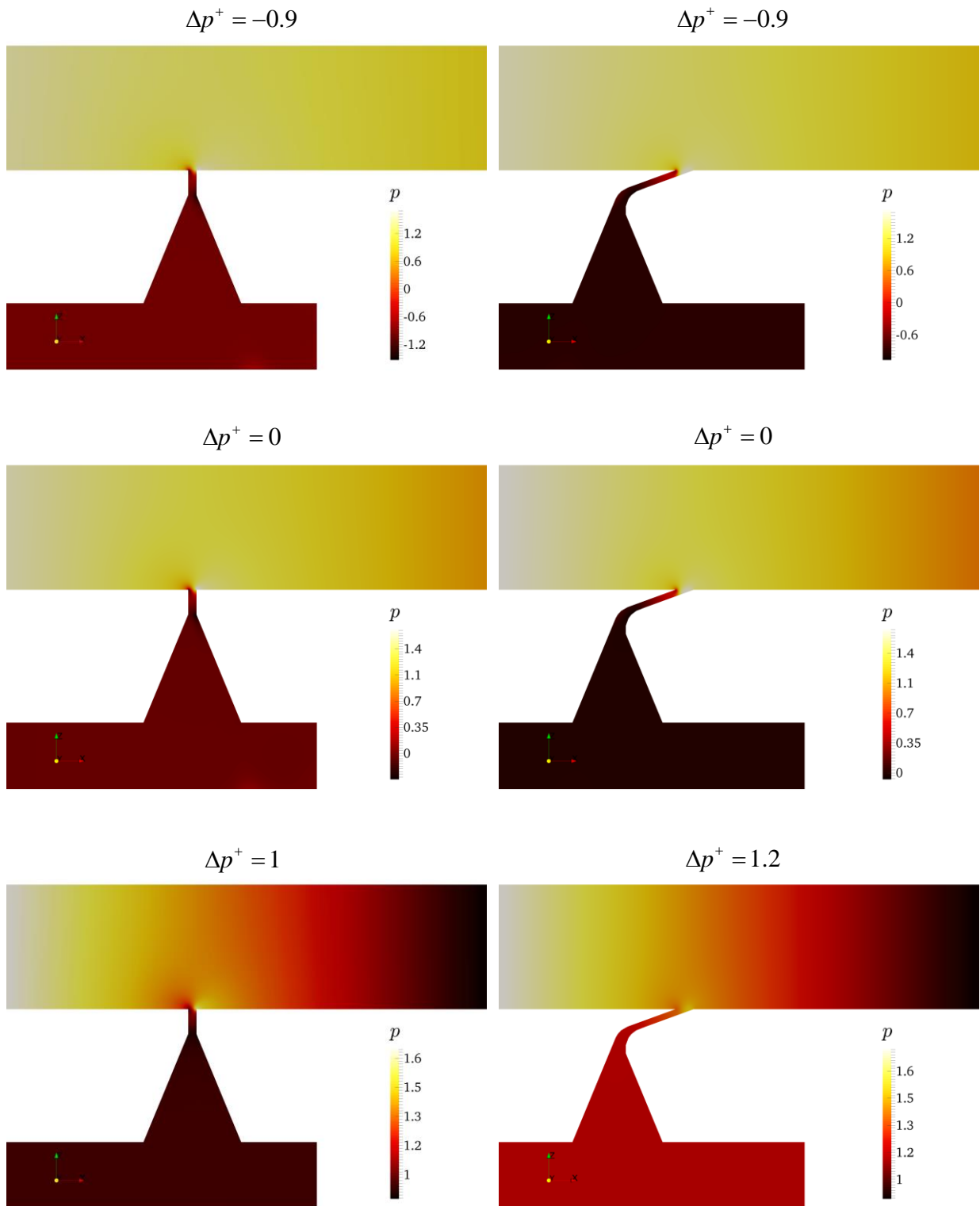


Fig. 4-4: Simulation results for the pressure field at  $Re = 500$ , for the 90° side channel geometry (left side) and the 20° geometry (right side). The pressure at the side channel increases from top to bottom.

The results for the pressure field nicely illustrate the pressure drop in the main channel, which is hence of some importance for the interpretation of the results. The pressure in the

side channels is very close to the pressure set up as boundary condition at the outlet face of the junction  $out_J$  (see Fig. 4-1). This means that the pressure drop in the collector channel, and further through the widening, is negligible. Only at higher flow fractions, i.e., for pressure differences of  $\Delta p^+$  ranging between -0.9 and 0, the pressure drop in the side channel becomes significant. This is not surprising, since the pressure drop increases with higher velocity, and thus with higher flow fraction.

The by far largest contribution to the pressure drop comes from the deflection of the flow directly at the side channel entry. Hence, the design of the side channel entry is of major importance for the pressure drop between main and side channel. It is known that the pressure drop in junctions can be reduced by replacing sharp edges with small roundings [35], which is recommended for future designs to keep the pressure drop low.

In summary, the overall pressure difference that is necessary to realize a proper flow fraction for separation (i.e., approximately 0.05) is low compared to a typical pressure drop in the main channel. The latter is determined by the distance that is required for the fibers to get in their final position, as well as the Reynolds number in the main channel.

## 5 Modeling of the pressure drop

To give an outlook on the suitability of the separation technique for industrial applications, the pressure drop of the device is of major importance, since the operating costs for hydrodynamic filtration consist mainly of electrical energy for pumping.

### 5.1 Relationship between flow fraction and pressure drop

Simulations were performed at different pressure differences  $\Delta p^+$ , and the corresponding values for the flow fractions were determined. The goal was then to derive a relationship between these two variables, which further allows the prediction of the pressure drop for a given flow fraction. In principle, the pressure drop is modeled with a Bernoulli equation from the main channel outlet  $out_C$  to the end of the widening at the side channel outlet  $out_J$ .

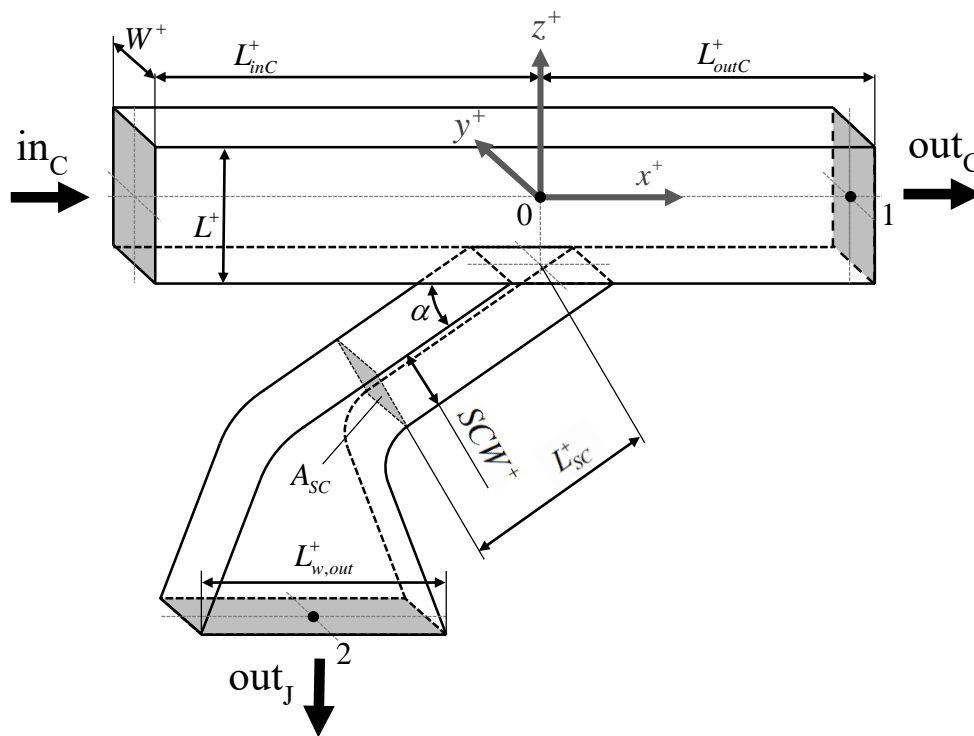


**Fig. 5-1.** Illustration of the 20° side channel geometry, including all variables used in the model for the pressure drop.

Since the velocity in the collector-channel is very low, the pressure drop in the collector-channel is negligible. For this reason, the outlet face  $out_J$  in the model is seen as the face at the end of the widening. The overall function for the pressure drop as a function of the flow fraction is:

$$\begin{aligned}
\Delta p^+ = & \left( \frac{\langle \bar{u}_{inC} \rangle}{\Phi^+ + 1} \right)^2 \frac{1}{2} \left( (\pi_J - \pi_C) (\Phi^+ + 1)^2 + 1 - \left( \Phi^+ \frac{A_{outC}}{A_{outJ}} \right)^2 \right. \\
& \left. - \left( \Phi^+ \frac{A_{outC}}{A_{SC}} \left( 1 - \frac{SCW^+}{L_{w,out}^+} \right) \right)^2 \zeta_{wid,SC} \right) \\
& + \zeta \mu^k \rho^{r-1} \left( \frac{\langle \bar{u}_{inC} \rangle}{\Phi^+ + 1} \right)^n \left( \frac{L_{outC}^+ (L^+ + W^+)^m}{(2L^+W^+)^m} - \frac{\left( \Phi^+ \frac{A_{outC}}{A_{SC}} \right)^n L_{SC}^+ (SCW^+ + W^+)^m \zeta_J}{(2SCW^+W^+)^m} \right)
\end{aligned} \tag{5-1}$$

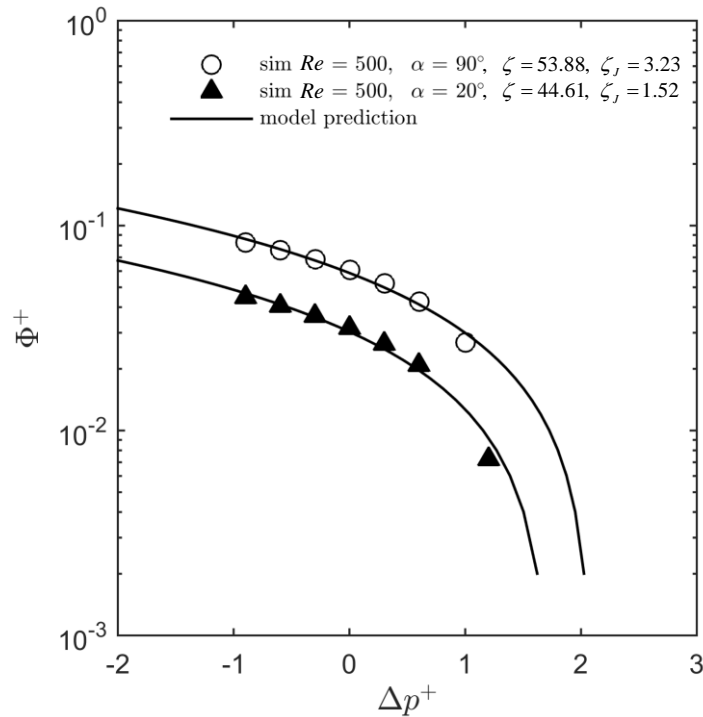
The derivation of this equation is given in Appendix E.4. It is based on the model in the work of König [34], and was adopted to take the more complex geometry into account. Besides geometrical parameters, inlet velocity and the flow fraction, the model includes the parameters  $\pi_J, \pi_C, \zeta, \zeta_J$  and  $\zeta_{wid,SC}$ . The factors  $\pi_J$  and  $\pi_C$  are used in the terms for the kinetic energy in the Bernoulli equations, and are set to 0 and 1, respectively. This is because the kinetic energy cannot be considered for the side channel flow due to its change in direction at the side channel entry. The friction factor  $\zeta$  describes the energy loss in the main channel, and the friction factor  $\zeta_J$  is the multiple of  $\zeta$  to determine the side channel loss (i.e.,  $\zeta_J$  provides information on how many times the frictional factor in the side channel is larger than in the main channel).  $\zeta_{wid,SC}$  is the frictional factor for the widening. In this model, only two parameters,  $\zeta$  and  $\zeta_J$ , have to be fitted. The parameters  $k, m, n$  and  $r$  are varying depending on the flow regime, and were chosen with 1,2,1 and 0 respectively in the calculations, since laminar flow is assumed at the given Reynolds numbers.

## 5.2 Results for pressure drop coefficients

The results from the simulations in OpenFOAM® were post processed with MATLAB, where two frictional coefficients were fitted. The results in Fig. 5-2 show that for values of  $\Delta p^+$  above 1, the flow fraction decreases very fast towards zero. Simulations with pressure differences of 1.5 for the 90° geometry and 1.8 for the 20° geometry did not give any meaningful results, indicating that above these values no liquid is removed through the side channel.

König [34] investigated the pressure drop at channels with a square cross section, using a model very similar to the one used in this work. She found values for  $\zeta$  in the range of 65

and for  $\zeta_J$  between 2.23 and 3.44, depending on the angle of the side channel. These previous results are not far off the values in the present work, with values of  $\zeta = 53.9$  and  $\zeta_J = 3.23$  for the  $90^\circ$  geometry, as well as  $\zeta = 44.6$  and  $\zeta_J = 1.52$  for the  $20^\circ$  geometry. However, the frictional coefficients for the main channel were not expected to differ that much between the different cases.



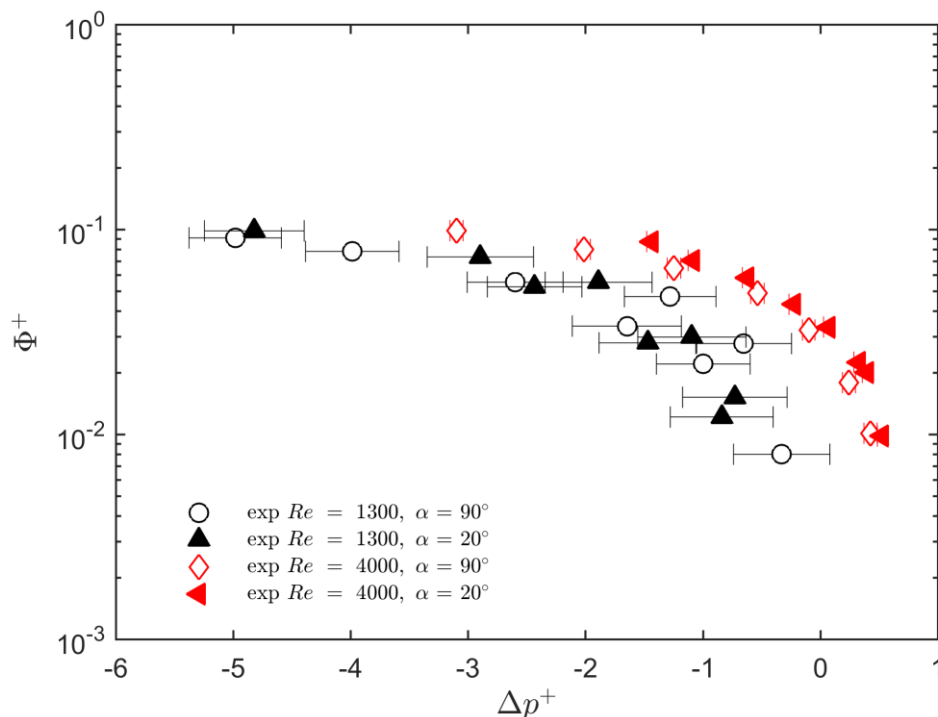
**Fig. 5-2: Results of the simulations (markers) and the model function for the determined frictional factors.**

Fig. 5-2 illustrates that the pressure difference needed to realize a certain flow fraction is higher for the  $20^\circ$  geometry (i.e.,  $\Delta p^+$  is smaller for a fixed  $\Phi^+$  compared to the  $90^\circ$  geometry). This is because of the fact that the side channel width is 0.75 mm (compared to 1 mm for the  $90^\circ$  geometry), and that the flow is simply more deflected for the  $20^\circ$  geometry.

The pressure drop in the system was also determined experimentally, using pure water without fibers. Unfortunately, experiments at  $Re = 500$  showed unsatisfying results, since the accuracy of the pressure measurement was not high enough to give reproducible results. Since the pressure is normalized with the inlet velocity, a measurement error of the same magnitude leads to higher deviations at lower inlet velocities, and thus lower Reynolds numbers.

Experiments at  $Re = 1,300$  and  $Re = 4,000$  showed better results, which are summarized in Fig. 5-3. Interestingly, no differences in the pressure drop characteristics between the two geometries are visible. The reason for this disagreement is most likely attributed to the large variation of the geometry for the  $20^\circ$  side channel as can be seen in Chapter 3.5.4. Clearly, the  $20^\circ$  side channel was much wider in the experiments as the  $0.75$  mm used in the simulations. Also, the purge channel was not considered in the simulations, which is unfortunately located at the most delicate position (i.e., where the highest pressure drop occurs).

Noticeably, the normalized pressure difference to reach a certain flow fraction is higher at the lower Reynolds number. Also, the associated error bars are much larger for  $Re = 1,300$  compared to  $Re = 4,000$  in the experimental data set. This hints to the fact that the data for  $Re = 1,300$  is not reliable, and extrapolation to smaller Reynolds numbers must be avoided. In summary, the overall shape of the curves based on our experimental and simulation data are similar. Also, a comparison of the data for the  $90^\circ$  side channel (although recorded at different Reynolds numbers) shows reasonable agreement, giving some confidence in both the experimental and simulation data.



**Fig. 5-3: Results for the flow fractions as a function of the pressure difference for both geometries at two different Reynolds numbers.**

## 6 Conclusions

### 6.1 Separation Efficiency

The results for the separation efficiency summarized in Chapter 3.5 show that the regime of the suspension flow in the main channel plays a key role for separation. Clearly, the flow regime is governed by the Reynolds number and the consistency. A network of fibers, located at the channel's center, can be observed at  $Re = 1,300$ , while at  $Re = 4,000$  the fibers are more evenly distributed across the main channel. We speculate that this is caused by the higher shear stress that is able to break-up the fiber network.

However, the strength of the fiber network depends strongly on the consistency, since a higher concentration of fibers leads to more contact points per fiber. Also, the region near the channel wall having a lower concentration of fibers, which is essential for hydrodynamic filtration, becomes narrower at higher consistencies. This is simply because of the larger number of fibers that have to fit in the channel.

In contrast, the design of the side channel has a smaller impact on the separation efficiency. However, this detail is of critical importance in terms of operational ease. Plugging leading to a shutdown of HDF operation was not observed when using the  $20^\circ$  geometry. This is in contrast to what other researchers reported in experimental devices that mimicked the flow conditions in a pressure screen. However, it has to be mentioned that this previous work focused on much higher Reynolds numbers compared to the present work [15][17][25].

When keeping the Reynolds number constant, changing the channel geometry has an impact on the separation, since the ratio of the fiber length to the channel dimensions changes. The size of the fiber network that is located in the channel center at lower Reynolds numbers remains more or less constant, while at decreasing channel dimensions the distance of this network to the channel wall becomes smaller.

By keeping the flow fraction low, the passage of longer fibers through the side channel can be prevented. To lower the number of side channels needed to reach a certain overall separation efficiency, the flow fraction should be as large as possible without removing long fibers from the main channel. At lower Reynolds numbers, this value is higher

because the region having a low concentration of longer fibers near the wall is larger in that case. Thus, lower Reynolds numbers will result in a smaller number of side channels.

## **6.2 Pressure drop**

The pressure drop was determined by simulations and experiments for the fluid phase only. Simulations suggested that the design of the side channel entry is crucial for the pressure drop, since the by far largest contribution to the pressure drop along the side channel is present in this region. However, the pressure differences required to realize flow fractions in the range of 0.015 to 0.05 are rather low in the side channel. Consequently, future optimization studies with respect to the energy demand should primarily consider the pressure drop in the main channel, i.e., its length.

The correlation between the simulation results and experiments is promising in terms of qualitative behavior. However, the absolute values differ significantly. In the experiments the pressure differences were higher than those predicted by the simulations. This can be partially explained by the non-ideality of the real system: the surface roughness, as well as the dimensional inaccuracy of the side channel geometry due to swelling of the 3D-printed parts might have influenced the results for the pressure drop. Furthermore, the design of the pressure measurement was not ideal for measuring pressure differences of only a few Pascal.

## **6.3 Projections for operating costs**

To provide an outlook on the operation costs for a large-scale hydrodynamic filtration device, the total power draw of a device has been estimated and is shown in Table 6-1 and Table 6-2. The total power draw consists of 3 contributions: the power draw for (i) the pump for the main channel flow (ii), the pump for the side channel flow and (iii) the pump which provides regular purging of the side channels.

The calculation is kept very simple and is detailed in Appendix E.6. However, the total power draw for a total inlet flow rate  $\dot{m}_{inC,tot,susp} = 100,000$  kg/h is only 131 W and 1,293 W for 10 and 100 side channels per main channel, respectively (see Table 6-2). The power draw for the distributor that splits the flow in order to provide the same flow rate in each main channel is not included here. However, the energy demand for the part of the operation that is decisive for the separation is rather low compared to established

separation techniques, since the Reynolds number in the channels, we assumed  $Re = 4,000$ , and thus the pressure drop is very low. In this example, 10 and 100 side channels are aligned along each main channel. For the given Reynolds number and flow fraction, this leads to a removal of approximately 8% and 55% of the fines fraction (see Fig. 6-1). Noticeably, the relationship between the number of side channels and the total power draw is linear.

The results for the power draw estimate show that the power draw of the main channel pump and the purge pump are of the same order of magnitude, while the energy required for the side channel pump is significantly smaller. From an economic point of view, the dimensions of the main channel should be as large as possible to reach the desired separation efficiency. Additionally, the pressure and the flow rate for the purging of the side channel should be chosen as small as possible to guarantee a satisfactory operation. Based on the observations that have been made during the experiments, we assume that a pressure difference of 1.5 bar is sufficient. Since the pressure and amount of purging plays an important role for the overall energy consumption, it needs to be considered in future studies.

**Table 6-1: Process parameters for the estimate of the power draw of a HDF with a throughput of 100,000 kg/h suspension.**

parameter	symbol	value	unit
total throughput	$\dot{m}_{inC,tot,susp}$	100,000	kg/h
inlet consistency	$C_{inC}$	0.1	%
finest fraction inlet	$dQ_{3,finest,inC}$	0.14	-
Reynolds number	$Re$	4,000	-
channel dimensions	$W \times L$	3 x 15	mm
flow fraction	$\Phi^+$	0.015	-
purge flow rate	$\dot{V}_{purge}$	1.67	ml/min <sup>1</sup>
purge pressure	$\Delta p_{purge}$	1.5 <sup>2</sup>	bar
pump efficiency	$\epsilon_{Pump}$	70	%
number of main channels	$n_C$	772	-
energy price	$K_{energy}$	35	€/MWh

**Table 6-2: Results for the power draw of a HDF with a throughput of 100,000 kg/h suspension, with 10 and 100 side channels per main channel.**

parameter	symbol	value	value	unit
side channels per main channel	$n$	10	100	-
main channel length	$L_C$	2	20	m
separated fines fraction	$(1-T_{fines})$	8	55	%
mass flow of separated fines	$\dot{m}_{fines,SC}$	1.12	7.7	kg/h
power draw pump main channel	$P_{PumpC,tot}$	81.3	812.7	W
power draw pump side channel	$P_{PumpSC,tot}$	3.5	19.7	W
power draw pump purge channel	$P_{Purge,tot}$	46.0	460.2	W
<b>total power draw</b>	<b><math>P_{Pump,tot}</math></b>	<b>130.8</b>	<b>1,292.6</b>	<b>W</b>
<b>total operating costs</b>	<b><math>K_{HDF,tot}</math></b>	<b>0.0046</b>	<b>0.045</b>	<b>€/h</b>
<b>costs per ton separated fines</b>	<b><math>K_{fines}</math></b>	<b>4.1</b>	<b>5.9</b>	<b>€/t</b>

<sup>1</sup> Based on experiments that indicated that purging with 5 ml/min is sufficient for 3 side channels.

<sup>2</sup> This is the expected purge pressure based on 1 bar total pressure loss, and 50% safety margin for purging.

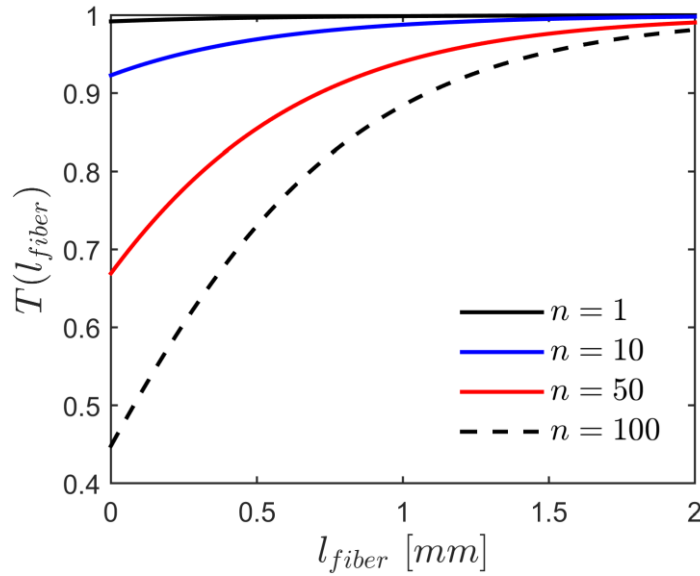


Fig. 6-1: Separation efficiency at  $Re = 4,000$  and  $\Phi^+ = 0.015$  after 1, 10, 50 and 100 side channels.

## 6.4 Outlook

We looked at the separation efficiency at one single side channel, and experimentally observed a promising separation performance. Hydrodynamic filtration has the potential to be a serious competitor to well established technologies due to its low energy consumption. However there are still a number of obstacles to cross before HDF technology can be applied on a pilot, or even industrial scale.

During the preliminary experiments, it became clear that in order to use multiple side channels along the main channel, each of these has to be designed with a different width to guarantee equal flow rates and thus flow fractions. Another option would be to set the pressure at each side channel independently. This must be investigated in future work, since it is of crucial importance for the final application of HDF technology.

The number of side channels along the main channel is limited, because thickening of the suspension takes place and thus the suspension would become immobile at some point. This would require the addition of water to lower the consistency again. A pilot-scale HDF could have the basic design of a shell and tube heat exchanger, with a set of parallel main channels that have, e.g., 10 side channels each. The mechanical design of such a pilot-scale HDF is a rather formidable task, and hence this endeavor must be followed in a separate project.

With the further increasing level of detail considered in simulations of fiber suspension flow, phenomena like the network formation of fibers and its impact on the separation performance should be investigated. This would also allow us to take a look at the separation of different pulps, since the fiber distribution clearly determines the size of fibre networks, i.e., flocks, in the channel.

## 7 Experimental

### 7.1 *Pre-treatment of the pulp*

The pulp provided by the industry partners had a consistency between 5 and 20%, while at experiments the highest consistency used was 0.75%. For every set of experiments, a total mass of 17 to 20 kg of pulp was prepared. When lowering the consistency, it is necessary to apply shear forces on the fibers to unbind them from the network, which was done by disintegration for 20 minutes. The disintegrator has only a volume of 2 l, so the mass of fibers for the experiments was first diluted with deionized water to this volume, and further diluted after the disintegration.

### 7.2 *Determination of the mass flow rates*

The mass flow rates were measured by weighting the fluid that left the main channel and the side channel in a certain time. The measurements were done three times at the beginning of each set of experiments and averaged. Since the calculation of the grade efficiency is based on the mass flow rate at the main channel inlet, the flow rate at the inlet was calculated by simply adding the side channel flow rate to the flow rate at the main channel exit.

The maximum deviation of the mass flow rate during operation was within  $\pm 4\%$  at  $Re = 4,000$  and  $\pm 6\%$  at  $Re = 1,300$ .

### 7.3 *Sampling*

For each set of operation parameters that were tested, 3 samples were taken. Each of this samples consisted of 2 samples with 200 ml at the inlet and side channel for the measurement of the fiber distribution and another 2 for the consistency measurement with 350 ml. The samples were stored in a refrigerator to avoid any further reactions that could lead to degradation of the pulp.

In order to take samples of the pulp entering the HDF at the inlet, the side channel pump was turned off for 30 seconds, and the sample was taken at the exit of the main channel.

## 7.4 Measuring the consistency

The consistencies were determined by thermogravimetric analysis. Filter papers from *Macherey Nagel*, type MN 615, with an average retention capacity of 4-12  $\mu\text{m}$  were used [36]. The filter papers were predried in an oven at 105  $^{\circ}\text{C}$  for 15 minutes. After measuring the weight of the filter paper and the sample, the suspension was dewatered via a suction filter and further dried at sheet dryers for 10 minutes. The weight of the filter, now with fibers, was then measured again after 3 hours in the oven.

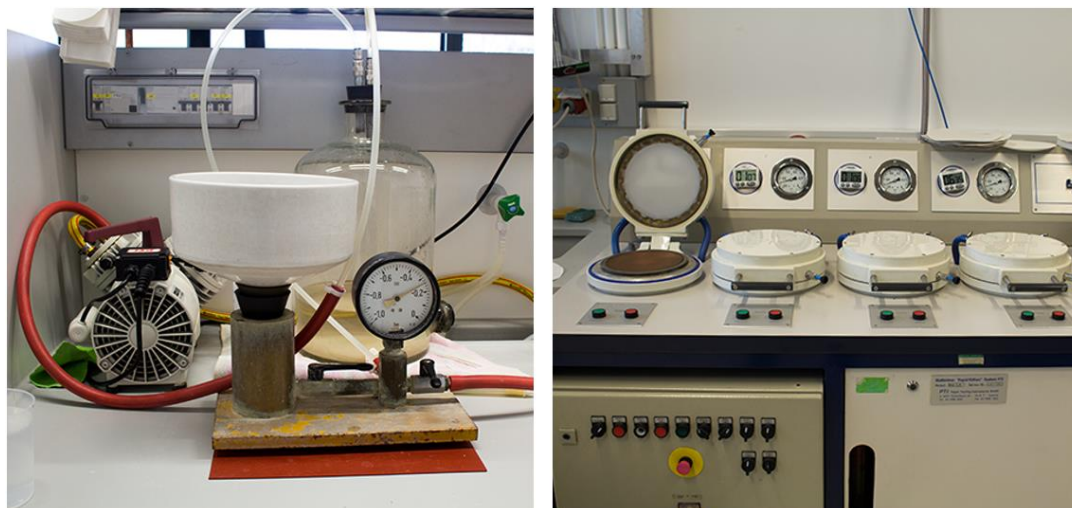


Fig. 7-1: Suction filter with vacuum pump (left panel) and sheet dryer (right panel) as used for the determination of the consistencies.

## 7.5 Measuring the fiber distribution

The fiber distributions were measured with a fiber tester from *Lorentzen & Wettre*, type *L&W FIBER TESTER PLUS*, as shown in Fig. 7-2. The whole suspension is sucked in at the inlet nozzle at the beginning of the measurement, and is diluted with water inside the measurement device. Fibers are pumped through a very small gap, where images of the individual fibers are taken. These images are then processed with a software to obtain, e.g., the length of the stretched fibers and the mean thickness, which are used to calculate the volume based  $q_3$  distribution of a sample. Usually, a total number of 8,000 fibers longer than 200  $\mu\text{m}$  should be analyzed in order to get reliable values for the fiber distribution. However, in our experiments the number of fibers in the fines fraction was very low, and so these measurements were stopped after 20 to 30 minutes. Otherwise, only the same fibers would have been analyzed again, since the suspension in the measurement device is pumped in a closed loop.

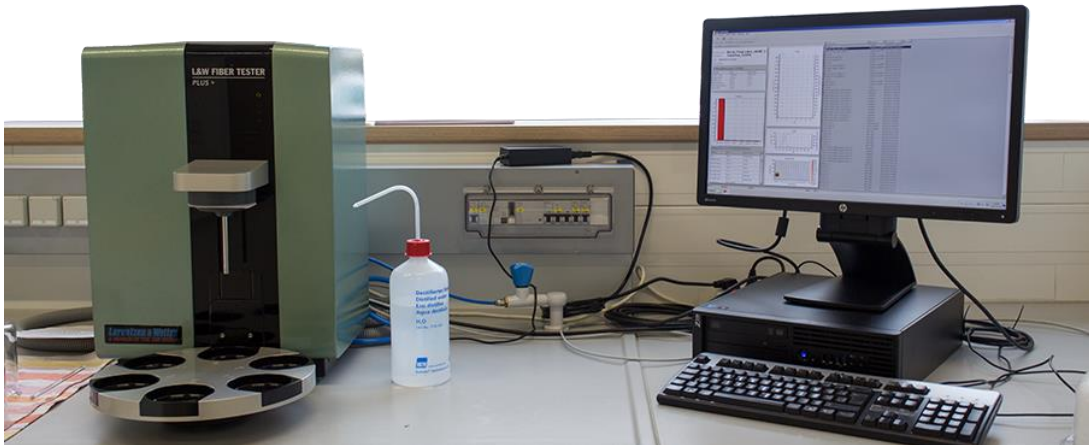


Fig. 7-2: L&W FIBER TESTER PLUS with the PC for the data analysis at the IPZ.

## 7.6 Pressure measurement

T-junctions were installed at the main channel inlet and outlet, and at the side channel outlet, as can be seen in Fig. 3-2. The T-junctions are connected to hoses which lead to the pressure gauge.

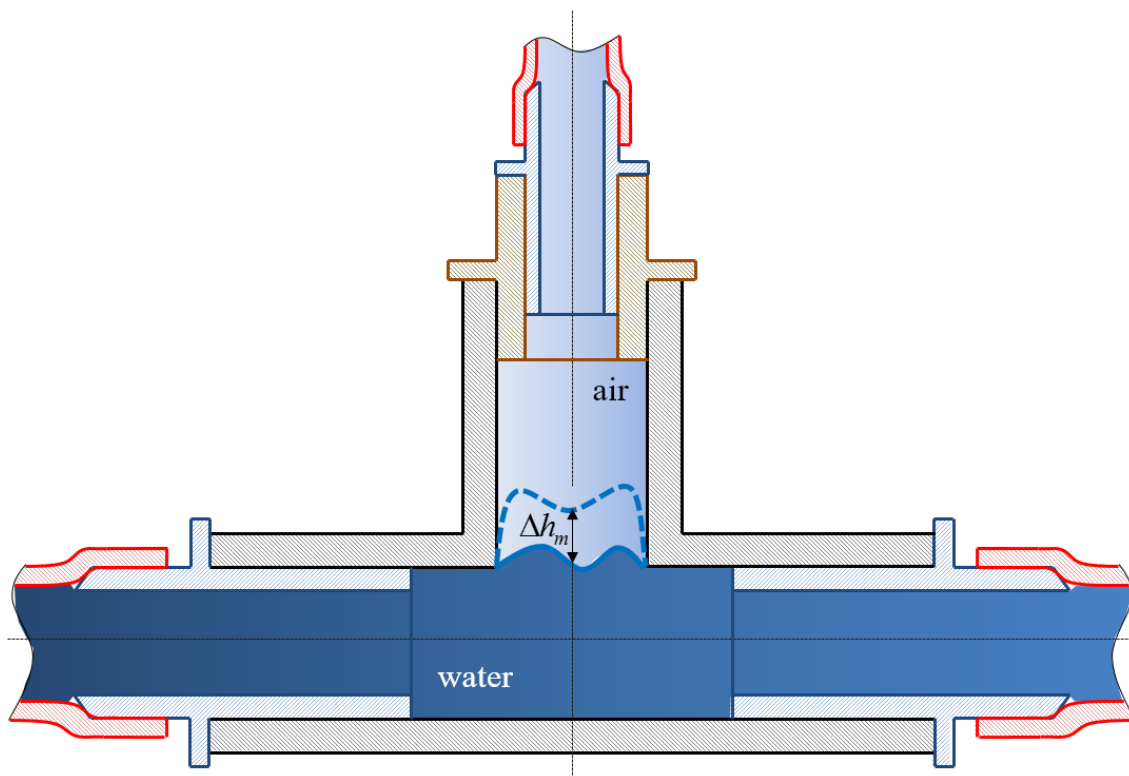


Fig. 7-3: T-junction for pressure measurement. In case the initial pressure in the measuring line is too low, the interfacial area is shifted upwards as shown by the dashed line, and further the measured pressure is lowered by  $\rho_{water} g \Delta h_m$ . Here, the pressure of the hydrostatic height of air is neglected, since the density of air is much lower than the density of water.

Each of the three measuring lines is separated from the gauge via a small valve (see P&ID in Appendix B.3), so the pressure can only be measured for one measuring point at a time, since only one pressure gauge is available. The measuring lines are filled with air, and flushed by opening the valve to the compressed air supply. This needs to be done to guarantee that the measuring line is totally filled with air, so that the pressure in the measuring system is equal to the pressure in the T-junction, as shown in Fig. 7-3.

This part is the most critical in the pressure measurement, since a variation of only 5 mm in height leads to a measurement error of approximately 50 Pa. We speculate, that air bubbles adhere to the edges in the junction, leading to errors in the range of  $\pm 30$  Pa, which further led to the relatively high standard deviations in Fig. 5-3. Thus, a redesign of the pressure measurement is highly recommended to reduce the errors at the pressure measurements.

We used a pressure gauge from *Fluke*, type *700G02*. At each measurement, 30 values were taken with a rate of 1 per second. The data was stored on the gauge, and later processed in MATLAB® after data transfer to PC.

## 8 References

- [1] T. Timmel, “Flippr<sup>o</sup>- Future Lignin and Pulp Processing Research,” 2015. [Online]. Available: <http://www.flippr.at/jart/prj3/flippr/main.jart>. [Accessed: 05-Aug-2015].
- [2] M. Mayr, R. Eckhart, I. Summerskiy, A. Potthast, T. Rosenau, J.-P. Schöggel, A. Posch, and T. Timmel, “Flippr<sup>o</sup>-an industrial research project in Austria,” *TAPPI J.*, vol. 14, no. 3, pp. 209–212, 2015.
- [3] B. Krogerus, L. Eriksson, A. Sundberg, J. Mosbye, I. Östlund, L. Sjöström, and A. Ahlroth, “Fines in closed circuits - Final report,” *KCL*, 2002. [Online]. Available: [https://www.researchgate.net/publication/238660713\\_Fines\\_in\\_closed\\_circuits\\_-\\_Final\\_report](https://www.researchgate.net/publication/238660713_Fines_in_closed_circuits_-_Final_report). [Accessed: 01-Aug-2015].
- [4] T. Taipale, M. Österberg, A. Nykänen, J. Ruokolainen, and J. Laine, “Effect of microfibrillated cellulose and fines on the drainage of kraft pulp suspension and paper strength,” *Cellulose*, vol. 17, no. 5, pp. 1005–1020, 2010.
- [5] H. M. Gruber, “Evaluation of fines content in pulps and filtrates in pulp production lines,” Graz University of Technology, 2014.
- [6] H. Lindqvist, K. Salminen, J. Kataja-aho, E. Retulainen, P. Fardim, and A. Sundberg, “The effect of fibre properties, fines content and surfactant addition on dewatering, wet and dry web properties,” *Nord. Pulp Pap. Res. J.*, vol. 27, pp. 104–111, 2012.
- [7] T. Lin, X. Yin, E. Retulainen, and M. M. Nazhad, “Effect of Chemical Pulp Fines on Filler Retention and Paper Properties,” *Appita*, vol. 60, no. 6, p. 469, 2007.
- [8] J. König, “Design and Feasibility Study of a lab-scale Device for the Separation of Fines with Hydrodynamic Filtration,” Graz University of Technology, 2015.
- [9] M. Yamada and M. Seki, “Hydrodynamic filtration for on-chip particle concentration and classification utilizing microfluidics,” *Lab Chip*, vol. 5, no. 11, pp. 1233–1239, 2005.
- [10] A. Lenshof and T. Laurell, “Continuous separation of cells and particles in microfluidic systems,” *Chem. Soc. Rev.*, vol. 39, no. 3, pp. 1203–1217, 2010.
- [11] D. Di Carlo, “Inertial microfluidics,” *Lab Chip*, vol. 9, no. 21, p. 3038, 2009.
- [12] D. Di Carlo, J. F. Edd, K. J. Humphry, H. a. Stone, and M. Toner, “Particle segregation and dynamics in confined flows,” *Phys. Rev. Lett.*, vol. 102, no. 9, pp. 1–4, 2009.
- [13] A. Tamura, S. Sugaya, M. Yamada, and M. Seki, “Tilted-Branch Hydrodynamic Filtration for Length-Dependent Sorting of Rod-Like Particles,” in *15th International Conference on Miniaturized Systems for Chemistry and Life Sciences*, 2011, pp. 1343–1345.
- [14] S. Sugaya, M. Yamada, and M. Seki, “Observation of nonspherical particle behaviors for continuous shape-based separation using hydrodynamic filtration,” *Biomicrofluidics*, vol. 5, no. 2, 2011.
- [15] J. A. Olson, “The Effect of Fibre Length on Passage Through Narrow Apertures,”

- University of British Columbia, 1996.
- [16] A. Kumar, "Passage of Fibres Through Screen Apertures," University of British Columbia, 1991.
- [17] R. W. Gooding, "Flow Resistance of Screen Plate Apertures," University of British Columbia, 1996.
- [18] S. Dong, "Modeling of Fiber Motion in Pulp and Paper Equipment," University of British Columbia, 2002.
- [19] S. Dong, M. Salcudean, and I. Gartshore, "The effect of slot shape on the performance of a pressure screen," *TAPPI J.*, vol. 3, no. 5, pp. 3–7, 2004.
- [20] S. Mokamati, "Effect of Aperture Geometry on the Steady Flow Through the Narrow Apertures in a Pulp Screen: Numerical and Experimental Study," University of British Columbia, 2007.
- [21] "Andritz RotoWash." [Online]. Available: <https://www.andritz.com/pp-paper-machine-approach-fiberrecovery-rotowash.pdf>. [Accessed: 15-Apr-2016].
- [22] "Andritz SpeedWasher." [Online]. Available: <https://www.andritz.com/pp-pulprecycled-ashwashing-speedwasher.pdf>.
- [23] J. A. Olson and T. Rehmat, "A lecture on cleaning and hydrocyclones in the pulp and paper industry," 2001. [Online]. Available: <http://www.fibrelab.ubc.ca/files/2013/01/Topic-6-Mechanical-Pulping-Cleaning-text.pdf>.
- [24] T. Femmer, I. Flack, and M. Wessling, "Additive Manufacturing in Fluid Process Engineering," *Chemie Ing. Tech.*, vol. 88, no. 00, pp. 1–19, 2016.
- [25] M. Walmsley and M. Atkins, "Comparing fibre length fractionation of a laboratory flow channel to an industrial pressure screen," in *APPITA Annual General Conference*, 2003, pp. 369 – 376.
- [26] K. Siebertz, D. Van Bebber, and T. Hochkirchen, *Statistische Versuchsplanung*, vol. 43, no. 1974. Springer Berlin Heidelberg, 2010.
- [27] M. Stieß, *Mechanische Verfahrenstechnik - Partikeltechnologie 1*. Springer Berlin Heidelberg, 2009.
- [28] J. H. Spurk and N. Aksel, *Strömungslehre: Einführung in die Theorie der Strömungen*, 8th ed. Springer Berlin Heidelberg, 2010.
- [29] R. C. Vaseleski and a B. Metzner, "Drag Reduction in the Turbulent Flow of Fiber Suspensions," *AIChE J.*, vol. 20, no. 2, pp. 301–306, 1974.
- [30] M. J. Ajersch, "Mechanisms of Pulp Loss in Flotation DeInking," McMaster University, 1997.
- [31] P. J. Krochak, J. A. Olson, and D. M. Martinez, "Near-Wall Estimates of the Concentration and Orientation Distribution of Semi-Dilute Rigid Fiber Suspensions in Poiseuille Flow," in *14th Fundamental Research Symposium*, 2009, pp. 181–206.
- [32] "MatPIV - University of Oslo." [Online]. Available: <https://www.mn.uio.no/math/english/people/aca/jks/matpiv/>. [Accessed: 02-Feb-2016].
- [33] S. Radl, S. Karner, D. Treffer, and P. Feenstra, *Labor Partikelverfahrenstechnik II*.

- Graz University of Technology, 2013.
- [34] L. M. König, "Particle Separation in a Virtual Microfluidic Channel Graz University of Technology," Graz University of Technology, 2015.
- [35] *VDI-WÄRMEATLAS*, 10th ed. Springer, Verein Deutscher Ingenieure, VDI-Gesellschaft Verfahrenstechnik und Chemieingenieurwesen (GVC).
- [36] "Macherey Nagel Filter Paper MN 615." [Online]. Available: [ftp://ftp.mn-net.com/filtration/filter\\_paper\\_data\\_sheets/MN-615-Pd.pdf](ftp://ftp.mn-net.com/filtration/filter_paper_data_sheets/MN-615-Pd.pdf). [Accessed: 02-Feb-2016].
- [37] "OpenFoam Webpage." [Online]. Available: <http://www.openfoam.org/>. [Accessed: 01-Nov-2015].
- [38] A. Tamayol and M. Bahrami, "Laminar Flow in Microchannels With Noncircular Cross Section," *J. Fluids Eng.*, vol. 132, no. 11, p. 111201, 2010.
- [39] L. Papula, *Mathematik fuer Ingenieure und Naturwissenschaftler Band 3*. Wiesbaden: Vieweg + Teubner, 2011.

## Appendix A Preliminary Experiments

### A.1 Experiments with three open side channels

In the very first set of experiments, two different Reynolds numbers and two different flow fractions were tested, with pulp from *SAPPI Gratkorn*. At the first 4 parameter sets shown in Fig. A-1, the flow rate in the main channel was controlled via a peristaltic pump, while at the other 2 the flow was driven by hydrostatic pressure. In all cases, the flow rate at the side channel was adjusted with the height of the side channel hose exit, and thus the hydrostatic pressure. Especially at the lower flow fraction the flow rate at the first side channel was higher than at the following side channels, due to the decreasing pressure in the main channel, as described in chapter 3.3.5. The flow fractions in all figures of the preliminary experiments with more than 1 open side channel are calculated by the relationship given in Appendix E.1, since only the total flow rate at the side channel was measured.

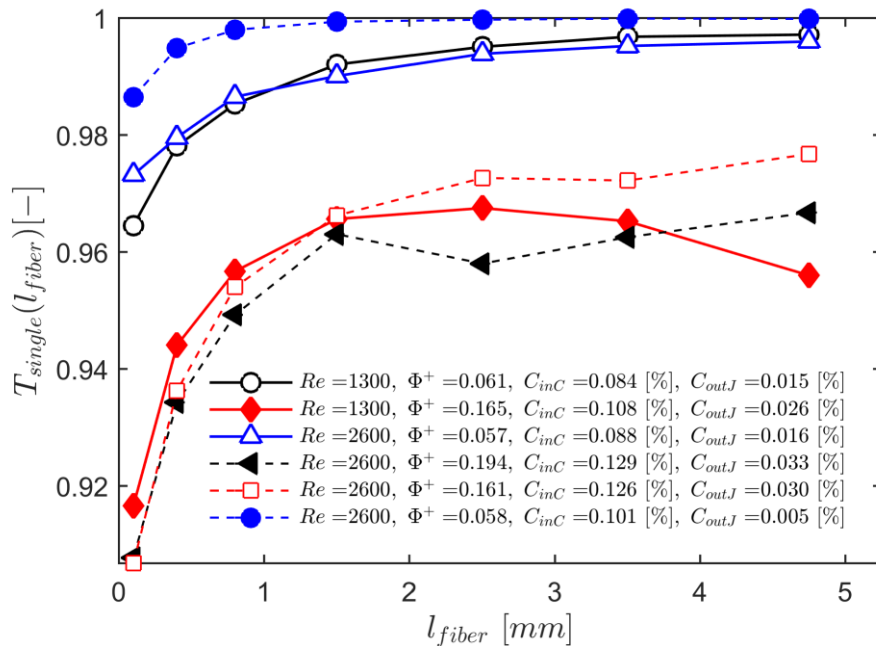


**Fig. A-1: First set of experiments, with two different operation modes. The flow rate in the main channel at the first 4 experiments was controlled via a peristaltic pump. The channel dimensions were 3 x 15 mm at the 90° side channel geometry.**

The results suggest that because of the strong pulsations in the main channel, more fibers are separated when operating with the peristaltic pump. Interestingly, the strong impact of the Reynolds number was not observed at these experiments, however, the difference in the Reynolds numbers is lower than in the experiments described in the main section of the

thesis. The results for pure hydrostatic driven flows at  $Re = 1,300$  are not shown here, because the inlet consistency was only 0.03% in that cases, due to a non-optimum setup of the stirred storage tank. Note that at these experiments, only one sample was taken, and thus no error bars could be plotted.

In a next step, the same parameter set was applied on mechanical pulp from *Norske Skog Bruck*. The tendency for plugging was higher, and the difference between the two operation modes seems lower. However, the separation efficiency curves in Fig. A-2 show a very poor separation behavior.

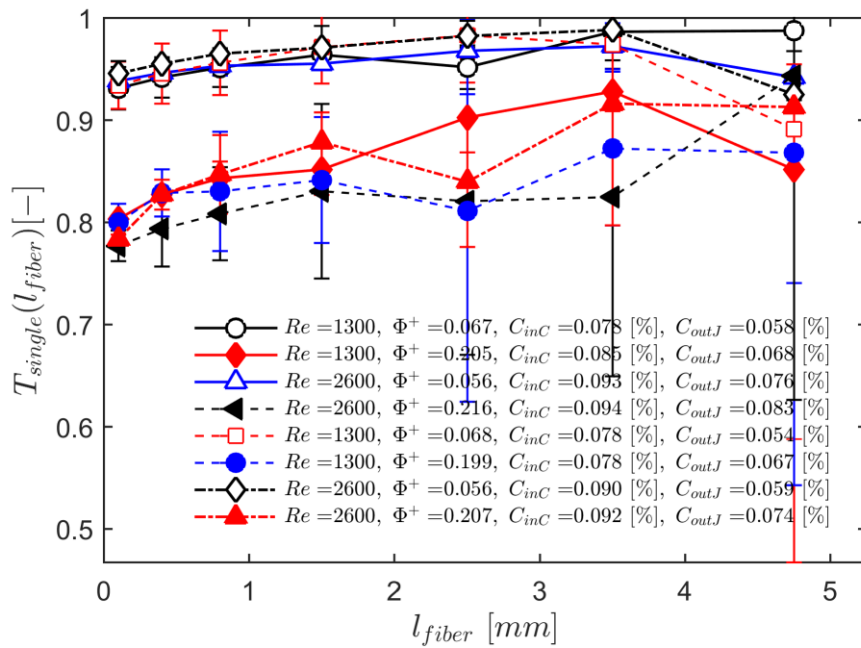


**Fig. A-2: Results for the preliminary experiments using mechanical pulp from *Norske Skog Bruck*, at channel dimensions of 3 x 15 mm at the 90° geometry.**

The fraction of removed fibers is nearly independent from the fiber length. The standard deviations as shown by the error bars are very high at fiber lengths above 3 mm, simply because only very few fibers are longer than 2.5 mm in this type of pulp. Based on these results, it was decided not to use mechanical pulp for further investigations on hydrodynamic filtration.

The last set of preliminary experiments was performed at higher consistencies, in order to determine the highest possible consistency at which hydrodynamic filtration could be used at channel dimension of 3 x 15 mm. Here, the 20° geometry was used for the first time. After the first two experiments at  $Re = 2,600$ , at which the main channel flow rate was controlled via the peristaltic pump, it was decided not to use this operation mode for

upcoming experiments, because plugging took place at the side channel when lowering the Reynolds number. The consistency in the stirred storage tank was set to 0.5%, however, the measured consistency at the main channel inlet was significantly lower. We speculate that the position of the stirrer in the tank was too centered, which led to a vortex and further to separation inside the tank towards the exit nozzle. The position of the stirrer as well as its geometry was changed for the subsequent experiments.

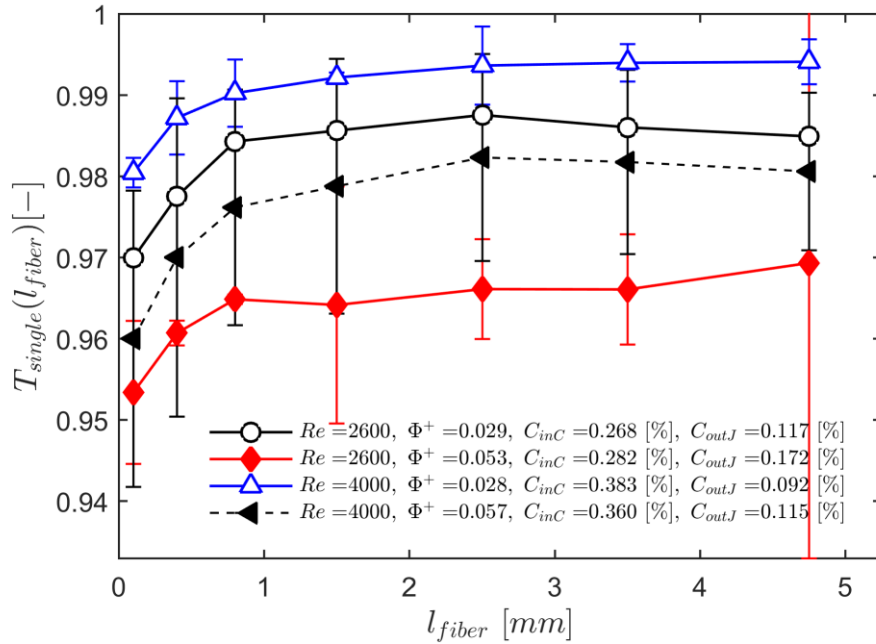


Fig. A-3: Separation efficiencies for channel dimensions of 3 x 15 mm at the 20° geometry.

Experiments showed that at these channel dimensions, the inlet consistency could be as high as 0.5%, above that value plugging of the main channel took place.

A purge mechanism was installed, which allows freeing the channel from deposited fibers. The purge line is connected to the water supply (approx. 6 bar pressure), and separated from the device by a solenoid valve. The solenoid valve is connected to a time relays, at which the impulse time and the pause time could be adjusted. The lowest possible impulse time of 0.05 s was used in most cases, the measured flow rates depending on the pause time are shown in Fig. A-5.

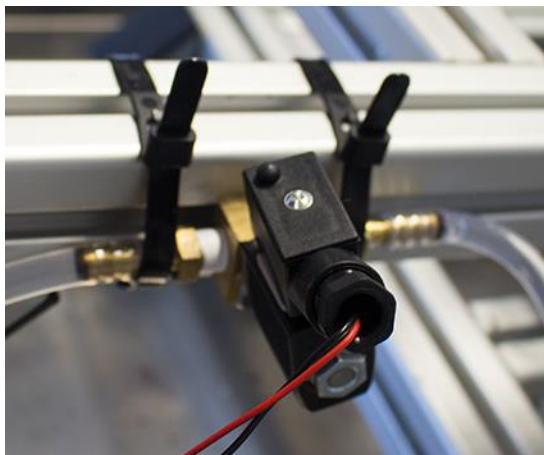


Fig. A-4: Solenoid valve *Bürkert 134071*, as used for controlling the purge flow rate.

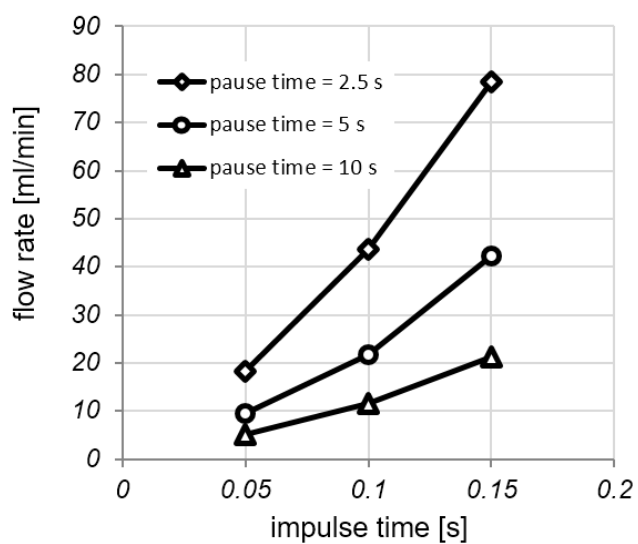


Fig. A-5: Flow rates through the solenoid valve as a function of the pause time and impulse time, which are adjusted with the time relays *ABB CT-TGS*.

# Appendix B P&ID's for the Hydrodynamic Filtration Device

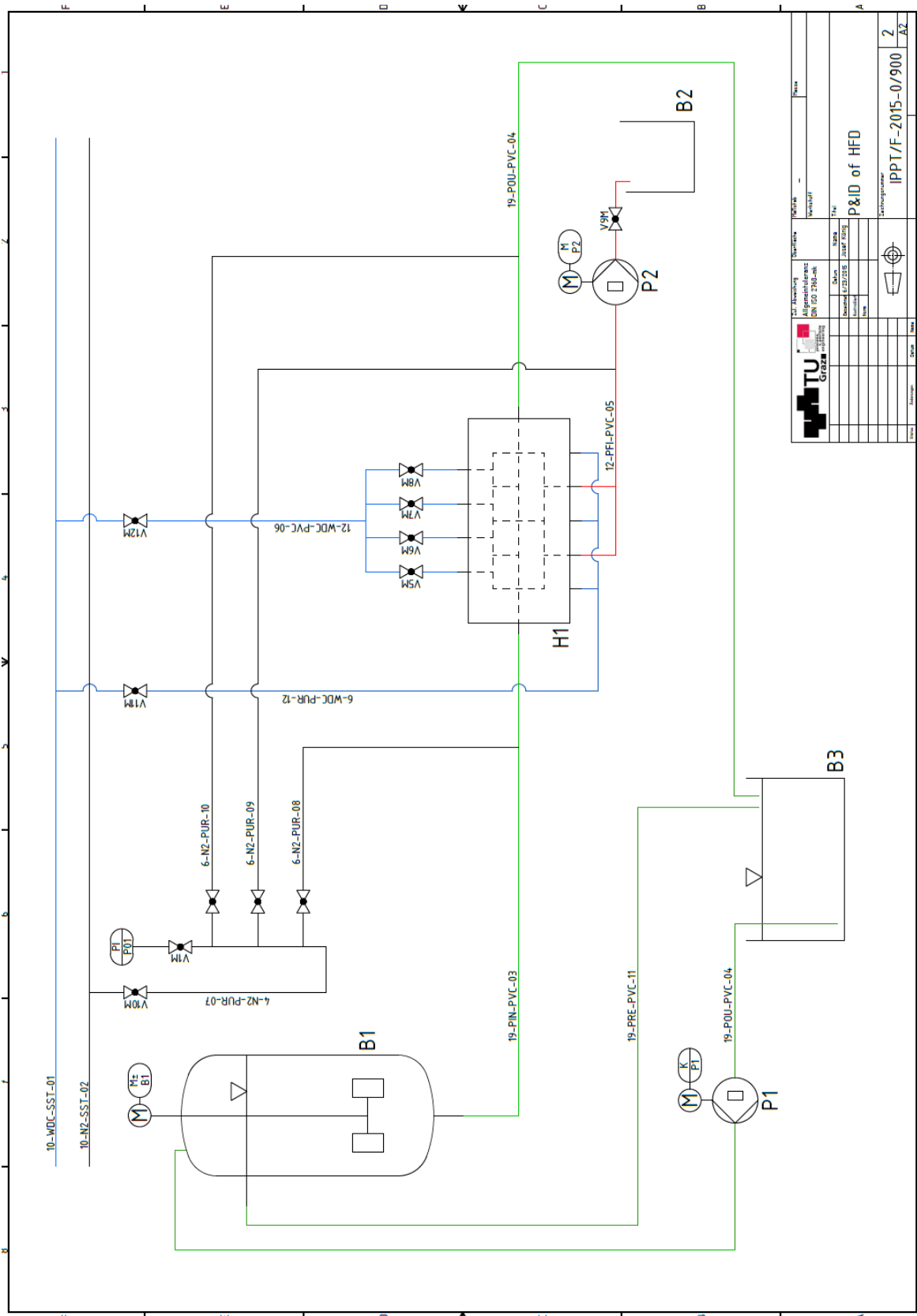
## B.1 Equipment list for P&ID's

Table B-1: List of the equipment as detailed in the P&amp;ID's.

Medium List																																																																	
Code	Medium	Colour																																																															
WDC	Water Deionized	blue																																																															
N2	Nitrogen	black																																																															
PIN	Pulp Suspension, Inlet	green																																																															
POU	Pulp Suspension, Outlet	green																																																															
PFI	Pulp Suspension, Fines	green																																																															
PRE	Pulp Suspension, Return	green																																																															
Material List																																																																	
Code	Material																																																																
SST	Stainless Steel Pipe																																																																
PVC	Polyvinylchloride Hose																																																																
PUR	Polyurethane Hose																																																																
Equipment List																																																																	
Code	Description	Type																																																															
B1	Storage Tank, Stirred	10 l																																																															
B2	Fines Tank	5 l																																																															
B3	Storage Tank	15 l																																																															
H1	Hydrodynamic Filtration Device																																																																
P1	Peristaltic Pump	P food&pharma19 twin-GM/FUC/FL																																																															
P2	Peristaltic Pump	ECOLINE VC-281																																																															
V1M	Pressure Reducing Valve	RS - 278-8774																																																															
V2M	Shut-off Valve	SMC Serie VHK Pneumatik-Steuerventil																																																															
V3M	Shut-off Valve	SMC Serie VHK Pneumatik-Steuerventil																																																															
V4M	Shut-off Valve	SMC Serie VHK Pneumatik-Steuerventil																																																															
V5M	Shut-off Valve	Gardena - 8194																																																															
V6M	Shut-off Valve	Gardena - 8194																																																															
V7M	Shut-off Valve	Gardena - 8194																																																															
V8M	Shut-off Valve	Gardena - 8194																																																															
V9M	Shut-off Valve	-																																																															
V10M	Pressure Control Valve	-																																																															
V11M	Pressure Control Valve	-																																																															
V12M	Pressure Control Valve	-																																																															
V13P	Pressure Relief Valve	1 bar																																																															
<table border="1"> <tr> <td rowspan="2">  </td> <td>Zul. Abweichung</td> <td>Oberfläche</td> <td>Maßstab</td> <td>Masse</td> </tr> <tr> <td>Allgemeintoleranz DIN ISO 2768-mk</td> <td></td> <td>-</td> <td></td> </tr> <tr> <td></td> <td>Gezeichnet</td> <td>Datum</td> <td>Name</td> <td rowspan="3">Titel</td> </tr> <tr> <td></td> <td>6/23/2015</td> <td></td> <td>Josef König</td> </tr> <tr> <td></td> <td>Kontrolliert</td> <td></td> <td></td> </tr> <tr> <td></td> <td>Norm</td> <td></td> <td></td> <td rowspan="2">P&amp;ID of HFD</td> </tr> <tr> <td></td> <td></td> <td></td> <td></td> </tr> <tr> <td></td> <td></td> <td></td> <td></td> <td rowspan="2">Zeichnungsnummer</td> </tr> <tr> <td></td> <td></td> <td></td> <td></td> </tr> <tr> <td></td> <td></td> <td></td> <td></td> <td rowspan="2">IPPT/F-2015-0/900</td> </tr> <tr> <td></td> <td></td> <td></td> <td></td> </tr> <tr> <td></td> <td></td> <td></td> <td></td> <td rowspan="2">3 A4</td> </tr> <tr> <td></td> <td></td> <td></td> <td></td> </tr> <tr> <td>Status</td> <td>Änderungen</td> <td>Datum</td> <td>Name</td> <td></td> </tr> </table>				Zul. Abweichung	Oberfläche	Maßstab	Masse	Allgemeintoleranz DIN ISO 2768-mk		-			Gezeichnet	Datum	Name	Titel		6/23/2015		Josef König		Kontrolliert				Norm			P&ID of HFD									Zeichnungsnummer									IPPT/F-2015-0/900									3 A4					Status	Änderungen	Datum	Name	
	Zul. Abweichung	Oberfläche		Maßstab	Masse																																																												
	Allgemeintoleranz DIN ISO 2768-mk		-																																																														
	Gezeichnet	Datum	Name	Titel																																																													
	6/23/2015		Josef König																																																														
	Kontrolliert																																																																
	Norm			P&ID of HFD																																																													
				Zeichnungsnummer																																																													
				IPPT/F-2015-0/900																																																													
				3 A4																																																													
Status	Änderungen	Datum	Name																																																														



**B.3 P&ID for HFD**



		Projektname Hydrofiter	Blatt 2
Auftraggeber Allg. Industrie- und Gewerbebau AG	Datum 12/2015	Zeichner JAM/BJG	P&ID of HFD
Projekt IPPT/F-2015-0/900	Blatt 2	Blatt A2	Blatt A2

**Fig. B-2: P&ID of the HFD. The main channel flow rate is controlled via the height of the liquid in stirred storage tank B1 and the height of the liquid in the bucket B3.**

## Appendix C Experimental data

Table C-1: Operating parameters and results of the experiments.

ID	gID	Oper.	$\bar{m}_{inC}$	$\bar{m}_{outJ}$	$C_{inC}$	$C_{outJ}$	$\Phi^+$	$t_{impulse}$	$t_{pause}$
-	-	-	g/min	g/min	%	%	-	s	s
0510-1	2	HS-P	1877	35	0.487	0.045	0.019	0.05	10.0
0510-2	2	HS-P	2017	73	0.482	0.033	0.038	0.05	5.0
<b>1610-1</b>	<b>2</b>	<b>HS-P</b>	<b>2124</b>	<b>34</b>	<b>0.121</b>	<b>0.009</b>	<b>0.016</b>	<b>0.05</b>	<b>10.0</b>
1610-2	2	HS-P	2194	71	0.132	0.017	0.033	0.05	5.0
2710-1	2	HS-P	706	34	0.078	0.006	0.051	-	-
2710-2	2	HS-P	740	35	0.105	0.004	0.049	0.05	10.0
2910-1	1	HS-P	2052	33	0.082	0.005	0.016	0.05	2.5
1612-1	3	HS-P	465	10	0.060	0.002	0.023	-	-
1612-2	3	HS-P	1348	20	0.129	0.005	0.015	-	-
2112-1	4	HS-P	220	10	0.100		0.050	-	-
2212-1	2	HS-P	2096	37	0.113	0.009	0.018	-	-
2212-2	2	HS-P	684	10	0.099	0.001	0.015		
1101-1	1	HS-P	693	11	0.098	0.002	0.015	0.05	20.00
1301-1	2	HS-P	2140	94	0.097	0.030	0.046	0.05	20.00
1301-2	2	HS-P	2231	11	0.112	0.002	0.005	0.05	180.00
2402-1	2	HS-P	721	37	0.066	0.018	0.053	-	-
0303-1	5	HS-P	2891	47	0.108	0.007	0.017	0.05	180.00
0303-2	5	HS-P	2949	144	0.120	0.024	0.051	0.05	180.00
0303-3	5	HS-P	969	47	0.075	0.004	0.051	0.05	180.00
0303-4	5	HS-P	915	20	0.086	0.001	0.023	0.05	180.00

Table C-2: Description of the geometry ID's used in Table C-1.

gID	H	W	geometry	SCW
1	15	3	90	1
2	15	3	20	0.75
3	9	3	20	0.75
4	3	3	20	0.75
5	15	9	20	0.75

## Appendix D CFD Simulations

### D.1 Geometries

The simulation of a certain flow situation requires a precise reproduction of the given geometrical situation. The measurement of the pressure drop is carried out for one open side channel. The goal of the simulations is to mimic exactly the conditions at the experiment, thus the pressure drop across the last side channel is to be simulated.

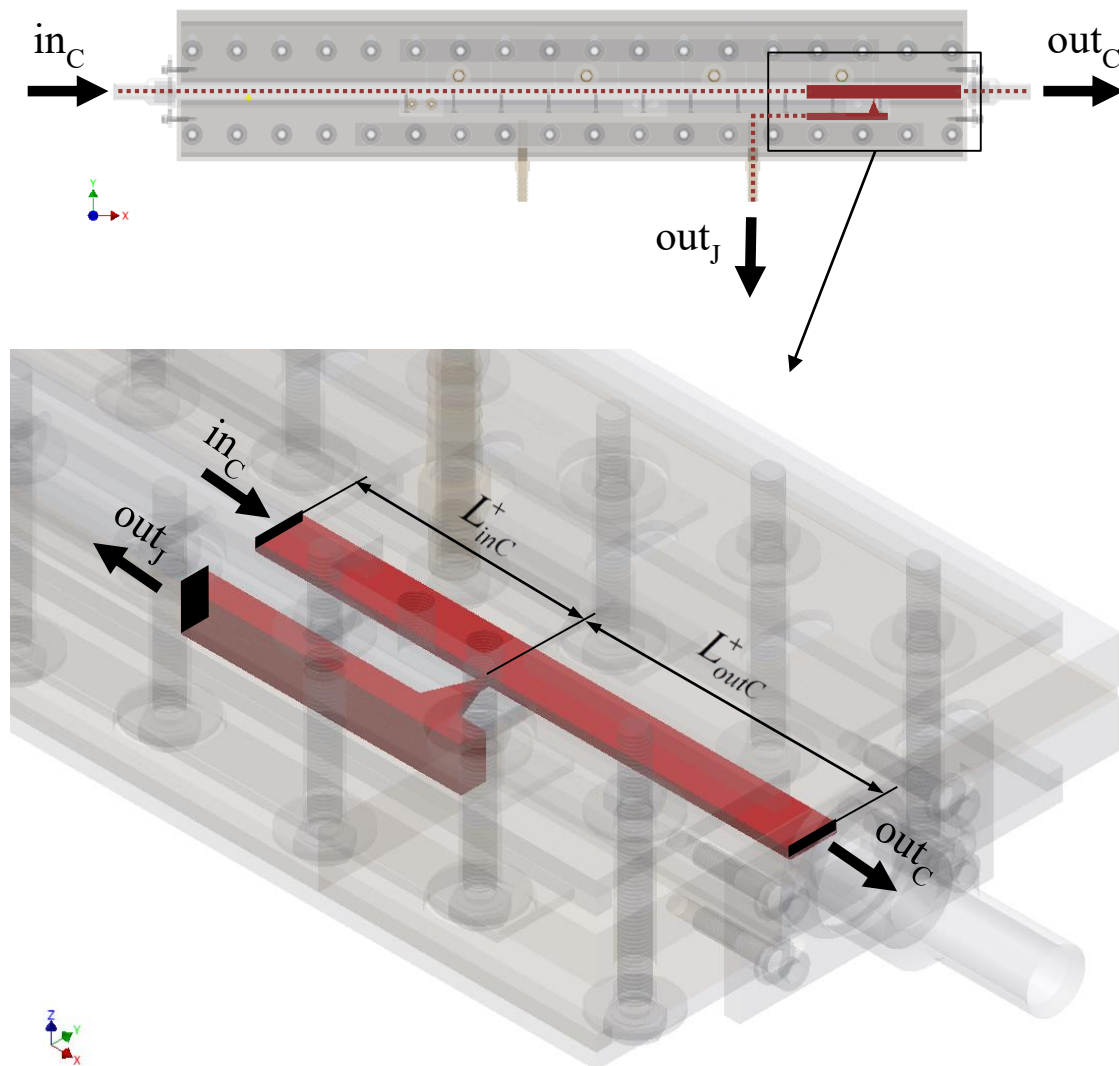


**Fig. D-1: Geometry of the flow situation at a single side channel. Fluid passes the three black colored faces inC, outC and outJ.**

The distance in upstream direction of the junction  $L_{inC}^+$  is set to 5, the distance in downstream direction  $L_{outC}^+$  is 6.5, where the index “+” indicates that the lengths are normalized with the channel height. As shown by König [34], the inlet length  $L_{inC}^+$  has almost no influence on the pressure drop, so this length is kept shorter to reduce the computational effort. The outlet length  $L_{outC}^+$  allows the flow to develop its final profile

after the removal of liquid at the side channel. The widening after the side channel entry aims to reduce the velocity and thus the pressure drop towards the side channel outlet. A detailed description of the geometries is shown in chapter REF {eine Detailansicht der Seitenkanalgeometrie wird im Kapitel Experimente genau beschrieben}

## **D.2 Meshing**

When applying the finite volume method for CFD, the simulation domain needs to be divided into multiple volume elements. This meshing can be done in an automated fashion with build-in tools in OpenFOAM like *snappyHexMesh*, creating a mesh from a given volume, e.g. a stl-geometry designed with CAD. However, those meshes can include cells with high aspect ratios in some cases, and are causing problems when solving the equations. Therefore, we use a semi-automatic method to build the meshes. This is done by applying the tools *blockMesh* and *extrudeMesh*, where the geometry of the cells can be well-defined [37]. The mesh of the main channel is built with *blockMesh*, the side channel geometry is built by repeatedly applying the *extrudeMesh* tool. Further, the mesh is mirrored across the  $x$ - $y$ -plane to ensure symmetry. Since the area near the side channel entry is of interest, the mesh is built finer in this region, where the splitting of the flow takes place.

The meshes for both geometries are shown in Fig. D-2 and Fig. D-3, where a total number of 650,000 cells is desired. Usually, the total number of cells is varied by a factor of 2-3 to determine if the mesh has an effect on the solution and thus the resulting flow field and pressures. So these meshes are refined in a next step to achieve a total number of cells of 2 million.

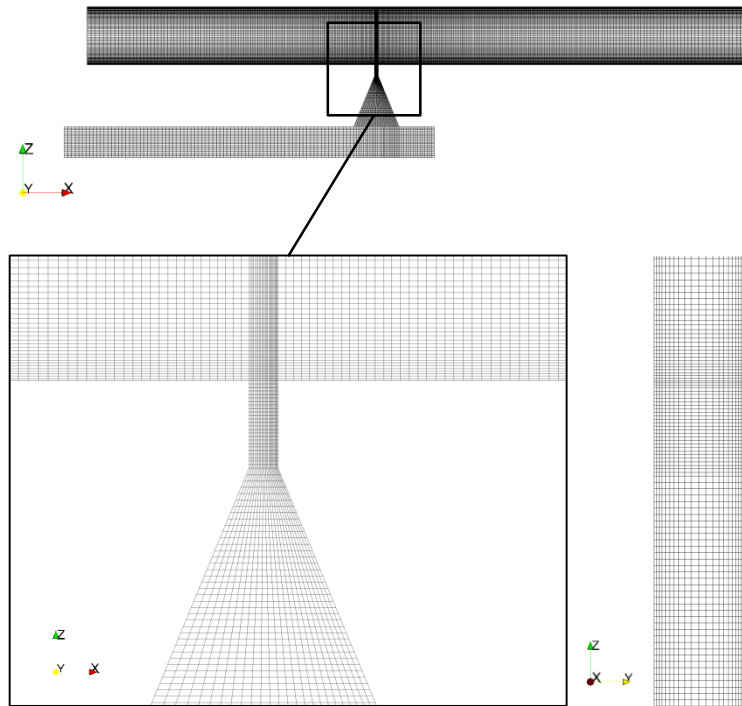


**Fig. D-2: Mesh of the 90° standard geometry, built with blockMesh and extrudeMesh. The cells in the side channel region are smaller with increasing x-position, because higher gradients are expected at this side. The total number of cells is approx. 650 000.**

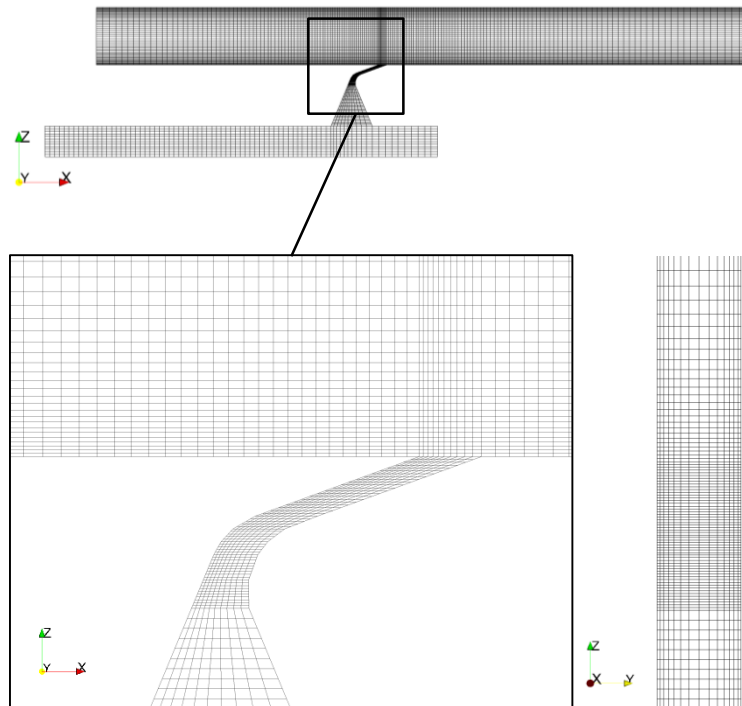


**Fig. D-3: Mesh for the 20° geometry, built with blockMesh and extrudeMesh. The mesh is finer at the left wall of the side channel, because the fluid is expected to be located there due to inertia. The total number of cells for this mesh is approx. 650,000.**

### D.3 Numerical schemes

To guarantee a satisfying accuracy of the solution, DNS is applied. Contrary to RANS or LES approaches, in DNS all scales are fully resolved, which requires a mesh size in the scale of the smallest eddies. Because of its stability and dynamic behavior, the *pimpleFOAM* solver is used in OpenFOAM®. The settings for the discretization schemes used are shown in Table D-1. A detailed description of the discretization schemes and other options is available on the openFOAM website [37].

**Table D-1: Settings for the numerical schemes used in openFOAM.**

keyword	scheme	value
ddtSchemes	default	backward
gradSchemes	default	Gauss linear
	grad(p)	Gauss linear
	grad(u)	Gauss linear
divSchemes	default	none
	div(phi,u)	Gauss limitedLinearV 1
	div(phi,nuTilda)	Gauss limitedLinear 1
	div((nuEff*dev(T(grad(u)))))	Gauss linear
laplacianSchemes	default	none
	laplacian(nuEff,u)	Gauss linear corrected
	laplacian(rAUf,p)	Gauss linear corrected
interpolationSchemes	default	linear
	interpolate(u)	linear
snGradSchemes	default	corrected
fluxRequired	default	no
	p	

### D.4 Boundary conditions and initial values

At least as important as to have the proper mesh, the correct definition of boundary conditions is essential. Both for the velocity field and the pressure field we need to define an initial value for each cell, which is zero in both cases usually. Note that in simulations negative pressures can be used, which is of course unnatural but numerically correct, since we can apply ambient pressures with no limitations.

Patches, which are a sum of cell faces of a certain area, are used in OpenFOAM® to set the boundary conditions. For example, all cell faces at the main channel inlet are defined as patch *inC*. All faces that represent an element of the channel wall are grouped in the patch *wall*. The no-slip condition at the wall is fulfilled by simply setting the velocity to zero. For the pressure field, we then need to set the *zeroGradient* boundary condition, which can be derived from the navier-stokes equations when applying zero velocity at the walls. This boundary condition is also used for the inlet, because we do not expect the pressure to change over the inlet patch. The pressure at the outlet *outC* is set to zero, so the pressure we define at the side channel outlet *collChannelxm* is equal to the total pressure difference. The boundary condition for the velocity at the two outlet patches is set to *inletOutlet*, not allowing any backflow over the patch face.

**Table D-2: Initial values and boundary conditions used for the simulations in openFOAM.**

<b>initial values</b>		
<b>field</b>	<b>type</b>	<b>value</b>
p	uniform	0
u	uniform	0
<b>boundary conditions pressure field</b>		
<b>field</b>	<b>type</b>	<b>value</b>
inC	zeroGradient	-
outC	uniform	0
collChannelxm	uniform	-0.3 ... 0.3
wall	zeroGradient	-
<b>boundary conditions velocity field</b>		
<b>field</b>	<b>type</b>	<b>value</b>
inC	nonuniform List	calc. with <i>setInletVelocity</i>
outC	inletOutlet	-
collChannelxm	inletOutlet	-
wall	fixedValue	(0 0 0)

At the inlet face, a laminar velocity profile is assumed. This is realized by simply calculating the velocity at the inlet patch at all positions. The solution of the velocity profile for non-circular cross-sections is given by Tamayol and Bahrami [38], the resulting inlet flow profile shown in Fig. D-4.

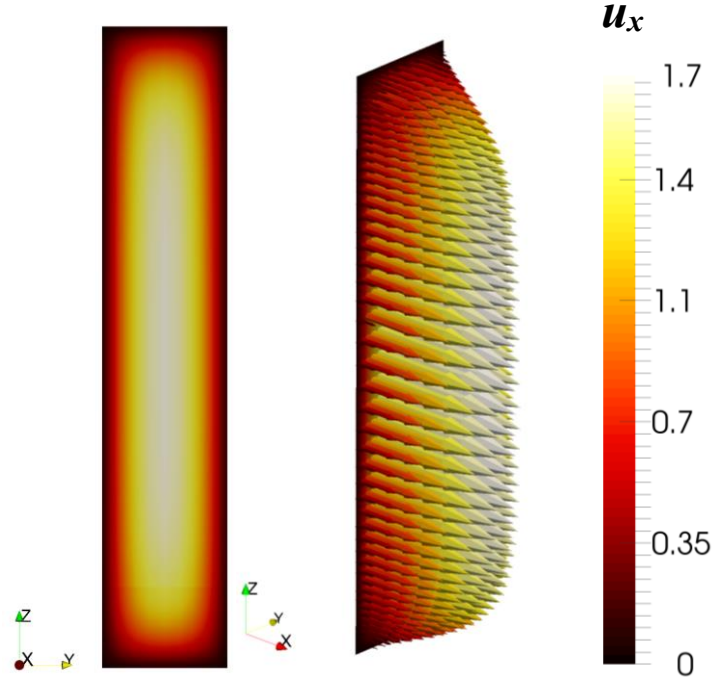


**Fig. D-4: Velocity profile imposed at the inlet patch in C, created with setInletVelocity with the solution of Tamayol and Bahrami [38].**

To adjust the Reynolds number, the kinematic viscosity  $\nu$  is varied, while the mean inlet velocity  $\bar{u}_{inC}$  is set to 1 in all simulations. The Reynolds number is calculated with the hydraulic diameter of the channel. For an arbitrary rectangular channel this gives:

$$\nu = \frac{\bar{u}_{inC} \cdot d_h}{Re} \quad (D-1)$$

The channel height is 1 by definition, so to get a hydraulic diameter of 1 also the channel width had to be 1, which is not the case in most of the simulations. For this reason, viscosity  $\nu$  is multiplied with the hydraulic diameter  $d_h^+$  to get the viscosity  $\nu^+$ , which is used in the simulations.

$$\nu = \frac{\bar{u}_{inC}}{Re} \frac{d_h^+}{d_h^+} \quad (D-2)$$

$=_{d_h=1}$

$$\nu d_h^+ = \nu^+ = \frac{\bar{u}_{inC} d_h^+}{Re} = \frac{2\bar{u}_{inC} W^+ L^+}{Re(W^+ + L^+)} \quad (D-3)$$

## Appendix E Calculations

### E.1 Correlation between total flow rates and relative flow fraction

One of the key factors of the separation mechanism is the volumetric flow fraction  $\Phi^+$ , defined as:

$$\Phi^+ = \frac{\dot{V}_{outJ}}{\dot{V}_{outC}} \quad (\text{E-1})$$

In the experimental device, only the total flow rates at the main channel in- and outlet and side channel outlet can be controlled. Thus, we need to determine the relationship between the volumetric flow fraction, which is typically set to a certain value, and the total flow rates that can be controlled during operation. The flow situation in a hydrodynamic filtration device with  $n$  side channels can be sketched as shown in Fig. E-1.

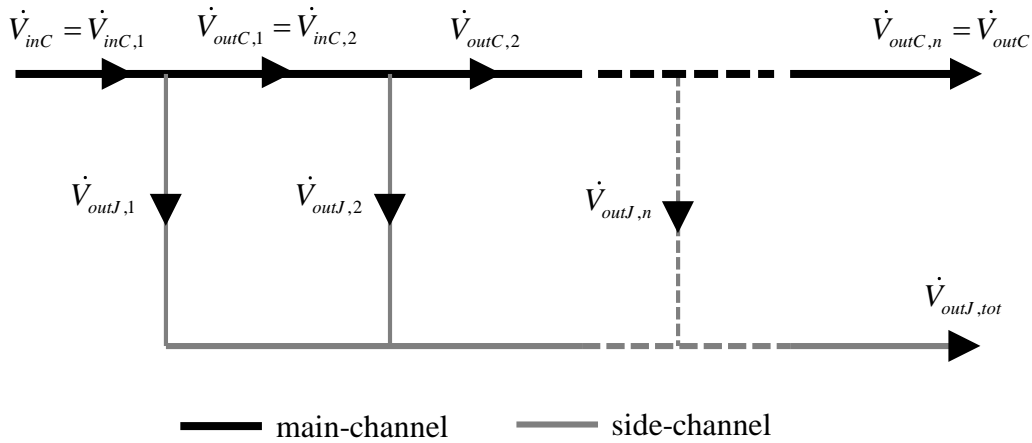


Fig. E-1: Flow rates at the main channel with multiple side channels.

We now assume that the volumetric flow fraction has the same value for every junction:

$$\frac{\dot{V}_{outJ,1}}{\dot{V}_{outC,1}} = \frac{\dot{V}_{outJ,2}}{\dot{V}_{outC,2}} = \frac{\dot{V}_{outJ,n}}{\dot{V}_{outC,n}} = \Phi^+ \quad (\text{E-2})$$

This might not be exactly the case in reality because the volumetric flow fraction depends on the pressure difference at the outlets, but if we assume that the pressure drop along the main channel is low compared to the pressure drop in side channel direction, this should be valid.

Balancing the volumetric flow rates around side channel 1 gives:

$$\dot{V}_{inC,1} = \dot{V}_{outC,1} + \dot{V}_{outJ,1} \quad (\text{E-3})$$

By using the volumetric flow fraction as shown above we get:

$$\dot{V}_{inC,1} = \dot{V}_{outC,1} + \dot{V}_{outC,1} \Phi^+ = \dot{V}_{outC,1} (1 + \Phi^+) \quad (\text{E-4})$$

$$\dot{V}_{outC,1} = \dot{V}_{inC,1} \frac{1}{1 + \Phi^+} = \dot{V}_{inC,2} \quad (\text{E-5})$$

The same procedure for side channel 2 gives:

$$\underbrace{\dot{V}_{inC,1} \frac{1}{1 + \Phi^+}}_{=\dot{V}_{inC,2}} = \dot{V}_{outC,2} + \dot{V}_{outC,2} \Phi^+ = \dot{V}_{outC,2} (1 + \Phi^+) \quad (\text{E-6})$$

$$\dot{V}_{outC,2} = \dot{V}_{inC,1} \left( \frac{1}{1 + \Phi^+} \right)^2 \quad (\text{E-7})$$

This routine can be applied to an arbitrary number of side channels  $n$ , which finally gives:

$$\dot{V}_{outC,n} = \dot{V}_{inC,1} \left( \frac{1}{1 + \Phi^+} \right)^n \quad (\text{E-8})$$

The total volumetric flow rate at the side channel after  $n$  side channels can now be determined with the overall balance of the form:

$$\dot{V}_{inC,1} = \dot{V}_{outC,n} + \dot{V}_{outJ,tot} = \dot{V}_{inC,1} \left( \frac{1}{1 + \Phi^+} \right)^n + \dot{V}_{outJ,tot} \quad (\text{E-9})$$

$$\dot{V}_{outJ,tot} = \dot{V}_{inC,1} - \dot{V}_{inC,1} \left( \frac{1}{1 + \Phi^+} \right)^n = \dot{V}_{inC,1} \left( 1 - \left( \frac{1}{1 + \Phi^+} \right)^n \right) \quad (\text{E-10})$$

Now we can define a normalized volume flow fraction  $\Psi^+$  that represents the total fraction of liquid which is removed based on the flow rate at the inlet.

$$\Psi^+ = \frac{\dot{V}_{outJ,tot}}{\dot{V}_{inC}} = 1 - \left( \frac{1}{1 + \Phi^+} \right)^n \quad (\text{E-11})$$

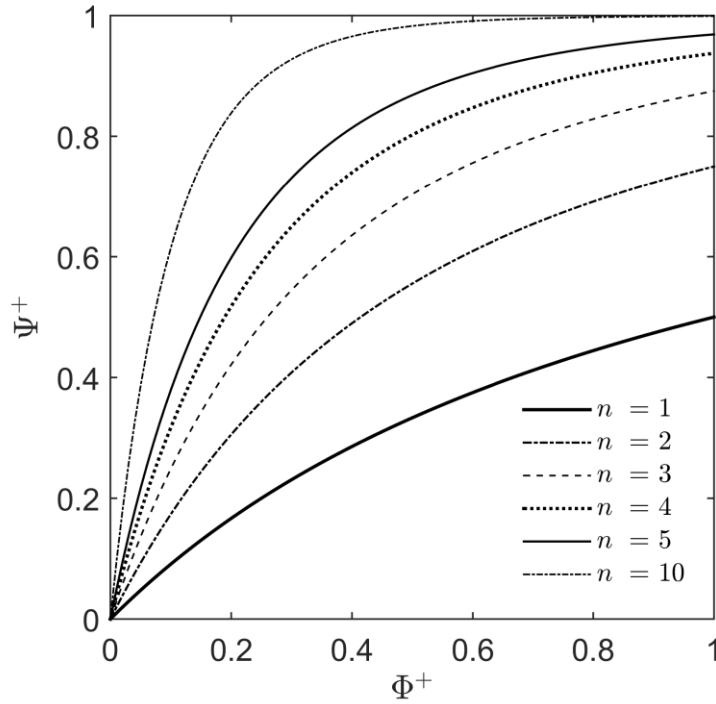


**Fig. E-2: Total fraction of the inlet flow  $\Psi^+$  depending on the relative flow fraction  $\Phi^+$  for different numbers of side channels.**

Fig. E-2 shows the total fraction of the inlet flow  $\Psi^+$  that has to be removed through the side channels to reach a desired volumetric flow fraction  $\Phi^+$  for different numbers of side channels. Obviously, by increasing the number of side channels the total flow rate of the side channels has to be increased. Note that  $\Phi^+$  can exceed a value of 1, while  $\Psi^+$  can only have values from 0 to 1, where 1 would mean that all incoming fluid is exiting the device via the side channels.

A satisfying separation performance is only given at low volumetric flow fractions. In the experiments, the highest value taken for  $\Phi^+$  is 0.2.

$$\Phi^+ = \frac{1}{(1 - \Psi^+)^{1/n}} - 1 \quad (\text{E-12})$$

## ***E.2 Separation efficiency with confidence intervals***

In the results of the separation efficiencies the standard deviation is used for the width of the error bars throughout this thesis. An alternative approach would be to describe the possible variations of the results with confidence intervals, as shown exemplarily in Fig. E-3.

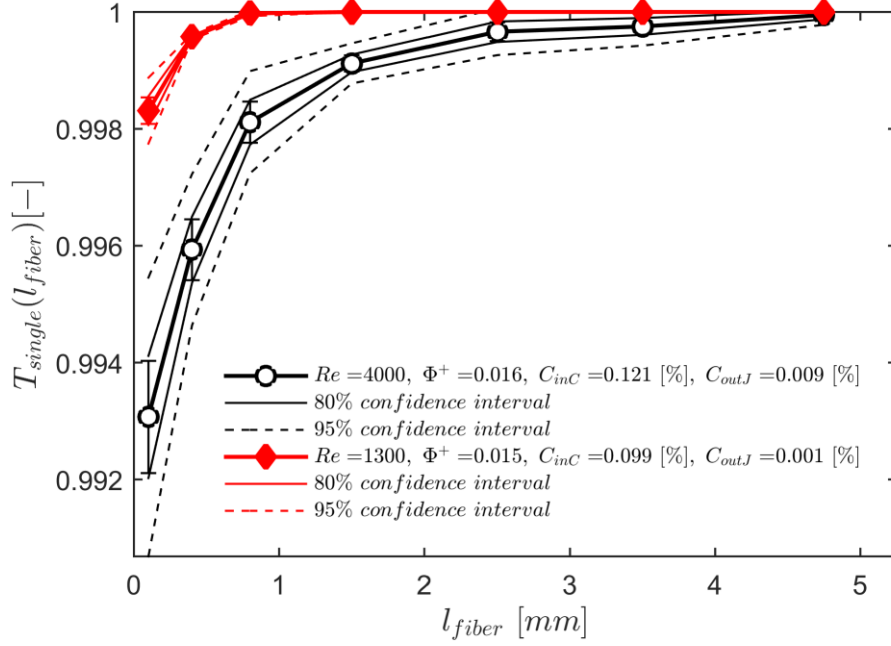


**Fig. E-3: Exemplary results of the separation efficiency, with error bars based on the standard deviation and confidence intervals.**

The intervals are calculated with:

$$\left[ \bar{x} - t_{\left(1-\frac{\alpha}{2}, n-1\right)} \frac{s}{\sqrt{n}}; \bar{x} + t_{\left(1-\frac{\alpha}{2}, n-1\right)} \frac{s}{\sqrt{n}} \right] \quad (\text{E-13})$$

The arithmetic mean  $\bar{x}$  of the characteristics and the root of the sample variance  $s^2$  are:

$$\bar{x} = \frac{\sum_i x_i}{n} \quad (\text{E-14})$$

$$s = \sqrt{\frac{\sum_i (x_i - \bar{x})^2}{n-1}} \quad (\text{E-15})$$

The value for the student t-distribution is tabulated in many sources [39]. In our experiments, the number of samples  $n$  was 3 in all cases. The more samples are taken, the narrower gets the confidence interval. Here, the value for the standard deviation as used for the error bars is close to an interval for a level of significance of 80%.

Since the intervals for a 95% confidence interval, which should always be desired, are quite large, it is recommended to take at least 10 samples when determining the separation efficiency curves.

### E.3 Dimensionless Navier-Stokes Equation

In the simulations, the flow of matter is predicted by solving differential equations for mass and momentum. By choosing an appropriate set of reference variables and making the equations dimensionless, the results of the simulations can be pictured in a more meaningful way. This procedure is shown in the following section.

The continuity equation for incompressible fluids is given by:

$$\frac{\partial \rho}{\partial t} + (\nabla \cdot \rho \mathbf{u}) = 0 \quad (\text{E-16})$$

Since the density  $\rho$  is constant in incompressible fluids,

$$(\nabla \cdot \mathbf{u}) = 0 \quad (\text{E-17})$$

follows from the continuity equation [28]. With this information, the momentum equation can now be written as the Navier-Stokes equation:

$$\frac{\partial \rho \mathbf{u}}{\partial t} + \nabla \cdot (\rho \mathbf{u} \mathbf{u}) = -\nabla p + \mu \Delta \mathbf{u} + \rho \mathbf{g} \quad (\text{E-18})$$

Because gravity is neglected in the calculations, the last term on the right hand side of Equ. (E-18) is not considered in further calculations. The Navier-Stokes Equation in the above form is given in dimensioned variables, making it inconvenient to apply the equation at different scales. By introducing a reference length, time and pressure, the Navier-Stokes equation can be expressed only in dimensionless variables.

$$t^* = \frac{t}{t_{ref}} \quad u^* = \frac{u}{u_{ref}} \quad p^* = \frac{p}{p_{ref}} \quad (\text{E-19})$$

$$t_{ref} = \frac{L}{U} \quad u_{ref} = U \quad p_{ref} = \rho U^2 \quad (\text{E-20})$$

Inserting this relationships in Equ. (E-18) and neglecting gravitational forces leads to:

$$\frac{U^2}{L} \frac{\partial \rho \mathbf{u}^*}{\partial t^*} + \frac{U^2}{L} \nabla^* \cdot (\rho \mathbf{u}^* \mathbf{u}^*) = -\frac{\rho U^2}{L} \nabla^* p^* + \frac{U}{L^2} \mu \Delta^* \mathbf{u}^* \quad (\text{E-21})$$

This equation can be rewritten in more compact form:

$$\frac{\partial \mathbf{u}^*}{\partial t^*} + \nabla^* \cdot (\mathbf{u}^* \mathbf{u}^*) = -\nabla^* p^* + \frac{\mu}{\rho L U} \Delta^* \mathbf{u}^* \quad (\text{E-22})$$

$= \frac{1}{Re}$

In the simulation, the reference variables are chosen with

$$L = d_h \quad U = \bar{u}_{inC} \quad (E-23)$$

This allows an easy comparison of simulation results and experimentally measured values. For example, the measured pressure at a certain position  $p_{exp}$  can be made dimensionless by applying:

$$p^+ = \frac{P_{exp}}{U^2 \rho} = \frac{P_{exp}}{\bar{u}_{inC}^2 \rho} \quad (E-24)$$

#### **E.4 Pressure drop model**

The pressure drop in the main channel is simulated in using OpenFOAM®. In the work of König [34], a model for the relationship between pressure and volumetric flow fraction was developed. This model has been slightly adopted to represent the flow situation as present in the experimental device.

The basic equation

$$\Delta p \propto \frac{\langle \bar{u}_i \rangle^n L \mu^k \rho^r}{d_h^m} \quad (E-25)$$

can be used for different flow regimes, as the parameters can be adjusted to the actual flow situation. For laminar flows, the parameter set 2,1,1,0 for  $m,n,k,r$  respectively, represent a linear dependency of the pressure drop on the flow velocity as known by the Hagen-Poiseuille equation [28]. In presence of turbulent flow, the parameter set 1,2,0,1 for  $m,n,k,r$  respectively, can be used to describe the quadratic dependence of the pressure drop on the flow velocity.

The hydraulic diameter  $d_h$  is defined as

$$d_h = \frac{4A}{U} \quad (E-26)$$

$$d_{h,C} = \frac{4L^+W^+}{2(L^+ + W^+)} = \frac{2L^+W^+}{(L^+ + W^+)} \quad (E-27)$$

$$d_{h,SC} = \frac{4SCW^+W^+}{2(SCW^+ + W^+)} = \frac{2SCW^+W^+}{(SCW^+ + W^+)} \quad (E-28)$$

The relationship between volumetric flow fraction and pressure is determined by applying the Bernoulli-equation [28] from the beginning of the side channel both to the end of the main and side channel.

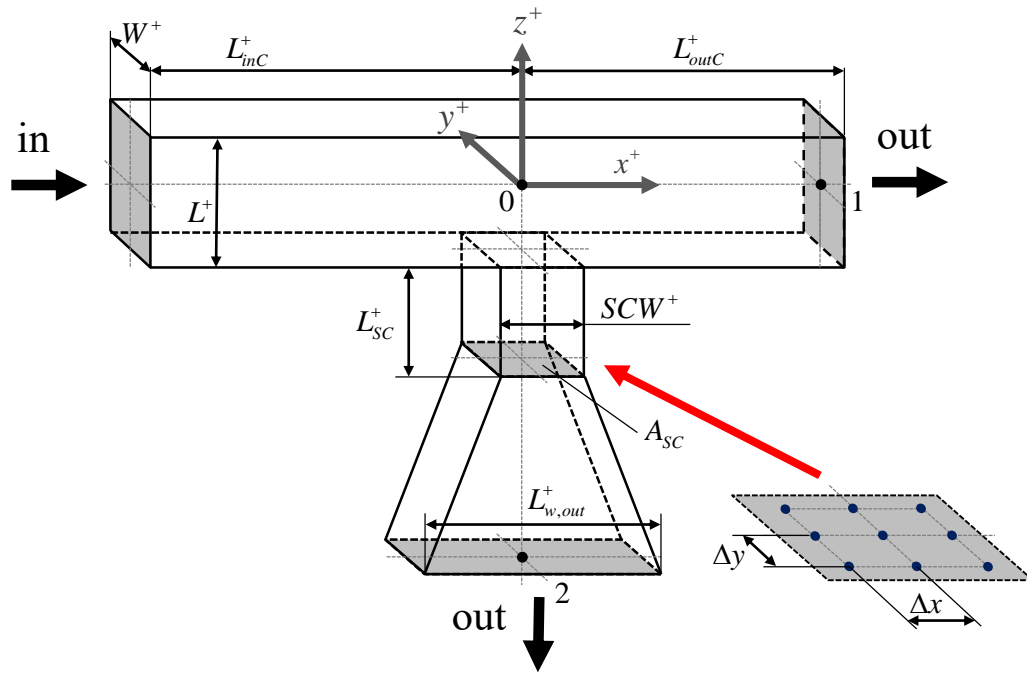


**Fig. E-4: Geometrical situation of the 90° geometry. All dimensions are normalized with the channel height  $L^+$ . The pressure at the plane  $A_{SC}$  is determined by averaging the pressure at 9 measurement points in the simulation.**

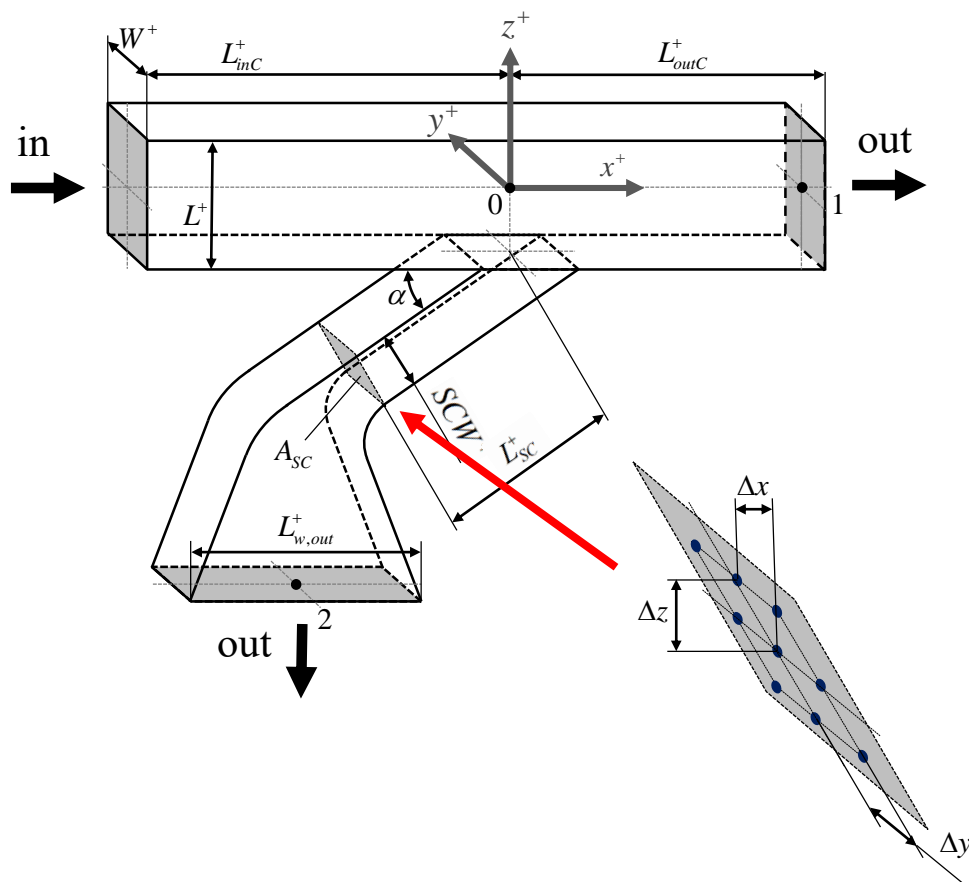


**Fig. E-5: Geometrical situation of the 20° geometry. All dimensions are normalized with the channel height  $L^+$ . The pressure at the plane  $A_{SC}$  is determined by averaging the pressure at 9 measurement points in the simulation.**

The Bernoulli equation from point 0 to 1 is

$$\begin{aligned} \frac{\bar{p}_{stat,0}}{\rho_{Fluid}} + \pi_C \frac{\langle \bar{u}_{inC} \rangle^2}{2} = \\ \frac{\langle \bar{p}_{stat,outC} \rangle}{\rho_{Fluid}} + \frac{\langle \bar{u}_{outC} \rangle^2}{2} + \frac{\langle \bar{u}_{outC} \rangle^n L_{outC}^+ (L^+ + W^+)^m}{(2L^+W^+)^m} \zeta \mu^k \rho^{r-1} \end{aligned} \quad (E-29)$$

In the Bernoulli equation from point 0 to 2 the widening of the side channel has to be taken into account. In general, the pressure drop in a continuous cross-section widening  $\Delta p_w$  can be modeled with

$$\begin{aligned} \frac{\Delta p_w}{\rho_{Fluid}} = \frac{\langle \bar{u}_{SC} \rangle^2}{2} \left( 1 - \frac{A_{SC}}{A_{outJ}} \right)^2 \zeta_{wid,SC} = \\ \frac{\langle \bar{u}_{SC} \rangle^2}{2} \left( 1 - \frac{SCW^+W^+}{L_{w,out}^+ W^+} \right)^2 \zeta_{wid,SC} = \frac{\langle \bar{u}_{SC} \rangle^2}{2} \left( 1 - \frac{SCW^+}{L_{w,out}^+} \right)^2 \zeta_{wid,SC} \end{aligned} \quad (E-30)$$

where  $\zeta_w$  is a loss coefficient and a function of the diameters at the beginning and the end of the widening [35].  $A_{SC}$  and  $A_{outJ}$  are the cross-sectional areas of the widening,  $u_{SC}$  is the velocity in the side channel and thus at the beginning of the widening. The Bernoulli from point 0 to 2 is then

$$\begin{aligned} \frac{\bar{p}_{stat,0}}{\rho_{Fluid}} + \pi_J \frac{\langle \bar{u}_{inC} \rangle^2}{2} = \\ \underbrace{\frac{\langle \bar{p}_{stat,outJ} \rangle}{\rho_{Fluid}}}_{=\Delta p^+} + \frac{\langle \bar{u}_{outJ} \rangle^2}{2} + \frac{\langle \bar{u}_{SC} \rangle^n L_{SC}^+ (SCW^+ + W^+)^m}{(2SCW^+W^+)^m} \zeta_J \zeta \mu^k \rho^{r-1} \\ + \frac{\langle \bar{u}_{SC} \rangle^2}{2} \left( 1 - \frac{SCW^+}{L_{w,out}^+} \right)^2 \zeta_{wid,SC} \end{aligned} \quad (E-31)$$

Since the static pressure at the main channel outlet at point 1 is set to 0 in all simulations, the pressure at the outlet equals the pressure difference  $\Delta p^+$ . The direction of the flow in the main channel plays also a role regarding the dynamic pressure. By adding factors  $\pi_C$  and  $\pi_J$ , this is taken into account.

0-1

$$\frac{\bar{p}_{stat,0}}{\rho_{Fluid}} + \pi_C \frac{\langle \bar{u}_{inC} \rangle^2}{2} = \frac{\langle \bar{p}_{stat,outC} \rangle}{\underbrace{\rho_{Fluid}}_{=0}} + \frac{\langle \bar{u}_{outC} \rangle^2}{2} + \frac{\langle \bar{u}_{outC} \rangle^n L_{outC}^+ (L^+ + W^+)^m}{(2L^+W^+)^m} \zeta \mu^k \rho^{r-1} \quad (\text{E-32})$$

0-2

$$\frac{\bar{p}_{stat,0}}{\rho_{Fluid}} + \pi_J \frac{\langle \bar{u}_{inC} \rangle^2}{2} = \Delta p^+ + \frac{\langle \bar{u}_{outJ} \rangle^2}{2} + \frac{\langle \bar{u}_{SC} \rangle^n L_{SC}^+ (SCW^+ + W^+)^m}{(2SCW^+W^+)^m} \zeta_J \zeta \mu^k \rho^{r-1} \quad (\text{E-33})$$

$$+ \frac{\langle \bar{u}_{SC} \rangle^2}{2} \left( 1 - \frac{SCW^+}{L_{w,out}^+} \right)^2 \zeta_{wid,SC}$$

Subtracting equation (E-32) from (E-33) gives

$$\Delta p^+ = \frac{\langle \bar{u}_{inC} \rangle^2}{2} (\pi_J - \pi_C) + \frac{\langle \bar{u}_{outC} \rangle^2}{2} - \frac{\langle \bar{u}_{outJ} \rangle^2}{2} + \zeta \mu^k \rho^{r-1} \left( \frac{\langle \bar{u}_{outC} \rangle^n L_{outC}^+ (L^+ + W^+)^m}{(2L^+W^+)^m} - \frac{\langle \bar{u}_{SC} \rangle^n L_{SC}^+ (SCW^+ + W^+)^m \zeta_J}{(2SCW^+W^+)^m} \right) - \frac{\langle \bar{u}_{SC} \rangle^2}{2} \left( 1 - \frac{SCW^+}{L_{w,out}^+} \right)^2 \zeta_{wid,SC} \quad (\text{E-34})$$

We can replace all velocities with the inlet velocity by applying the relationships

$$\Phi^+ = \frac{\langle \bar{u}_{outJ} \rangle A_{outJ}}{\langle \bar{u}_{outC} \rangle A_{outC}} \quad (\text{E-35})$$

and

$$\langle \bar{u}_{inC} \rangle A_{outC} = \langle \bar{u}_{outC} \rangle A_{outC} + \langle \bar{u}_{outJ} \rangle A_{outJ} \quad (\text{E-36})$$

The velocities at the outlets are thus,

$$\langle \bar{u}_{outC} \rangle = \frac{\langle \bar{u}_{inC} \rangle}{\Phi^+ + 1} \quad (\text{E-37})$$

$$\langle \bar{u}_{outJ} \rangle = \frac{\langle \bar{u}_{inC} \rangle}{\Phi^+ + 1} \Phi^+ \frac{A_{outC}}{A_{outJ}} \quad (\text{E-38})$$

$$\langle \bar{u}_{SC} \rangle = \langle \bar{u}_{outJ} \rangle \frac{A_{outJ}}{A_{SC}} = \frac{\langle \bar{u}_{inC} \rangle}{\Phi^+ + 1} \Phi^+ \frac{A_{outC}}{A_{SC}} \quad (\text{E-39})$$

By combination of (E-34), (E-37), (E-38) and (E-39) we finally arrive at

$$\begin{aligned}
\Delta p^+ = & \frac{\langle \bar{u}_{inC} \rangle^2}{2} (\pi_J - \pi_C) + \frac{\left( \frac{\langle \bar{u}_{inC} \rangle}{\Phi^+ + 1} \right)^2}{2} - \frac{\left( \frac{\langle \bar{u}_{inC} \rangle}{\Phi^+ + 1} \Phi^+ \frac{A_{outC}}{A_{outJ}} \right)^2}{2} \\
& + \zeta \mu^k \rho^{r-1} \left( \frac{\left( \frac{\langle \bar{u}_{inC} \rangle}{\Phi^+ + 1} \right)^n L_{outC}^+ (L^+ + W^+)^m}{(2L^+ W^+)^m} - \frac{\left( \frac{\langle \bar{u}_{inC} \rangle}{\Phi^+ + 1} \Phi^+ \frac{A_{outC}}{A_{SC}} \right)^n L_{SC}^+ (SCW^+ + W^+)^m \zeta_J}{(2SCW^+ W^+)^m} \right) \quad (E-40) \\
& - \frac{\left( \frac{\langle \bar{u}_{inC} \rangle}{\Phi^+ + 1} \Phi^+ \frac{A_{outC}}{A_{SC}} \right)^2}{2} \left( 1 - \frac{SCW^+}{L_{w,out}^+} \right)^2 \zeta_{wid,SC}
\end{aligned}$$

This equation can be rewritten in a more compact form:

$$\begin{aligned}
\Delta p^+ = & \left( \frac{\langle \bar{u}_{inC} \rangle}{\Phi^+ + 1} \right)^2 \frac{1}{2} \left( (\pi_J - \pi_C) (\Phi^+ + 1)^2 + 1 - \left( \Phi^+ \frac{A_{outC}}{A_{outJ}} \right)^2 \right. \\
& \left. - \left( \Phi^+ \frac{A_{outC}}{A_{SC}} \left( 1 - \frac{SCW^+}{L_{w,out}^+} \right) \right)^2 \right) \zeta_{wid,SC} \quad (E-41) \\
& + \zeta \mu^k \rho^{r-1} \left( \frac{\langle \bar{u}_{inC} \rangle}{\Phi^+ + 1} \right)^n \left( \frac{L_{outC}^+ (L^+ + W^+)^m}{(2L^+ W^+)^m} - \frac{\left( \Phi^+ \frac{A_{outC}}{A_{SC}} \right)^n L_{SC}^+ (SCW^+ + W^+)^m \zeta_J}{(2SCW^+ W^+)^m} \right)
\end{aligned}$$

The main channel flow is in direction of the streamlines from point 0 to 1, so the dynamic pressure is contributing to the total pressure and thus  $\pi_C$  is 1. The situation in direction from point 0 to 2 is different, here we can set the dynamic pressure to 0, so that  $\pi_J$  is 0.

### ***E.5 Pressure drop in the experiments***

For computational reasons, the simulation domain was chosen to be only the relevant part for the characterization of the flow at the side channel. Since the pressure can only be measured before and after the main channel, we have to calculate the pressure that is present at the boundaries of the simulation domain. With this information we can then compare the results of the simulation with results of the measurements.

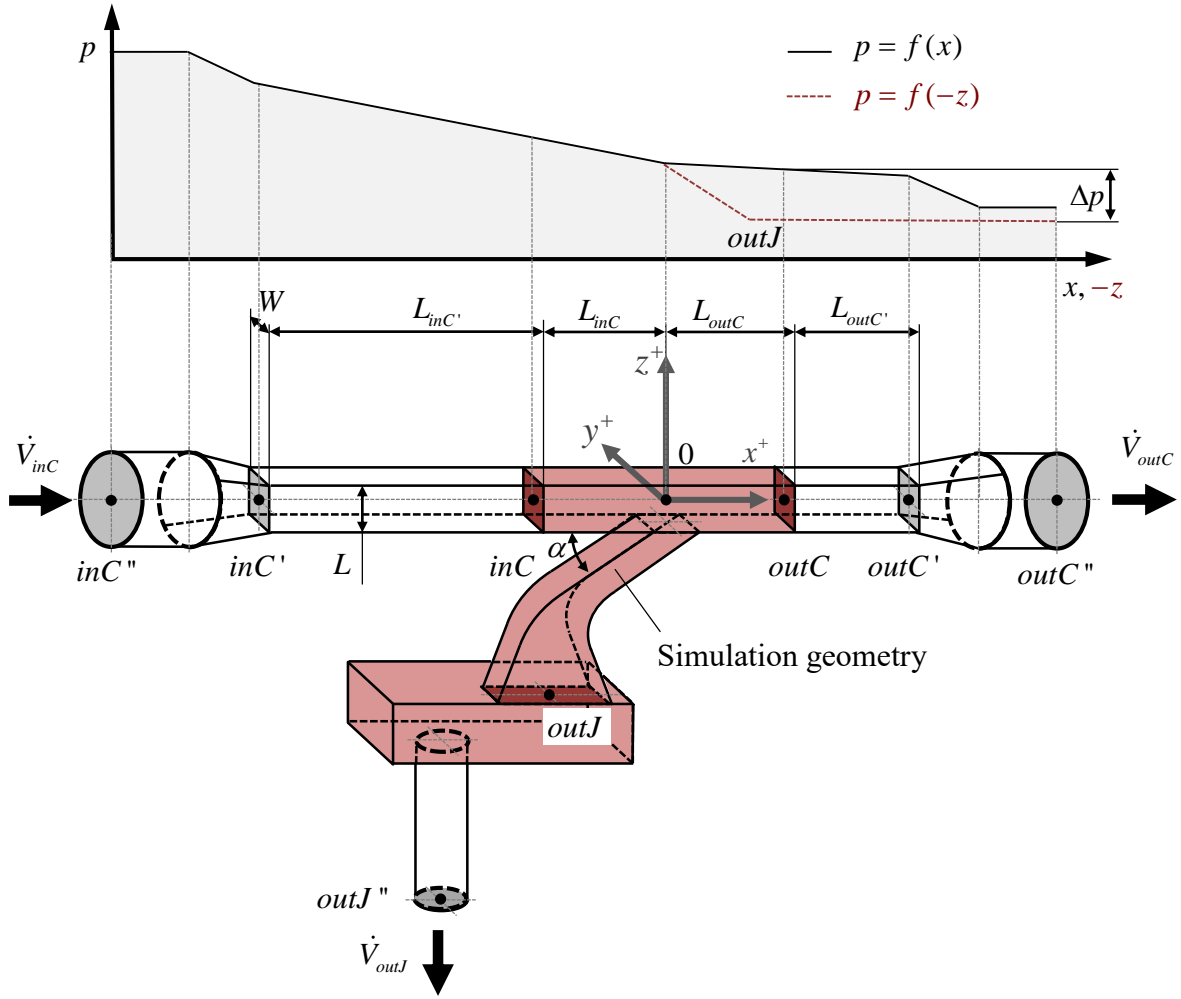


**Fig. E-6: Pressure drop in the HDF. The red colored area shows the part for which single-phase simulations are done.**

The Pressure drop at the contraction at the main channel inlet is modeled with

$$\Delta p = \frac{\rho \langle \bar{u}_{inC} \rangle^2}{2} \zeta_{cont} \quad (\text{E-42})$$

For low values of the contraction angle,  $\zeta_{cont}$  can be set to 0.04 according to VDI [35]. The pressure loss in contractions with low contraction angles is in general lower than in a widening, because of the fact that usually no separation of the fluid takes place in wall-near regions.

In the main channel, the pressure drop from the beginning of the rectangular section to the crossing point of the main and side channel is

$$\Delta p = \frac{\rho \langle \bar{u}_{inC} \rangle^2}{2} \underbrace{\frac{64}{Re} \phi_{AR} \phi_{Exp}}_{\lambda_{Exp}} \frac{L_{inC'} + L_{inC}}{d_h} = \frac{\rho \langle \bar{u}_{inC} \rangle}{2} \frac{64 \nu}{d_h^2} \phi_{AR} \phi_{Exp} (L_{inC'} + L_{inC}) \quad (\text{E-43})$$

The factors  $\phi_{Asp}$  and  $\phi_{Exp}$  describe the deviation of the friction coefficient in the actual experiment  $\lambda_{Exp}$  to the ideal friction coefficient  $\lambda$  in laminar flows.  $\phi_{AR}$  accounts for different aspect ratios of the rectangular channel [35],  $\phi_{Exp}$  is determined by evaluating the total pressure drop as shown later. In a perfect experimental setting with smooth walls and an aspect ratio of 0.44, where  $\phi_{AR}$  becomes 1,  $\phi_{Exp}$  should also become 1.

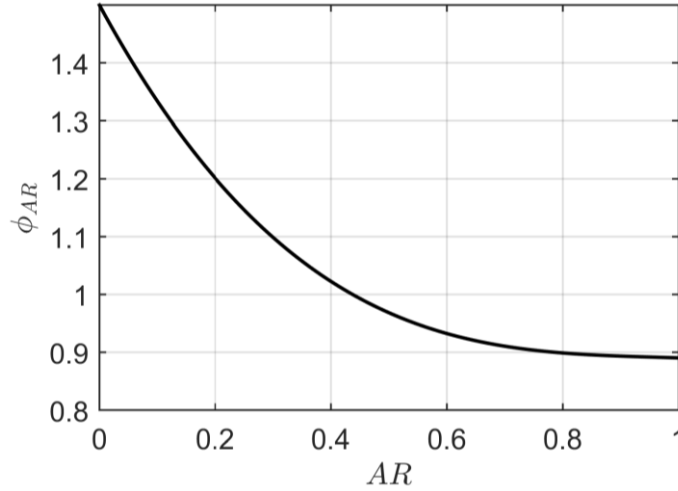


Fig. E-7: Factor  $\phi_{AR}$  as a function of the aspect ratio  $AR$ , as given in [35]

Similarly, the pressure drop from the crossing point of main and side channel can be written as

$$\Delta p = \frac{\rho < \bar{u}_{outC} >^2}{2} \frac{64}{Re} \phi_{Asp} \phi_{Exp} \frac{L_{outC} + L_{outC'}}{d_h} = \frac{\rho < \bar{u}_{outC} >}{2} \frac{64 \nu}{d_h^2} \phi_{Asp} \phi_{Exp} (L_{outC} + L_{outC'}) \quad (E-44)$$

Since the aspect ratio of the main channel does not change in flow direction,  $\phi_{Asp}$  is constant for both Equ. (E-43) and (E-44). Only a small amount of liquid is to be removed through the side channel, thus it is assumed that the flow regime does not change in the main channel and therefore the same value of  $\phi_{Exp}$  is used in both equations. The pressure drop in the main channel caused by removal of liquid at the side channel is not modeled at this point. The flow rate after the side channel is lower, resulting in a lower velocity  $u_{outC}$  and pressure drop, which is illustrated in Fig. E-6, where the slope of the pressure line is flatter after the side channel in  $x$  direction.

The last contribution to the total pressure drop in main channel direction is the pressure loss at the widening at the end of the main channel. There, the cross-sectional area changes from the rectangular main channel to the circular cross-section of the connected hose. In general, the pressure drop at a widening can be modeled according to VDI WärmAtlas [35] with

$$\Delta p = \frac{\rho \langle \bar{u}_{in} \rangle^2}{2} \zeta_{wid} \left( 1 - \frac{A_{in}}{A_{out}} \right)^2 \quad (\text{E-45})$$

The loss coefficient  $\zeta_{wide}$  is a function of the widening angle  $\beta_{wide}$  and the ratio of the diameters at the inlet and the outlet of the widening. For widening angles below 30°, as present in the experimental device, the loss coefficient is only a function of the widening angle [35].

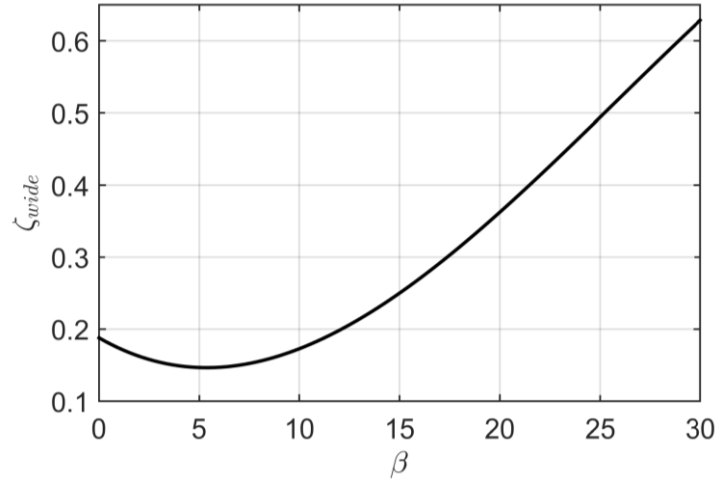


Fig. E-8: Loss coefficient  $\zeta_{wide}$  as a function of the widening angle  $\beta$ , as given in VDI [35].

The Bernoulli equation from the measurement point at the inlet  $inC''$  to the measurement point at the main channel outlet  $outC''$  is:

$$\begin{aligned} \frac{\rho \langle \bar{u}_{inC''} \rangle^2}{2} + \langle \bar{p}_{inC''} \rangle &= \frac{\rho \langle \bar{u}_{outC''} \rangle^2}{2} + \langle \bar{p}_{outC''} \rangle + \frac{\rho \langle \bar{u}_{inC} \rangle^2}{2} \zeta_{cont} \\ &+ \frac{\rho \langle \bar{u}_{inC} \rangle}{2} \frac{64\nu}{d_h^2} \phi_{Asp} \phi_{Exp} (L_{inC'} + L_{inC}) + \frac{\rho \langle \bar{u}_{outC} \rangle}{2} \frac{64\nu}{d_h^2} \phi_{Asp} \phi_{Exp} (L_{outC} + L_{outC'}) \\ &+ \frac{\rho \langle \bar{u}_{outC} \rangle^2}{2} \zeta_{wid} \left( 1 - \frac{A_{outC'}}{A_{outC''}} \right)^2 \end{aligned} \quad (\text{E-46})$$

The deviation from the ideal laminar flow in the experiment can be determined by isolating the factor  $\phi_{Exp}$  from Equ. (E-46):

$$\begin{aligned}
\phi_{Exp} = & \left( \frac{2}{\rho} (\langle \bar{p}_{inC''} \rangle - \langle \bar{p}_{outC''} \rangle) + \langle \bar{u}_{inC''} \rangle^2 - \langle \bar{u}_{outC''} \rangle^2 - \langle \bar{u}_{inC} \rangle^2 \zeta_{cont} \right. \\
& \left. - \langle \bar{u}_{outC} \rangle^2 \zeta_{wid} \left( 1 - \frac{A_{outC'}}{A_{outC''}} \right)^2 \right) \\
& / \left( \frac{64\nu}{d_h^2} \phi_{Asp} (\langle \bar{u}_{inC} \rangle (L_{inC'} + L_{inC}) + \langle \bar{u}_{outC} \rangle (L_{outC} + L_{outC'})) \right)
\end{aligned} \tag{E-47}$$

The desired pressure at point *outC* , which allows the comparison between experiment and simulation, is now calculated by simply deriving the Bernoulli equation from point 0 to *outC''* :

$$\begin{aligned}
\frac{\rho \langle \bar{u}_{outC} \rangle^2}{2} + \langle \bar{p}_{outC} \rangle = & \frac{\rho \langle \bar{u}_{outC''} \rangle^2}{2} + \langle \bar{p}_{outC''} \rangle + \frac{\rho \langle \bar{u}_{outC} \rangle}{2} \frac{64\nu}{d_h^2} \phi_{Asp} \phi_{Exp} L_{outC'} \\
& + \frac{\rho \langle \bar{u}_{outC} \rangle^2}{2} \zeta_{wid} \left( 1 - \frac{A_{outC'}}{A_{outC''}} \right)^2
\end{aligned} \tag{E-48}$$

This can be reformulated as:

$$\begin{aligned}
\langle \bar{p}_{outC} \rangle = & \frac{\rho}{2} (\langle \bar{u}_{outC''} \rangle^2 - \langle \bar{u}_{outC} \rangle^2) + \langle \bar{p}_{outC''} \rangle + \frac{\rho \langle \bar{u}_{outC} \rangle}{2} \frac{64\nu}{d_h^2} \phi_{Asp} \phi_{Exp} L_{outC'} \\
& + \frac{\rho \langle \bar{u}_{outC} \rangle^2}{2} \zeta_{wid} \left( 1 - \frac{A_{outC'}}{A_{outC''}} \right)^2
\end{aligned} \tag{E-49}$$

## E.6 Projection of the operating costs

In the following, the calculation of the operating costs is shown for 10 side channels along each main channel. The calculation for the case with 100 side channels is done analogously.

### E.6.1 Power draw of the main channel pump

The power draw of the main channel is calculated by assuming laminar flow in the main channel at  $Re = 4,000$ . We can calculate the power draw with:

$$P_{PumpC,tot} = \frac{\Delta p_C \frac{\dot{m}_{inC,tot,susp}}{\rho}}{\varepsilon_{Pump}} = \frac{\langle \bar{u}_{inC} \rangle^2 \rho \frac{64}{2} l_C \frac{\dot{m}_{inC,tot}}{\rho}}{\varepsilon_{Pump} Re d_h} = 81.3W \tag{E-50}$$

### E.6.2 Power draw for the side channel pump

The magnitude of the dimensionless pressure drop for a flow fraction of 0.015 is approx. 1, according to Fig. 5-3. The pressure drop is thus

$$\Delta p_{SC} = \Delta p_{SC}^+ < \bar{u}_{inC} >^2 \rho = 640 Pa \quad (E-51)$$

The total flow fraction of 10 side channels is calculated by applying Equ. (E-11):

$$\Psi^+ = 1 - \left( \frac{1}{1 + \Phi^+} \right)^n = 0.138 \quad (E-52)$$

The total power draw of the side channel pump is then:

$$P_{PumpSC,tot} = \frac{\Delta p_{SC} \frac{\dot{m}_{inC,tot,susp} \Psi^+}{\rho}}{\mathcal{E}_{Pump}} = 3.51 W \quad (E-53)$$

### E.6.3 Power draw of the purge pump

The flow rate for purging a single channel was in the range of 1.67 ml/min in the experiments, if the pause time was set to 10 seconds, which is more frequent as usually necessary. A pressure difference of 1.5 bar is assumed, which allows a purge of the side channel in a very short time. A total of 772 main channels is needed for the total inlet flow rate. At each main channel, 10 side channels are aligned, so a total of number of  $n_{SC,tot} = 7,700$  side channels have to be purged.

The power draw for the purge pump is thus:

$$P_{PumpPurge,tot} = \frac{\Delta p_{Purge} \dot{V}_{Purge} n_{SC,tot}}{\mathcal{E}_{Pump}} = 46 W \quad (E-54)$$

---

## **Appendix F      MATLAB Code**

The MATLAB Code is only available in the digital version.